Wegener Center for Climate and Global Change
University of Graz

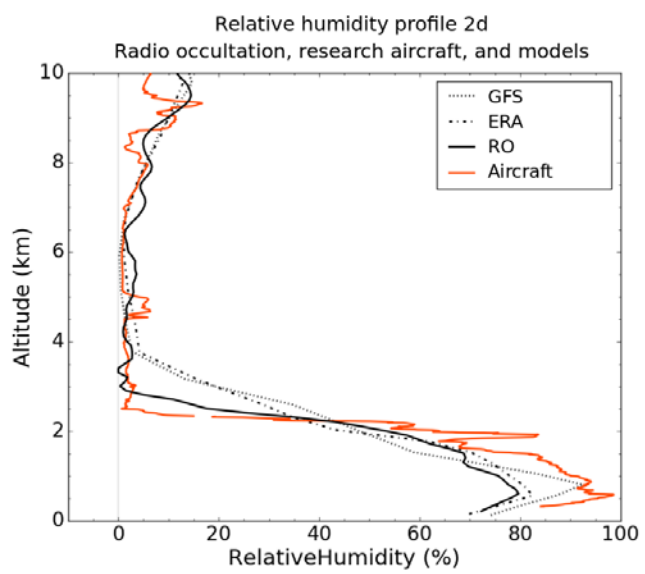

Scientific Report No. 78-2018

Investigating the value of GPS radio occultation water vapor data using in-situ and remote sensing techniques and models

Therese Rieckh

November 2018

Financially supported by

Wegener Center

UNI GRAZ

COSMIC

The **Wegener Center for Climate and Global Change** combines as an interdisciplinary, internationally oriented research institute the competences of the University of Graz in the research area “Climate, Environmental and Global Change”. It brings together, in a dedicated building close to the University central campus, research teams and scientists from fields such as geo- and climate physics, meteorology, economics, geography, and regional sciences. At the same time close links exist and are further developed with many cooperation partners, both nationally and internationally. The research interests extend from monitoring, analysis, modeling and prediction of climate and environmental change via climate impact research to the analysis of the human dimensions of these changes, i.e, the role of humans in causing and being effected by climate and environmental change as well as in adaptation and mitigation. (more informationen at www.wegcenter.at)

The present report is the result of a PhD thesis work completed in October 2018. The work was funded by Constellation Observing System for Meteorology, Ionosphere, and Climate/ University Corporation of Atmopsheric Research (COSMIC/UCAR) under research grant NSF-NASA AGS-1522830.

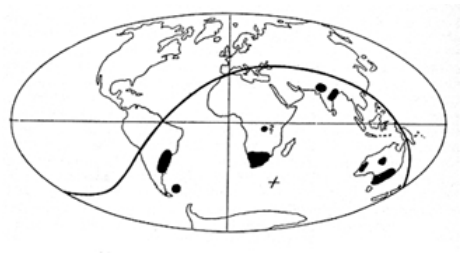

Alfred Wegener (1880-1930), after whom the Wegener Center is named, was founding holder of the University of Graz Geophysics Chair (1924-1930). In his work in the fields of geophysics, meteorology, and climatology he was a brilliant scientist and scholar, thinking and acting in an interdisciplinary way, far ahead of his time with this style. The way of his ground-breaking research on continental drift is a shining role model—his sketch on the relations of continents based on traces of an ice age about 300 million years ago (left) as basis for the Wegener Center Logo is thus a continuous encouragement to explore equally innovative ways:
paths emerge in that we walk them (Motto of the Wegener Center).

Wegener Center Verlag • Graz, Austria

ISBN 978-3-9504501-6-3

November 2018

Contact: Dr. Therese Rieckh
trieckh@gmail.com

Wegener Center for Climate and Global Change
University of Graz
Brandhofgasse 5
A-8010 Graz, Austria
www.wegcenter.at

RIECKH Therese

Investigating the value of GPS radio occultation water vapor data using in-situ and remote sensing techniques and models

PhD thesis
to obtain the academic degree
Doctor of Natural Sciences

submitted to the
Faculty of Environmental and Regional Sciences and Education
University of Graz

First referee: Assoz. Prof. FOELSCHE Ulrich

Institute for Geophysics, Astrophysics, and Meteorology/Institute of Physics, University of Graz; and Wegener Center for Climate and Global Change, University of Graz

Second referee: Dr. ANTHES Richard

President Emeritus, University Corporation for Atmospheric Research

Third referee: Univ. Prof. WICKERT Jens

Berlin Institute of Technology, GFZ-Potsdam

2018

This thesis, originally submitted in May 2018, was modified in November 2018. Papers II and III in Part II were updated to the final published versions of May and July 2018, respectively. Minor corrections were implemented throughout the thesis.

Supervisor

Assoz. Prof. Dr. Ulrich Foelsche
University of Graz, Austria

External supervisor

Dr. Richard Anthes, President Emeritus
University Corporation for Atmospheric Research, Boulder, Colorado, USA

Abstract

Water vapor is a major driver of climate and weather and plays a key role in many atmospheric processes. While water is present in all three aggregation states in the atmosphere, the gaseous one dominates and water vapor is the most important natural greenhouse gas. Due to its large latent heat of vaporization/condensation, water plays a major role in the energy transport of the atmosphere. To accurately model weather and climate it is crucial to understand the distribution, transport, and vertical structure of humidity. However, measuring water vapor accurately is a challenge, as it is highly variable on both spatial and temporal scales. To this day, no single observing system can provide global accurate tropospheric humidity data with a resolution that captures its variability on all important vertical, horizontal, and time scales.

The Global Positioning System (GPS) Radio Occultation (RO) method provides high vertical resolution humidity profiles for the troposphere. This measurement technique uses phase changes of GPS signals to derive atmospheric thermodynamic parameters. In the troposphere, ancillary data are required to retrieve humidity (or temperature).

The objective of this thesis is to assess the quality of RO-derived humidity using other remote sensing techniques, in-situ observing techniques, and model analyses and reanalyses. The structural uncertainty of RO-derived humidity is determined from comparisons of multiple different RO humidity retrievals. Even in challenging humidity conditions, such as high variability and extreme dryness, the accuracy of RO-derived humidity data is similar to the one of other state-of-the-art humidity measurements. Additionally, the RO technique features global coverage, all-weather capability, and same data quality for day and night time measurements. This shows the usefulness of RO for tropospheric humidity studies, as well as its potential to contribute tropospheric data to NWP models via data assimilation.

Zusammenfassung

Wasserdampf spielt eine wichtige Rolle in Wetter und Klima. Obwohl Wasser in allen drei Aggretatzuständen in der Atmosphäre vorhanden ist, dominiert der gasförmige Zustand und Wasserdampf ist das wichtigste natürliche Treibhausgas der Erde. Gleichzeitig spielt Wasser durch seine hohe latente Wärme eine große Rolle im atmosphärischen Energietransport. Wissen über die Verteilung und die Vertikalstruktur der troposphärischen Feuchte ist notwendig um Wetter und Klima korrekt modellieren zu können. Genaue Messungen stellen allerdings eine Herausforderung dar, da Wasserdampf sowohl zeitlich als auch räumlich extrem variabel ist. Keine einzige Messmethode kann Wasserdampf global mit einer Auflösung messen, welche dessen Variabilität auf einer zeitlichen, horizontalen und vertikalen Ebene widerspiegelt.

Die GPS Radiookkultationsmethode (RO) liefert die Möglichkeit, vertikal hoch aufgelöste Information über die Feuchteverteilung in der Troposphäre zu gewinnen. Bei dieser Messmethode werden über die Phasenwegsverlängerung von GPS Signalen thermodynamische Größen bestimmt. In der Troposphäre ist für die Berechnung von Feuchte allerdings zusätzliche Information notwendig.

Das Ziel dieser Arbeit ist es, die Qualität von RO Feuchtedaten mithilfe von anderen Fernerkundungsmethoden und in-situ Messungen sowie Modell-Analysen und Reanalysen abzuschätzen. Die strukturelle Unsicherheit der von RO abgeleiteten Feuchteinformation wird über Unterschiede zwischen verschiedenen Feuchte-Retrievals bestimmt. Sogar in Regionen mit starken Feuchteschwankungen ist die Genauigkeit von RO Feuchte vergleichbar mit der von anderen Messmethoden. Im Vergleich zu anderen Messmethoden und Modellen kann RO kurzzeitige und kleinräumige Variabilität auflösen. Zusätzlich liefert RO globale Messungen unter allen Wetterbedingungen bei Tag wie bei Nacht und zeigt daher durchaus Potential troposphärische Daten im Datenassimilationsprozess der Wettervorhersage beizutragen.

Acknowledgments

This thesis brings several years of work together. Over this time range, I have received support from many people in a variety of ways, and I can only acknowledge a subset of them individually. To all the helpful hands I received on the way, those I still remember and those that already slipped my mind, please know that you were greatly appreciated at the time. You probably made my day.

I sincerely thank my supervisor Ulrich Foelsche for setting me up on this path and supporting me on the way. I thank him for his knowledge and his guidance from my "base" and home University during my four years abroad. I also thank my mentor Andrea Steiner for her continuous support and knowing that I could always ask for help if I needed to.

I sincerely thank my external supervisor Richard Anthes, who, after more than 20 years of serving as UCAR's president, took on science again — and me as his supervisee. I thank Rick for advising me for over three years, for sharing his passion on science, for words of motivation when I needed them, and discussions on one eye-level where I was free to bring up any thought and idea without hesitation.

I have received a lot of support in Boulder during my stay: I thank Bill Kuo and Bill Schreiner for the opportunity to come to Boulder and work in the COSMIC group, as well as UCAR (with support of NSF and NASA) for the continuous financial support. I thank Ben Ho for close collaboration and Bill Randel for his contagious curiosity and passion for science. I thank the COSMIC team members for science discussions, IT support, tea times with home-made goodies, and board game lunches. I thank the NCAR grad student and postdoc fellows for more common lunches and tea times, writing accountability meetings, and shut-up-and-write sessions, without which I probably would have never finished this thesis. I also greatly appreciate the friends I have made in Boulder along the way, their time and patience when I sailed through a work-related low, their encouragement, and their ideas and actions to give my mind a break.

In my home town Graz and University base, I thank the entire Wegener Center team for the support during the past years, for the bits and pieces of code, the jokes, the friendly faces whenever I came to visit, and their help to navigate guidelines regarding this work. I particularly thank Lukas Brunner for sharing his LaTeX

template for this thesis. Many friends and fellow students in Graz already battled their way through the Magisterstudium with me, and even though we have spread to several different countries now, these friends have stayed close and we have been taking the ups and downs of a PhD together, too.

I thank all people involved with providing and supporting open-source tools, such as python, inkscape, and LaTeX, as well as the stackoverflow community.

I sincerely thank my family for their love and encouragement, as well as their patience and understanding that I chose to spend these past years in a faraway place.

Lastly, I thank my husband Jan. During the years, he was a constant source of encouragement and avid supporter of my path in science. At the same time, he made sure I kept track of my work-life balance and was always there to provide a different perspective, especially when I did not want one. Science often begins with asking the right questions, and Jan inspires me to constantly re-evaluate my values and approach to things, encouraging me to be both a better scientist and more fulfilled person.

Contents

Preface **1**

Part I. Synopsis

1. Introduction **5**

2. Humidity in weather and climate **9**
2.1. Important physical properties of water 9
2.2. Vertical humidity structure and circulation 11
2.3. Water vapor parameters 13

3. Tropospheric humidity measurement techniques **15**
3.1. Radiosonde measurements 15
3.2. Aircraft measurements 17
3.3. Thermal infrared nadir sounders: AIRS 18
3.4. Radio Occultation 19

4. Conclusions and summary **27**

Part II. Published papers

Paper I: Tropospheric dry layers in the Tropical Western Pacific: Comparisons of GPS radio occultation with multiple data sets **33**
1. Introduction 33
2. Data and methods 34
3. Individual profile comparisons 36
4. Case study: research flight 13 38
5. Results of all collocations 40
6. Global distribution 42
7. Conclusions 43
8. Data availability 43

9. Appendix A: RO water vapor retrievals 45
10. Appendix B: Contribution of RO in the 1D-Var 47

Paper II: Evaluating tropospheric humidity from GPS radio occultation, radiosonde, and AIRS from high-resolution time series 51

1. Introduction 51
2. Data and method 53
3. Results 56
4. Differences from ERA in dry versus wet atmospheric conditions 60
5. Variability during typhoon passages 62
6. Structural uncertainty of RO 64
7. Conclusions 65
8. Supplement 70

Paper III: Estimating observation and model error variances using multiple data sets 81

1. Introduction 81
2. Discussion of data sets 82
3. Derivation of error variances 84
4. Comparison with previous studies for RO refractivity 86
5. Calculation of the error variance terms using multiple data sets 86
6. Summary and discussion 92
7. Appendix A: Derivation of estimates of error variances using four data sets and the N-cornered hat method 94
8. Appendix B: Mean and standard deviations of three independent error estimates of q RH T and N using RO Direct and RO 1D-VAR at Guam Ishi Mina and Naze 98

Acronyms 105

List of figures 107

List of tables 111

Bibliography 113

Preface

This thesis is based on the following peer-reviewed publications:

Rieckh, T., Anthes, R., Randel, W., Ho, S.-P., and Foelsche, U. (2017). "Tropospheric dry layers in the tropical western Pacific: comparisons of GPS radio occultation with multiple data sets". *Atmos. Meas. Tech.* 10, pp. 1093–1110. DOI: 10.5194/amt-10-1093-2017.

Contributions: T. Rieckh and W. Randel formulated the initial idea of this work. R. Anthes and S.-P. Ho helped to develop the design of the study further. Together with U. Foelsche, they contributed ideas and provided valuable feedback. T. Rieckh collected the data, performed all the computational work and coding necessary, performed the analysis, and prepared both the text and figures of the entire manuscript. R. Anthes and W. Randel contributed significantly to the data analysis and the writing.

Rieckh, T., Anthes, R., Randel, W., Ho, S.-P., and Foelsche, U. (2018). "Evaluating tropospheric humidity from GPS radio occultation, radiosonde, and AIRS from high-resolution time series". *Atmos. Meas. Tech.* 11, pp. 3091–3109. DOI: 10.5194/amt-11-3091-2018.

Contributions: T. Rieckh and R. Anthes formulated the initial idea and developed the design of this work. W. Randel, U. Foelsche, S.-P. Ho contributed ideas and provided valuable feedback. T. Rieckh collected the data, performed all the computational work and coding necessary, performed the analysis, and prepared both the text and figures of the entire manuscript. R. Anthes contributed significantly to the data analysis and the writing.

Anthes, R. and **Rieckh, T.** (2018). "Estimating observation and model error variances using multiple data sets". *Atmos. Meas. Tech.* 11, pp. 4239–4260. DOI: 10.5194/amt-11-4239-2018.

Contributions: R. Anthes formulated the overall idea of this work. T. Rieckh performed all the computational work, created the figures, and contributed significantly to the discussion of the results and writing the paper.

In addition, I contributed to several other manuscripts, which are not part of this thesis, during the course of my PhD:

Biondi, R., Steiner, A., Kirchengast, G., and **Rieckh, T.** (2015). "Characterization of thermal structure and conditions for overshooting of tropical and extratropical cyclones with GPS radio occultation". *Atmos. Chem. Phys.* 15, pp. 5181–5193. DOI: 10.5194/acp-15-5181-2015.

Biondi, R., Steiner, A., Kirchengast, G., Brenot, H., and **Rieckh, T.** (2016). "A novel technique including GPS radio occultation for detecting and monitoring volcanic clouds". *Atmos. Chem. Phys. Discuss.* DOI: 10.5194/acp-2015-974.

Biondi, R., Steiner, A., Kirchengast, G., Brenot, H., and **Rieckh, T.** (2017). "Supporting the detection and monitoring of volcanic clouds: A promising new application of Global Navigation Satellite System radio occultation". *Adv. Space Res.* 60, 12, pp. 2707–2722. DOI: 10.1016/j.asr.2017.06.039.

Gilpin, S., **Rieckh, T.**, and Anthes, R. (2018). "Reducing representativeness and sampling errors in radio occultation–radiosonde comparisons". *Atmos. Meas. Tech.* 11, pp. 2567–2582. DOI: 10.5194/amt-11-2567-2018.

Rieckh, T. and Anthes, R. (2018). "Evaluating two methods of estimating error variances using simulated data sets with known errors". *Atmos. Meas. Tech.* 11, pp. 4309–4325. DOI: 10.5194/amt-11-4309-2018.

This thesis starts with a synopsis in Part I which includes an introduction and motivation of the research question and overall scope of this thesis. Scientific background, data, and methods are discussed. The conclusion summarizes and combines the results of the publications, which are presented in Part II. The complete list of acronyms, figures, tables, and the bibliography are in the end of this thesis.

Part I.

Synopsis

1. Introduction

> *Despite its central importance, work to date has not led to a universally accepted picture of the factors controlling water vapor amount, a solid understanding of the mechanisms by which it influences atmospheric processes, or even precise knowledge of its concentrations in many parts of the atmosphere, to say nothing of its trends over time.*
>
> Sherwood et al. [2010]

Accurate and precise measurements of tropospheric water vapor are of high importance for a variety of reasons. Firstly, water vapor is the most important greenhouse gas in the troposphere [IPCC, 2007] and therefore a very important driver of Earth's climate. Climate models need high-quality measurements as a baseline for comparisons with climate model output, to put current climate into context, and to accurately model climate change. Secondly, humidity is an important driver for many atmospheric processes, which together determine the current state of the weather [Sherwood et al., 2010, Stevens and Bony, 2013]. Numerical Weather Prediction (NWP) models depend upon high-quality measurements and will provide both a better weather forecast as well as improved forecasts of extreme events, such as cyclone intensity and path or extreme precipitation events. Thirdly, since water vapor is involved in so many atmospheric processes, scientific interest alone is a motivation study the distribution, variability, and transport of water vapor throughout Earth's atmosphere. High quality measurements of atmospheric humidity products are therefore key for scientific progress related to weather and climate, as well as model development and evaluation; however, the strong spatial and temporal variability of water vapor as well as its change over five orders of magnitude from surface to mesopause pose challenges on observing systems. Measurement techniques therefore focus on specific altitudes to narrow the concentration range. Within the troposphere, this range still covers three orders of magnitude, and to this date, no single current observing technique can provide unbiased and precise tropospheric humidity measurements of high vertical resolution and global coverage.

The Global Positioning System (GPS) Radio Occultation (RO) technique fulfills most of the above-mentioned criteria, featuring International System of Units (SI)

traceability, global coverage, high vertical resolution, and all-weather capability, and high accuracy and precision for the parameters refractivity and temperature [Melbourne et al., 1994, Hajj et al., 2002, Anthes, 2011]. In fact, RO has shown the potential to provide data of climate benchmark quality for refractivity and temperature between about 8 km and 25 km [Ho et al., 2009, 2012, Steiner et al., 2013]. However, the quality of RO humidity is still an important subject of research. Firstly, the uncertainty of RO products is relatively high in the lower and mid troposphere, increasing the uncertainty of the retrieved humidity. Secondly, in order to derive humidity from RO refractivity, ancillary (*a-priori*) data are required, which are usually used from a model analysis or reanalysis. Two different methods, a direct retrieval or a One-Dimensional Variational (1D-Var) retrieval can be used to derive humidity. Both the choice of retrieval as well as the a-priori estimate have an influence on the resulting humidity profile.

This thesis provides new results on the quality of troposheric humidity data retrieved from GPS RO measurements. I used data from multiple models and measurement techniques, in-situ as well as remotely sensed, to assess the ability of RO to provide accurate humidity profiles in the troposphere, and to evaluate its usefulness at different altitudes. This work discusses strengths and weaknesses of using RO for deriving humidity products, compared to other state-of-the-art measurement techniques.

The general setup for the study includes:

1. Use of multiple different RO humidity retrievals. At minimum, a direct retrieval and a 1D-Var retrieval; but also comparisons of humidity retrievals from different RO processing centers to determine the structural uncertainty of RO-derived humidity.

2. Comparison of individual profiles rather than comparing data averaged over large regions and time spans. This allows investigation of details of the profile structure, variability on relatively small vertical scales, and bias detection related to profile structure.

3. Comparisons in regions with complicated humidity conditions, including regions with tropical cyclone activity, dry air intrusions, and atmospheric conditions that favor super-refraction.

The synopsis is structured as follows: Chapter 2 gives a short overview of the role of water and water vapor in weather and climate and introduces atmospheric parameters that are commonly used to describe humidity. Various measurement techniques are discussed in Chapter 3, with focus on the RO technique. Chapter 4

introduces the combined setup of all studies and summarizes the results of the publications.

2. Humidity in weather and climate

Water vapor plays key role in both driving weather and influencing climate, resulting from the combination of its abundance in the troposphere and its physical properties. Water is the most abundant liquid on Earth, and water vapor can make up to 4 % of tropospheric composition. Water has a high latent heat of vaporization/condensation, via which it can capture, transport, and release enormous amounts of energy and drive major atmospheric events. The triple point of water lies well within standard atmospheric conditions, allowing frequent phase changes. Water influences Earth's radiation balance in gaseous, liquid, and solid form. Water vapor is sensitive to a continuous spectrum of thermal infrared radiation, making it Earth's most important greenhouse gas and accounting for 60 % of the natural greenhouse effect [Kiehl and Trenberth, 1997]. Clouds influences Earth's albedo and therefore incoming radiation. Lastly, water vapor influences air quality and visibility via chemical processes.

Water vapor is extremely variable on temporal, horizontal, and vertical scales. Water vapor concentration varies over three orders of magnitude in the troposphere, and over five orders from surface to the mesopause [Kämpfer, 2013]. Over 50 % of Earth's atmospheric water vapor is located within the lowest 2 km of the tropopshere [Mockler, 1995]. In the Upper Troposphere – Lower Stratosphere (UTLS) region water vapor concentrations are very small, but water vapor still plays a major role in chemical and radiative processes.

2.1. Important physical properties of water

Bent molecular structure The oxygen atom has six valence electrons and shares another two with the hydrogen atoms via covalent bonding. Therefore two electron pairs are not bonded with another atom ("lone pairs"), which leads to the tetrahedral shape of the molecule. Since lone pairs occupy more space than bonding pairs, the bond angle is 104.5°, smaller than the one of a perfect tetrahedral molecule.

Electronegativity difference Oxygen has a much higher electronegativity than hydrogen (3.44 versus 2.2 on the Pauling scale), meaning that the bonding

electrons are more attracted to the oxygen atom [Housecroft and Sharpe, 2008]. Together with the bent shape, this causes the molecule to be partially positively and partially negatively charged, i.e. a permanent dipole moment.

Permanent dipole moment The permanent dipole moment allows intermolecular forces in water called hydrogen bonding. Hydrogen bonding is responsible for a number of important properties of water, e.g. its increased volume in the solid state compared to liquid state, large heat capacity in the liquid state, and high cohesiveness and resulting high surface tension.

Large heat capacity The large heat capacity of liquid water, resulting from its permanent dipole moment, moderates Earth's climate as it requires a large amount of energy (or energy release) to raise (or lower) its temperature.

Large latent heat The large latent heat of vaporization/condensation of water allows to capture and release large amounts of energy via phase changes, which also facilitates energy transport.

The triple point The triple point of water, where all three phases can coexist, is at a temperature of 273.16 K and a partial pressure of water vapor of 6.112 hPa [Sherwood et al., 2010]. This point lies within typical atmospheric conditions, thus water can be found in all three states (solid, liquid, gaseous) in the atmosphere. However, the gaseous state dominates [>99 %, Stevens and Bony, 2013].

Greenhouse gas The complex water molecule can experience the following modes as a response to incoming radiation of the right wavelength: three modes of translation of the center of mass, three modes of rotation around the center of mass, three modes of vibration of the molecule; as well as combinations of these modes. For water vapor, this leads to a continuous spectrum of absorption lines in the near-infrared and thermal infrared (see Fig. 2.1). This makes water vapor the most important absorber of solar radiation in the lower atmosphere [Stevens and Bony, 2013]. Any kind of condensed water (i.e. hydrometeors) cools the atmosphere by scattering shorter wavelengths of incoming radiation and warm the atmosphere via absorption of the longer ones. Therefore clouds affect Earth's radiative balance both via their large albedo and via their strong greenhouse effect, where the former cooling rate is roughly twice as large as the latter heating rate at the top of the atmosphere [Stevens and Bony, 2013].

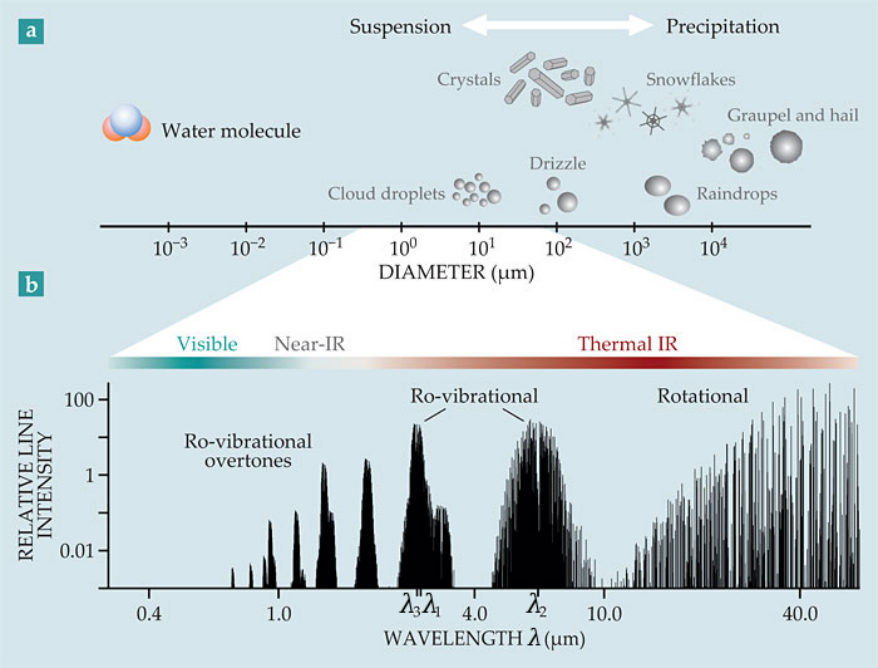

Figure 2.1.: (a) Hydrometeors: the condensed forms of water in the atmosphere come in several sizes and shapes. (b) The near- and thermal infrared regions of the spectrum excite the water molecule and produce its rotational–vibrational (or ro-vibrational) and rotational bands. Specific lines λ_1, λ_2, and λ_3 mark the symmetric stretching mode, bending mode, and asymmetric stretching mode, respectively. Figure and caption (adapted) taken from Stevens and Bony [2013].

2.2. Vertical humidity structure and circulation

Idealized simulations show that the influence of water on the atmosphere's structure and circulation patterns is comparable to or larger than the influence from Earth's rotation, presence of continents, and poleward gradients of solar insolation [Stevens and Bony, 2013]. The latent heat of water vapor accounts for about half of the poleward and most of the upward heat transport within Earth's atmosphere. Furthermore, water vapor dominates net radiative cooling of the troposphere, which drives convection [Sherwood et al., 2010].

The vertical structure of water vapor pressure e is restricted by the saturation vapor pressure e_s, which in turn depends on temperature T. The relationship is described by Clapeyron's equation, which relates pressure of a substance to temperature in a system with both phases in equilibrium. For meteorology, this equation is expressed as:

$$\frac{1}{e_\mathrm{s}}\frac{\mathrm{d}e_\mathrm{s}}{\mathrm{d}T} = \frac{L_\mathrm{v}}{R_\mathrm{v}T^2} \tag{2.1}$$

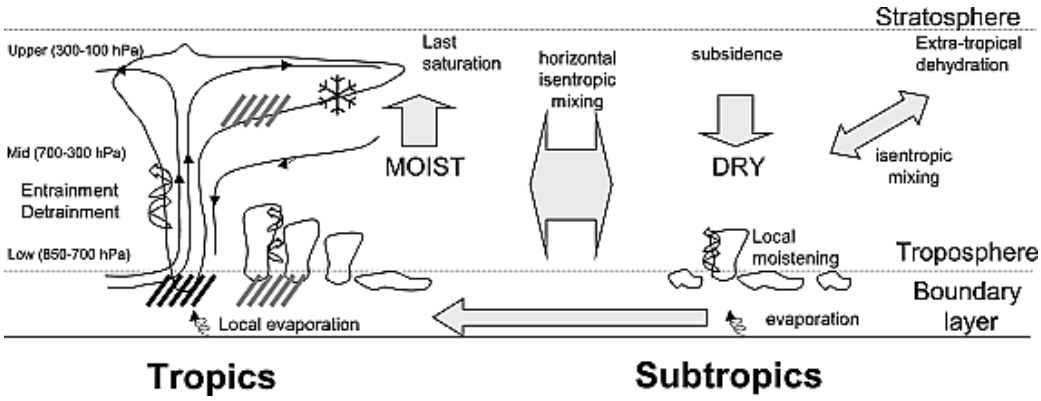

Figure 2.2.: Schematic of the overturning circulation in the tropics and subtropics. Figure taken from Sherwood et al. [2010].

where L_v is the latent heat of vaporization ($2.501 \times 10^6\,\mathrm{J\,kg^{-1}}$ at 0 °C) (or latent heat of sublimation ($2.834 \times 10^6\,\mathrm{J\,kg^{-1}}$) for e_s with respect to ice) and R_v is the gas constant for water vapor ($461.5\,\mathrm{J\,kg^{-1}\,K^{-1}}$). Equation 2.1 can be integrated (assuming L_v constant) and e_s is given as:

$$e_\mathrm{s} = e_{\mathrm{s}0} \exp\left(\frac{L_\mathrm{v}}{R_\mathrm{v}}\left(\frac{1}{T_0} - \frac{1}{T}\right)\right) \tag{2.2}$$

with T_0=273.15 K and e_{s0}=6.11 hPa.

The saturation vapor pressure e_s roughly doubles for every 10 K of temperature increase. Because 1) T decreases with altitude, 2) e_s decreases with decreasing T, and 3) the upper limit for e is e_s (supersaturation with respect to water is rare in the troposphere because condensation nuclei are plentiful [Sherwood et al., 2010]), temperature constrains the vertical structure of e. If e exceeds e_s, water vapor will condense into liquid or ice clouds, which will eventually either precipitate or re-evaporate in warmer temperatures.

The global hydrological cycle traces the largest movement of any substance on Earth [Foelsche, 1999]. Figure 2.2 shows a simple schematic of the overturning circulation for the tropics and subtropics, where most of the water vapor feedback takes place. Water enters the troposphere via surface evaporation, with its maximum over trade wind regions in the subtropical oceans [Sherwood et al., 2010]. Overall, the water vapor in the Planetary Boundary Layer (PBL) gets transported towards the Intertropical Convergence Zone (ITCZ), where it gets lifted within convective clouds, and transported to the upper-air subtropical regions. In regions of subsidence, air is compressed, warmed, and mixed with surrounding air [Sherwood et al., 2010].

2.3. Water vapor parameters

Atmospheric humidity can be described by a variety of parameters. Most commonly used are the following definitions.

2.3.1. Mixing ratio *r* or *w*

The mixing ratio describes the amount of water in the air and is given as the ratio of the mass of water m_{w} to the mass of dry air m_{dry}. In the troposphere it is usually given in either $\mathrm{g\,kg^{-1}}$ or $\mathrm{kg\,kg^{-1}}$.

$$r = w = \frac{m_{\mathrm{w}}}{m_{\mathrm{dry}}} \tag{2.3}$$

It is related to pressure and water vapor pressure via:

$$r = w = \frac{0.622 \cdot e}{p - e} \tag{2.4}$$

The mixing ratio r can be approximated by specific humidity q.

2.3.2. Specific humidity *q*

Specific humidity q (in the troposphere also usually given in $\mathrm{g\,kg^{-1}}$) is the ratio of the mass of water m_{w} to the total air mass m and can also be expressed via the mixing ratio r.

$$q = \frac{m_{\mathrm{w}}}{m} = \frac{m_w}{m_{dry} + m_{\mathrm{w}}} = \frac{r}{r+1} \tag{2.5}$$

Specific humidity q is related to p and e via:

$$q = \frac{0.622 \cdot e}{p - 0.378 \cdot e} \tag{2.6}$$

2.3.3. Water vapor pressure *e*

Water vapor pressure e (usually given in hPa) denotes the partial pressure of water in the atmosphere. It is commonly used when handling Radio Occultation (RO) data because of its connection to refractivity N, temperature T, and pressure p in the Smith–Weintraub equation (see Chapter 3). Water vapor pressure e can be derived from the above equations as:

$$e = \frac{q \cdot p}{0.622 + 0.378 \cdot q} \tag{2.7}$$

2.3.4. Relative humidity RH

Relative Humidity (RH) is defined as the fraction of water vapor pressure e to saturation water vapor pressure e_s:

$$\mathrm{RH} = 100 \cdot \frac{e}{e_\mathrm{s}} \tag{2.8}$$

where RH is given in percent. At higher altitudes below freezing, RH can be defined using saturation pressure either with respect to water or with respect to ice. The definition with respect to water is more commonly used because air can easily become supersaturated with respect to ice. Most hygrometers are sensitive to relative humidity with respect to water also at temperatures below freezing.

2.3.5. Dew point temperature T_d

Dewpoint temperature is the temperature to which an air parcel needs to be cooled to (while keeping pressure constant) to saturate the parcel (RH = 100 %):

$$e = e_\mathrm{s}(T_\mathrm{d}) \tag{2.9}$$

Using Eq. (2.2) and $T = T_\mathrm{d}$, the dew point temperature can be computed for a given water vapor pressure:

$$\frac{1}{T_\mathrm{d}} = \frac{1}{T_0} - \left(\frac{R_\mathrm{v}}{L_\mathrm{v}}\right) \ln\left(\frac{e}{e_{s0}}\right) \tag{2.10}$$

3. Tropospheric humidity measurement techniques

Generally, tropospheric humidity can be measured by both in-situ and remote sensing techniques. In-situ techniques measure humidity directly and are usually used on aircraft, radiosondes, and dropsondes. In-situ data are point measurements, hence they can provide high vertical resolution profiles of localized humidity features. A disadvantage of in-situ techniques is that they tend to cover small spatial regions and are generally not available at locations which are difficult or expensive to reach (such as polar regions or over oceans). Remote sensing techniques do not measure humidity directly, but rather derive it from another, measurable quantity. Active sensors transmit radiation and measure the signal scattered back to the receiver. Passive sensors derive information on humidity via the radiation emitted or scattered by the atmosphere. Sensor platforms include satellites, airplanes, and the ground. An advantage of remote sensing is the large area covered — it is possible to observe the entire globe with only a few satellites. In contrast to in-situ techniques, data can easily be gathered in remote places. However, these advantages are offset to some degree by much coarser horizontal and vertical resolution, from sub-kilometer to several kilometer (vertical) to several hundreds of kilometers (horizontal).

Discussing all current observation techniques is well outside the scope of this introduction. Details on tropospheric water vapor observation techniques can be found in Kämpfer [2013] and references therein. The following sections give a short introduction on the subset of tropospheric humidity measurement techniques which are used in the papers in Part II, and a more detailed description of the Radio Occultation (RO) technique, as these data are the core of this work.

3.1. Radiosonde measurements

Radiosondes are a relatively simple method to collect tropospheric and stratospheric data. The first device that closely resembled the modern radiosonde – a meteograph with a radio transmitter – was launched as early as in 1929[1]. Temperature, humidity,

[1] http://radiosondemuseum.org

and pressure data were transmitted to a ground station, and the first prototype of the modern radiosonde was born. The principle is still the same today: a gas-filled balloon carries the instrument upwards, usually with an ascending rate of about $4\,\mathrm{m\,s^{-1}}$ to $6\,\mathrm{m\,s^{-1}}$. Data are transmitted to a ground station during the ascent and reported on so-called "mandatory pressure levels". Mandatory pressure levels are the 1000, 925, 850, 700, 500, 400, 300, 250, 200, 150, 100, 70, 50, 30, 20, and 10 hPa levels[2]; however, radiosondes can also have a cut-off altitude at which they stop reporting. Additionally, data are reported on so-called "significant thermodynamic levels" if strong humidity or temperature changes occur at that level. Since radiosondes provide point measurements, the resulting profile can show strong variability in the vertical, especially if clouds and strongly changing humidity conditions are present. When the radiosonde reaches an altitude where the surrounding air pressure gets too low, the balloon bursts and the radiosonde is lowered to the ground via a small parachute. Recovery of the sonde is not necessary since data are transmitted throughout the ascent.

Although the principle is still the same, radiosonde layout, sensors, and handling have undergone significant improvement (Fig. 3.1). Radiosondes have become smaller and cheaper, and sensors have become more accurate[3]. Since 1957, all global radiosonde stations launch their sondes at 00 and 12 UTC [Lazante et al., 2002]. Specialized sondes have been developed, such as dropsondes and ozonesondes. Dropsondes are dropped out of planes and collect data while descending on a parachute, and are frequently used to collect data withing tropical and subtropical cyclones. Ozonsondes are launched with a much lower frequency and measure tropospheric and lower stratospheric ozone concentration.

Radiosonde measurements provide the longest record of tropospheric humidity data, however, the long record comes with discontinuities in the data [Dai et al., 2011]. Instrument development has overall greatly improved sensor accuracy, but different sensor types still each have their unique bias, known or unknown [Miloshevich et al., 2006, Vömel et al., 2007, Ho et al., 2010]. Many different sensor types are used globally, and sensor types are often switched over time. If not properly documented (which has been rather the rule than the exception), a switch in sensor type can lead to an artificial trend or jump in the station's record. While those data are still useful in operational weather forecasting, climate change monitoring and detection studies cannot be performed without detailed knowledge about a station's record regarding sensor development and changes. The Integrated Global Radiosonde Archive (IGRA) collects and provides global radiosonde data and information about each station's history and changes, such as sensor type and

[2] http://glossary.ametsoc.org/wiki/Mandatory_level
[3] http://radiosondemuseum.org

Figure 3.1.: A radiosonde from 1929 (left) compared to a modern-day radiosonde. Figures from http://radiosondemuseum.org.

updates, location changes, and measured atmospheric parameters. Conclusions about the data can be drawn to some extent from the historical information.

Another recent effort to address discontinuities in radiosonde records is made by the Global Climate Observing System (GCOS) Reference Upper-Air Network (GRUAN). The aim is to provide high-quality long-term vertical profiles of selected essential climate variables, including an estimate of the measurement uncertainty, while monitoring all changes a station has undergone [Bodeker et al., 2016]. The number GRUAN radiosonde stations keeps expanding and currently has 9 certified stations and 17 more to be certified (status: February 2018). The individual station's record is still relatively short (less than 4 years for certified stations), but these data are valuable for calibration and evaluation of global measurement networks.

3.2. Aircraft measurements

Research aircraft are the most flexible measurement techniques since they have the capacity to measure many different tropospheric parameters at once (given the availability of the according instruments). Applications for aircraft data include

studies of tropospheric chemistry, chemical cycles, clouds and aerosols, radiative transfer in clear air and clouds, Upper Troposphere – Lower Stratosphere (UTLS) processes, turbulence and boundary layer processes, mesoscale weather systems, and more [see e.g. Jensen et al., 2013, Pan et al., 2017].

As such, research aircraft can provide high-quality, high-resolution humidity profiles in the troposphere, but are also highly constrained in both time and space. Both manned and unmanned research aircraft missions are expensive and thus infrequent, restricted to altitudes from the surface to lower edge of the stratosphere, and often confined to a geographic region, studying a particular event or area of interest. Globally applicable conclusions can hardly be drawn from solely research aircraft measurements, but aircraft measurements are important verification tools of weather models and ground-based and satellite-based measurements [e.g. Randel et al., 2016, Rieckh et al., 2017].

3.3. Thermal infrared nadir sounders: AIRS

Data from both active and passive (microwave and infrared) nadir-sounders are available globally and in large amounts, which makes them valuable for data assimilation. Roughly 80 % of all assimilated data in ECMWF Reanalysis Interim (ERA-Interim) are radiances [Poli et al., 2010]. However, as an inherent feature of a nadir sounder, vertical resolution of the profiles is low. An overview of various active and passive infrared and microwave sounders can be found at https://earthdata.nasa.gov/user-resources/remote-sensors.

Atmospheric Infrared Sounder (AIRS) is a thermal infrared grating array spectrometer that measures radiances of Earth's surface and atmosphere and provides humidity profiles as Level 2 products. AIRS measures the infrared brightness on 2378 spectral channels in the 3.7 µm to 15.4 µm range[4]. Each wavelength is sensitive to temperature and water vapor over a certain altitude range in the atmosphere. Thus profiles of atmospheric parameters (temperature, humidity) can be derived by using multiple infrared detectors, each of which are sensing a particular wavelength. However, the vertical resolution of these profiles is around 2 km to 3 km, which is finer than other infrared or microwave nadir sounders, but also large compared to the variability of water vapor in the vertical. Thus nadir sounders fail to detect the majority of smaller scale vertical variability of tropospheric humidity. Since AIRS is an infrared based system, it cannot provide data within or below clouds.

[4] https://airs.jpl.nasa.gov/

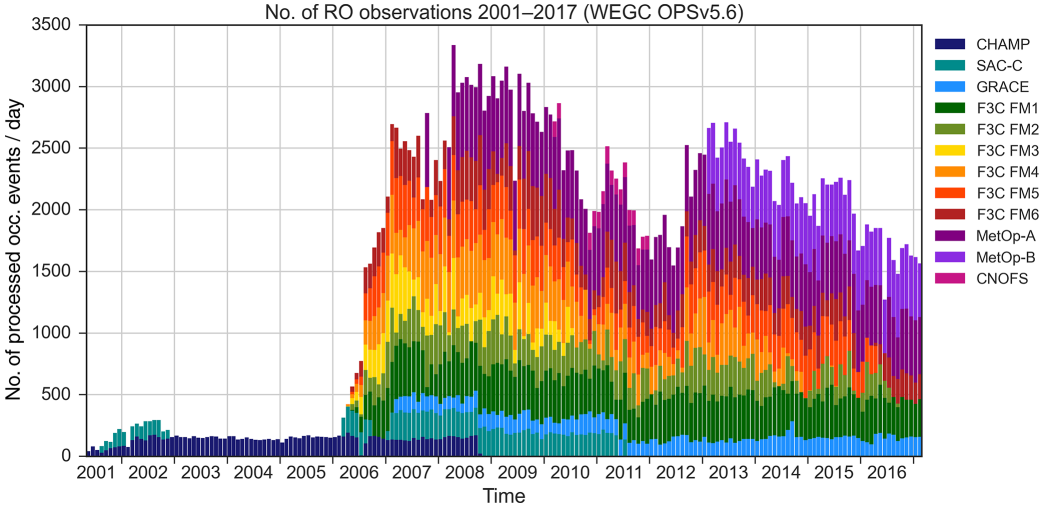

Figure 3.2.: Number of daily processed RO profiles at the WEGC over time. The number of available RO profiles increased strongly in 2006 when the six COSMIC satellites were launched. Even though many COSMIC satellites still performed years after their expected life time, the number of profiles has decreased over time, and MetOp-A and MetOp-B have provided the majority of profiles in recent years. Figure taken from Angerer et al. [2017].

3.4. Radio Occultation

Global Positioning System (GPS) RO is a limb sounding technique that makes use of the signals emitted by GPS satellites to derive atmospheric parameters. The GPS L1 and L2 signals are delayed and refracted when traveling through Earth's atmosphere and received on-board a Low-Earth Orbit (LEO) satellite. The altered signals are processed to bending angles α, from which atmospheric parameters such as refractivity N, pressure p, temperature T, and water vapor pressure e can be derived.

Features of the RO technique are global coverage, all-weather capability, SI-traceability, and high accuracy and precision of near-vertical profiles with high vertical resolution [Melbourne et al., 1994, Hajj et al., 2002, Anthes, 2011]. After the successful proof-of-concept mission GPS/MET in 1995 [Ware et al., 1996], a number of RO research missions have provided over six million RO profiles globally since mid 2001 (Fig. 3.2) .

The RO technique makes use of the readily available GPS satellite constellation and their transmitted signals. GPS L-band frequencies were chosen for a number of reasons, including a minimum effect of weather on the GPS signal propagation. However, the residual influence of the atmosphere on the L1 and L2 signals yields accurate and precise profiles of atmospheric parameters with high vertical

resolution on a global scale. The 24 GPS satellites that orbit the Earth at about 55° inclination continuously transmit signals at the L1 and L2 frequencies (L1: λ=19.0 cm, f=1575.2 MHz); L2: (λ=24.4 cm, f=1227.6 MHz).

When the GPS signals travel through Earth's atmosphere, they are delayed and refracted in the ionosphere and neutral atmosphere because the refractive index n is not unity. Furthermore, the signals are bent due to the gradients of n (air density changes with altitude). The altered signals are received at a LEO satellite as a phase change, function of time. Due to the motions of the satellites, the atmosphere is scanned from top to bottom (setting occultation) or from bottom to top (rising occultation), which yields profiles of phase changes between the intrinsically transmitted and the received delayed signals. Measurement duration for one such profile is about 3 min.

The profiles of phase changes are combined with precise orbit information, geometric delay, and clock correction to retrieve bending angles α, as a function of the impact parameter a. The bending angle is given by the integral of incremental bending along the ray path [see e.g. Foelsche, 1999]. Since bending angles are frequency-dependent, ionospheric influence on the measurement can be removed by linearly combining the L1 and L2 bending angles. The result is one bending angle profile that describes the neutral atmosphere.

The impact parameter is the perpendicular distance between the center of refraction (which is roughly at Earth's center) and any of the ray asymptotes. It is given as:

$$a = nr\sin(\varphi) \tag{3.1}$$

where n is the refractive index, r is the radius of the ray path, and φ is the angle between r and the tangent of the ray. Due to the dependence of a on n, the impact parameter is always occultation-specific, but constant along the ray path. A schematic of an occultation is shown in Fig. 3.3.

Bending angle profiles can be converted to profiles of refractive index n (and refractivity N) by applying the inversion of the so-called Abel integral, which is given as:

$$n(r_\mathrm{t}) = \exp\left[-\frac{1}{\pi}\int_{a_\mathrm{t}}^{\infty}\frac{\alpha(a)}{\sqrt{a^2-a_\mathrm{t}^2}}\mathrm{d}a\right] \tag{3.2}$$

with the impact parameter a (and impact parameter at the tangent point a_t), the radius of the tangent point r_t, and the refractive index n [Kursinski et al., 1997]. The upper boundary of the integral is infinity and requires initialization. Initialization varies among the RO processing centers [see e.g. Ho et al., 2012].

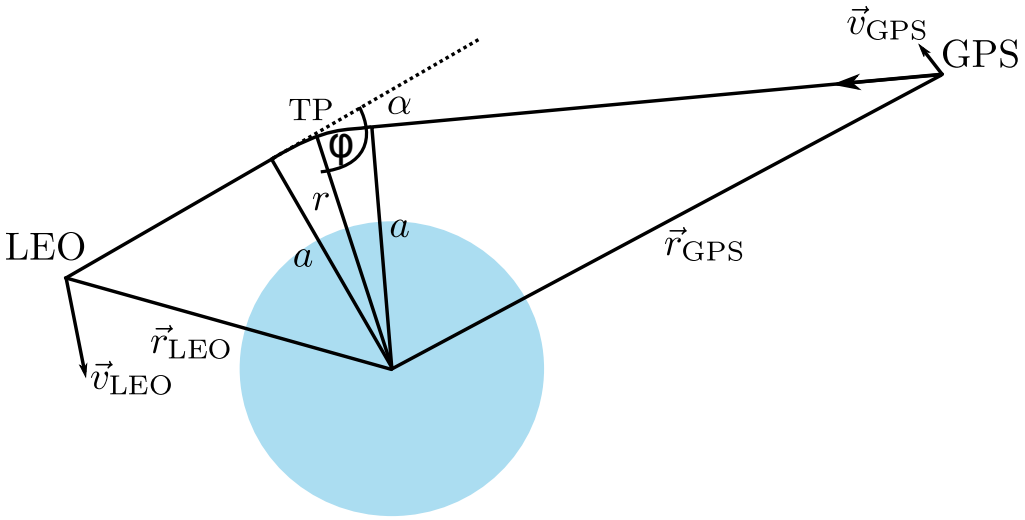

Figure 3.3.: Schematic of the occultation geometry for a setting event (LEO satellite setting with respect to GPS satellite). The GPS signal is refracted by the ionosphere and neutral atmosphere and received at a LEO satellite. TP is the tangent point, r the radius of the ray path, a is the impact parameter, φ is the angle between r and the ray tangent, α is the bending angle, and $\vec{r}_{\mathrm{GPS}}$ and $\vec{r}_{\mathrm{LEO}}$ are the position vectors of the GPS and LEO satellite, respectively. Figure taken and adapted from Pirscher [2010].

Since vertical changes in the refractive index n are small, refractivity N is computed from n as:

$$N = (n - 1) \cdot 10^6 \tag{3.3}$$

N is related to several atmospheric parameters via the Smith–Weintraub equation [Smith and Weintraub, 1953]:

$$N = 77.6\frac{p}{T} + 3.73 \cdot 10^5 \frac{e}{T^2} - 4.03 \cdot 10^7 \frac{n_{\mathrm{e}}}{f^2} + 1.4W \tag{3.4}$$

with atmospheric pressure p (hPa), temperature T (K), partial pressure of water vapor e (hPa), electron density n_{e} (electrons m^{-3}), transmitter frequency f (Hz), and mass of condensed water in the atmosphere W ($\mathrm{g\,m}^{-3}$). The first and second term on the Right Hand Side (RHS) describe the contributions of the dry and wet atmosphere, respectively. The third term describes ionospheric influence and can be neglected since ionospheric influence is handled earlier in the retrieval. The last term describes influence due to scattering on liquid water and can also be neglected.

If humidity is negligible, computation of T and p is straightforward. Only the first term on the RHS remains, and combining it with the ideal gas law, density can be derived:

$$N_{\mathrm{dry}} = 77.6\frac{p_{\mathrm{dry}}}{T_{\mathrm{dry}}} = 77.6\rho_{\mathrm{dry}}\frac{R}{M_{\mathrm{dry}}} \tag{3.5}$$

where ρ_{dry} is density, R is the universal gas constant ($8.314\,\mathrm{J\,K^{-1}\,mol^{-1}}$) [Mohr et al., 2008] and M_{dry} is the mean molecular mass of dry air ($28.964\,\mathrm{kg\,kmol^{-1}}$) [Khélifa et al., 2007]. Using the hydrostatic equation and the ideal gas law, pressure and temperature can be computed:

$$p_{\mathrm{dry}}(h) = \int_{h}^{\infty} g(\Phi, h')\rho_{\mathrm{dry}}(h')\mathrm{d}h' \tag{3.6}$$

$$T_{\mathrm{dry}}(h) = \frac{M_{\mathrm{dry}}p_{\mathrm{dry}}(h)}{R\rho_{\mathrm{dry}}(h)} \tag{3.7}$$

where $g(\Phi, h')$ is the latitude and altitude dependent gravitational acceleration. This retrieval can be used to retrieve T and p in the stratosphere and above.

At altitudes where humidity is significant (i.e. in the troposphere), neglecting the second term in the Smith–Weintraub equation will lead to large errors in T and p and also does not provide any humidity information. This became more relevant with the development of open-loop tracking [Sokolovskiy et al., 2006], which enabled signal tracking at lower altitudes and thus lower penetration depths for RO profiles. About one third of the profiles reach below the lowest kilometer, and two thirds below the lowest two kilometers Mean Sea Level (MSL), enabling the use of RO data to study features of the lower troposphere, such as Planetary Boundary Layer (PBL) height [Ao et al., 2012, Xie et al., 2012, Ho et al., 2015].

To retrieve correct tropospheric parameters, the first and second terms in Eq. (3.4) remain and N is given as:

$$N = 77.6\frac{p}{T} + 3.73 \cdot 10^5\frac{e}{T^2} \tag{3.8}$$

Auxiliary information is required to retrieve temperature and humidity. There are two common approaches to derive physical T, p, and e: applying a direct retrieval, or a One-Dimensional Variational (1D-Var) retrieval. Several RO processing centers currently provide water vapor profile retrievals: University Corporation for Atmospheric Research (UCAR), Jet Propulsion Laboratory (JPL), Danish Institute for Meteorology (DMI), and WEGC. These centers vary in their choice of humidity retrieval and details (i.e. choice of a-priori, magnitude of prescribed errors, etc).

3.4.1. The direct retrieval

The direct retrieval combines T from an external source (e.g. model forecast, re-analysis, or different measurement technique) with RO N to directly compute water vapor pressure e. The direct retrieval is commonly used because of its simplicity and independence from first guess humidity. Errors in RO humidity derived via the direct retrieval include errors of the RO refractivity and of the input temperature.

The error in e due to errors in T can be directly computed by taking the first derivative of Eq. (3.4):

$$\delta e = \frac{1}{k_2} \left(2NT - k_1 p\right) \delta T \tag{3.9}$$

where k_1 and k_2 are $77.6\,\mathrm{K\,hPa^{-1}}$ and $3.73\,10^5\,\mathrm{K^2\,hPa^{-1}}$, respectively (see Eq. (3.8)). Figure 3.4 shows the approximate specific humidity q errors due to T errors for several pressure levels and different latitudes. The impact of T uncertainty is smaller when humidity is higher, such as at low altitudes (Fig. 3.4, blue, purple, and red lines) and in the tropics (Fig. 3.4, panel A).

A second source of errors of RO derived humidity stems from refractivity uncertainty, which mainly comes from atmospheric multipath, receiver tacking errors, and Super Refraction (SR). Atmospheric multipath occurs in the lower troposphere where strong humidity variability in the vertical leads to sharp vertical refractivity gradients, which results in interference in the phase measurements. Radio-holographic methods reduce or eliminate this effect [Gorbunov, 2002]. Signal tracking errors can occur under complicated signal dynamics, typically in the moist troposphere [Beyerle et al., 2002] and can be minimized by the use of open loop tracking [Sokolovskiy, 2001]. SR occurs when bending of the ray becomes locally so large that its curvature is smaller than the curvature of the Earth ($\mathrm{d}N/\mathrm{d}z < -157\,\mathrm{N\text{-}units\,km^{-1}}$) and is often caused by sharp humidity gradients in the vertical. It results in a negative N bias below the layer of SR [Sokolovskiy, 2003].

Advantages of the direct retrieval are its flexibility, simplicity, and high quality in the lower and mid troposphere in the absence of SR. The direct retrieval only requires auxiliary T information, which has a number of advantages: 1) T is a commonly measured parameter, so RO N can be combined with T from many different observation techniques; 2) temperature in the troposphere is relatively stable in both time and space, so errors are expected to be smaller; 3) model T (often used in the direct retrieval) are very reliable at this point in time. Errors in the direct retrieval are dominated by RO N errors in the lower troposphere and by a-priori T errors in the upper troposphere.

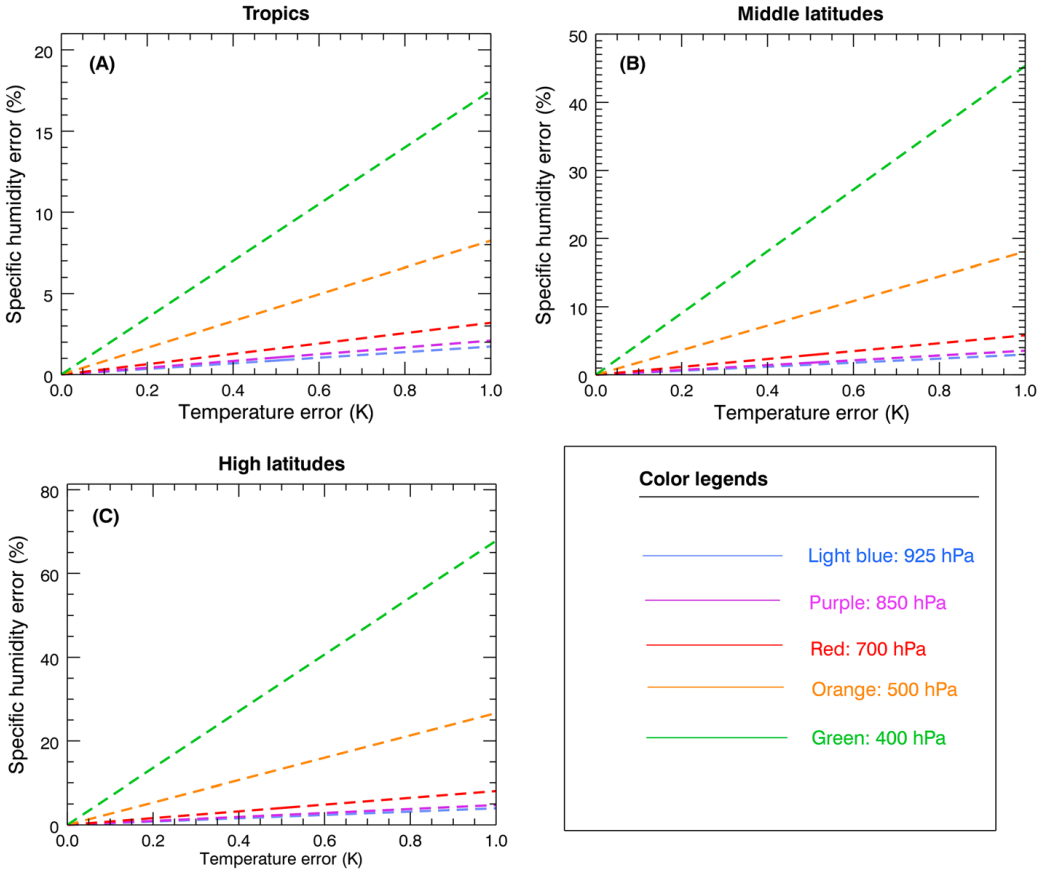

Figure 3.4.: RO specific humidity retrieval errors resulting from temperature T uncertainty for the (a) tropics (30°S to 30°N), (b) mid latitudes (30° to 60°), and (c) high latitudes (60° to 90°) for different pressure levels. Generally, the impact of T uncertainty is smaller when humidity is higher, such as at low altitudes and in the tropics. Note the different y-axis range for (a), (b), and (c). Figure taken from Vergados et al. [2014].

Disadvantages of the direct retrieval are its poor performance in the upper troposphere (starting at temperatures lower than 250 K [Kursinski et al., 1997]) and its inability to allow adjustment for the RO refractivity and a-priori temperature.

3.4.2. The One-Dimensional Variational retrieval

The 1D-Var retrieval combines RO refractivity or bending angle with a given priori atmospheric state (auxiliary T and e) to find the statistically optimal solution for p, T, and e. The goal is to find the maximum likelihood solution for $\mathbf{x}$ (the state

of the atmosphere) given the observations $\mathbf{y}_o$ and the background state $\mathbf{x}_b$. The statistically optimal solution is obtained by minimizing the cost function

$$J(\mathbf{x}) = \frac{1}{2}(\mathbf{x}-\mathbf{x}_b)^{\mathrm{T}}\mathbf{B}^{-1}(\mathbf{x}-\mathbf{x}_b) + \frac{1}{2}\left(H(\mathbf{x})-\mathbf{y}_o\right)^{\mathrm{T}}\mathbf{R}^{-1}\left(H(\mathbf{x})-\mathbf{y}_o\right). \quad (3.10)$$

The cost function is the summed difference of the current state ($\mathbf{x}$) to the background state ($\mathbf{x}_b$) and the observation ($\mathbf{y}_o$). The modeled observations $\mathbf{y}$ are given by $\mathbf{y} = H(\mathbf{x})$ where H is the forward operator to map from model state to observation space. $\mathbf{x}_b$ and $\mathbf{y}_o$ have associated uncertainties described by their respective error covariances $\mathbf{B}^{-1}$ and $\mathbf{R}^{-1}$. The errors are assumed unbiased and uncorrelated, and the distribution is assumed Gaussian.

The gradient of the cost function J indicates the direction of the minimum solution and is given as

$$\bigtriangledown_{\mathbf{x}} J = \mathbf{B}^{-1}(\mathbf{x}-\mathbf{x}_b) + \mathbf{H}^{\mathrm{T}}\mathbf{R}^{-1}\left(H(\mathbf{x})-\mathbf{y}_o\right) \quad (3.11)$$

where $\mathbf{H}^T$ is the adjoint operator of $\mathbf{H} = \frac{\partial H}{\partial \mathbf{x}}$, the tangent linear approximation of the observation operator H. The minimum of the cost function can be found iteratively, using helper parameters such as stepsize and number of iterations. A disadvantage of this method is the potential termination of the minimization algorithm at a local minimum of J.

A second method is the incremental formulation, where the cost function is defined as

$$J(\delta\mathbf{x}) = \frac{1}{2}\delta\mathbf{x}^{\mathrm{T}}\mathbf{B}^{-1}\delta\mathbf{x} + \frac{1}{2}\left(\mathbf{H}\delta\mathbf{x}-\mathbf{d}\right)^{\mathrm{T}}\mathbf{R}^{-1}\left(\mathbf{H}\delta\mathbf{x}\right)-\mathbf{d}) \quad (3.12)$$

with the increment $\delta\mathbf{x}$ and the innovation vector $\mathbf{d} = \mathbf{y}_o - \mathbf{H}\mathbf{x}_b$.

An advantage of the incremental formulation is decreased computational cost and the uniqueness of the minimum of J [COSMIC Project Office, 2005]. A disadvantage is that unlike Eq. (3.10), which uses the full state to provide the coefficients of the tangent linear model and adjoint model, the incremental formulation determines the coefficients only using the background. Therefore the coefficients for the tangent linear and adjoint calculations from the previous minimization must be used for a second run of minimizing J.

The 1D-Var retrieval has the potential for much better results in the mid and upper troposphere than the direct retrieval, but it is also much more complex. A toy model for the 1D-Var is shown in Figure 3.5 (taken and adapted from Lauritsen et al. [2017]). The total RO observed refractivity (O, blue) is given by the combination of the "dry" refractivity N_{d} and the "wet" refractivity N_{w} (i.e. the first and second term in Eq. (3.8)). The a-proiri refractivity (or background

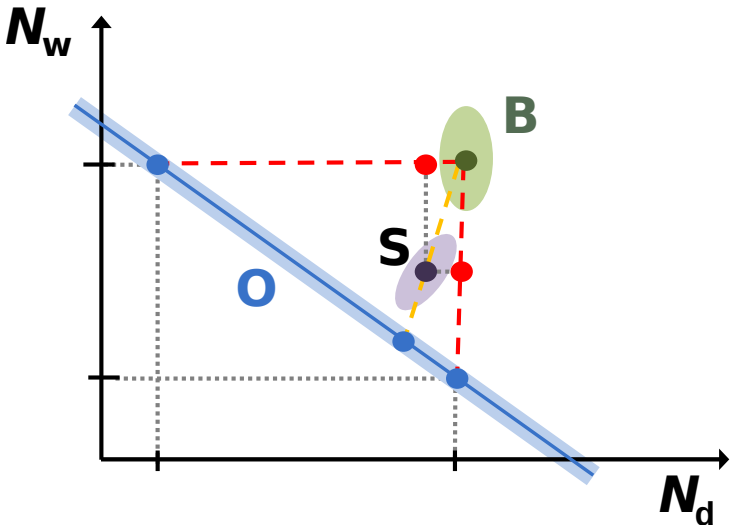

Figure 3.5.: 1D-Var toy model: RO observed refractivity O is a combination of the dry (N_d) and wet (N_w) refractivity, with assigned error (solutions all on the blue line, error indicated by blue shading). Background refractivity B and its error is shown by green dot and shaded area around. Depending on the errors allowed for each parameter (N, T, e), the solution can lie anywhere in the triangle determined by the boundaries given through O (blue solid line) and B (red dashed lines), assuming no biases and no correlation of the data sets. E.g., CDAAC assigns a very small error to RO N and forces the result onto the blue line, while DMI allows a large error for RO N and the solution can be very close to B. Figure taken and adapted from Lauritsen et al. [2017].

refractivity B and its uncertainty, green) has a different value. In a 1D-Var retrieval, O and B are combined for an optimal solution S. The errors assigned to any of the variables vary among the centers. E.g., while the DMI 1D-Var assigns a fairly larger error to O at lower levels and allows the solution S to approach the background B [Nielsen, 2016], the UCAR 1D-Var assigns only a very small error to O and forces it to stay close to the originally derived refractivity O. The former trusts the a-priori forecast and the refractivity output from the 1D-Var retrieval will be highly influenced by the a-priori. The latter keeps the refractivity output from the 1D-Var close to its original value while allowing a potential bias for refractivity in the lower troposphere.

While a 1D-Var retrieval is much more complex than a direct retrieval, it has the advantage of leaving room for adjustment for all involved variables. Thus errors for multiple variables can be minimized. With a correct setup, refractivity errors in the lower troposphere (as described in Section 3.4.1) can be minimized in the combined final a-priori and RO products.

4. Conclusions and summary

Humidity in the atmosphere plays a key role in many processes determining weather and climate, from the surface to the mesopause. The strong spatial and temporal variability of water vapor as well as its concentration change over several orders of magnitude in the vertical are a challenge for observing systems and thus make water vapor a relatively poorly monitored atmospheric constituent. There are many in-situ and remote sensing techniques that observe atmospheric humidity, but all of them leave gaps of uncertainty regarding accuracy, global availability, vertical resolution, and monitoring within and under cloudy regions. The Global Positioning System (GPS) Radio Occultation (RO) technique fills some of these gaps, as data are provided globally in all weather conditions with high vertical resolution and high accuracy and precision for the parameters temperature and refractivity. In recent years, focus has shifted also towards RO-derived humidity and its accuracy in the troposphere. Several factors influence the derived RO humidity: 1) the choice of the retrieval (direct versus One-Dimensional Variational (1D-Var)), 2) choice and quality of the auxiliary data required for the retrieval, and 3) quality of the RO refractivity in the retrieval. Atmospheric super-refraction causes a negative refractivity bias which translates into a negative humidity bias in the lowest few kilometers of the troposphere.

This thesis presents new results on the quality of tropospheric humidity data retrieved from RO measurements. Several other, state-of-the-art humidity data sets from in-situ and remote sensing techniques as well as two model analyses and reanalyses provide a baseline for the assessment. Strengths and weaknesses of all involved data sets are discussed.

The general setup for all studies includes:

1. Comparison of multiple different RO humidity retrievals. Different RO processing centers use different ways of implementing the retrieval of their choice, along with the choice of a-priori data, and (in the case of the 1D-Var) background error, observation error, and other tuning parameters. Differences among several retrievals demonstrate the structural uncertainty of RO-derived humidity.

2. Comparison of individual profiles or within tight co-location criteria rather than comparing data averaged over large temporal and spatial scales and vertical layer averaging. The vertical resolution of RO allows to resolve detailed humidity variability, and individual profile comparison avoids cancellation of opposite signs.

3. Evaluation in regions with challenging humidity conditions, including regions with cyclone activity, dry air intrusions, and atmospheric conditions that favor super-refraction.

Overall our results show that, in the absence of super-refraction, RO humidity retrievals can compete with other state-of-the-art humidity measurement techniques in the lower and mid troposphere, while also featuring high vertical resolution (a weakness of infrared and microwave sounders) and global coverage (a weakness of radiosonde and research aircraft observations).

Paper I demonstrates that RO reliably detects so-called "dry air intrusions", layers with very low humidity (relative humidity $< 10\,\%$) in the lower and mid troposphere. Both structure and intensity of dry layers are captured quite accurately by RO, as comparisons with high vertical resolution profiles from the National Science Foundation (NSF)/National Center for Atmospheric Research (NCAR) Gulfstream V research aircraft field experiment in the tropical western Pacific show. This comparison demonstrates the ability of RO to provide accurate humidity data also in these unfavorable dry conditions, where water vapor pressure is only a small fraction of the measured refractivity. Analyzing dry air intrusion occurrence on a global scale yields similar results for ECMWF Reanalysis Interim (ERA-Interim), Global Forecast System (GFS), and the independent RO technique.

In Paper II, high-resolution time series at four radiosonde stations in the tropical and subtropical western Pacific demonstrate the high quality of RO-derived humidity and the good agreement among four different RO humidity retrievals. Both observational and model data are compared among each other and to RO. The results validate the stability of the four retrievals and demonstrate that RO retrieved humidity has equal or better accuracy than both the standard radiosonde and Atmospheric Infrared Sounder (AIRS) at these specific locations in the lower and mid troposphere in the absence of super-refraction. Paper II shows the potential of RO to contribute valuable information on tropospheric humidity in data assimilation, especially when high-quality radiosonde data are unavailable (e.g., in the southern hemisphere and over oceans). In contrast to infrared or microwave sounders, the backbone of humidity data assimilation, RO can resolve strong vertical gradients of humidity and provide data below clouds.

Paper III takes a more mathematical approach to evaluate the quality of RO-derived humidity. We use the "N-corned hat method" with three data sets (i.e. Three-Cornered Hat (3CH) method) to estimate vertical profiles of error variances for several observational and model data sets. The computed error variances are smallest for ERA-Interim, which is a reasonable result considering ERA-Interim uses a thoroughly developed model and data assimilation system, and includes many independent, quality controlled observations [Dee et al., 2011]. For the studied four locations, RO data generally have smaller errors than the radiosonde data, which agrees with results from Paper II. The vertical error variance profiles show major differences for the RO direct retrieval and 1D-Var retrieval above 600 hPa.

Part II.

Published papers

Atmos. Meas. Tech., 10, 1093–1110, 2017
www.atmos-meas-tech.net/10/1093/2017/
doi:10.5194/amt-10-1093-2017

Atmospheric Measurement Techniques
Open Access
EGU

Tropospheric dry layers in the tropical western Pacific: comparisons of GPS radio occultation with multiple data sets

Therese Rieckh[1,2], Richard Anthes[1], William Randel[3], Shu-Peng Ho[1], and Ulrich Foelsche[4,2]

[1]COSMIC Program Office, University Corporation for Atmospheric Research, Boulder, Colorado, USA
[2]Wegener Center for Climate and Global Change, University of Graz, Graz, Austria
[3]National Center for Atmospheric Research, Boulder, Colorado, USA
[4]Institute for Geophysics, Astrophysics, and Meteorology/Institute of Physics, University of Graz, Austria

Correspondence to: Therese Rieckh (rieckh@ucar.edu)

Received: 29 July 2016 – Discussion started: 12 August 2016
Revised: 7 February 2017 – Accepted: 21 February 2017 – Published: 16 March 2017

Abstract. We use GPS radio occultation (RO) data to investigate the structure and temporal behavior of extremely dry, high-ozone tropospheric air in the tropical western Pacific during the 6-week period of the CONTRAST (CONvective TRansport of Active Species in the Tropics) experiment (January and February 2014). Our analyses are aimed at testing whether the RO method is capable of detecting these extremely dry layers and evaluating comparisons with in situ measurements, satellite observations, and model analyses. We use multiple data sources as comparisons, including CONTRAST research aircraft profiles, radiosonde profiles, AIRS (Atmospheric Infrared Sounder) satellite retrievals, and profiles extracted from the ERA (ERA-Interim reanalysis) and the GFS (US National Weather Service Global Forecast System) analyses, as well as MTSAT-2 satellite images. The independent and complementary radiosonde, aircraft, and RO data provide high vertical resolution observations of the dry layers. However, they all have limitations. The coverage of the radiosonde data is limited by having only a single station in this oceanic region; the aircraft data are limited in their temporal and spatial coverage; and the RO data are limited in their number and horizontal resolution over this period. However, nearby observations from the three types of data are highly consistent with each other and with the lower-vertical-resolution AIRS profiles. They are also consistent with the ERA and GFS data. We show that the RO data, used here for the first time to study this phenomenon, contribute significant information on the water vapor content and are capable of detecting layers in the tropics and subtropics with extremely low humidity (less than 10 %), independent of the retrieval used to extract moisture information. Our results also verify the quality of the ERA and GFS data sets, giving confidence to the reanalyses and their use in diagnosing the full four-dimensional structure of the dry layers.

1 Introduction

Water vapor is the most important greenhouse gas in the troposphere, yet it is still the parameter with the highest uncertainty in weather and climate models. All current humidity observation techniques have limitations for analyzing global water vapor fields. For example, nadir-viewing satellite instruments (e.g., infrared (IR) or microwave (MW) sensors in space) are restricted by their low vertical resolution. IR sounders cannot observe within and under clouds. Radiosonde (RS) coverage is sparse or nonexistent over the open oceans. The radio occultation (RO) method does not suffer from these limitations, but water vapor information can only be derived by using a combination of RO data and information on temperature from another source (observations or model). In addition, RO observations have significant errors in the lower tropical troposphere under superrefraction conditions (Sokolovskiy, 2003).

A number of studies have shown good agreement between RO and RS moisture profiles (e.g., Kishore et al., 2011; Ho et al., 2010). These climatological studies focus on comparisons of RO with the global radiosonde network rather than extremely dry air (relative humidities less than 10 %). In this paper we study the ability of RO to measure extremely dry

air in the tropics and subtropics, using for comparison high-resolution aircraft profiles, radiosondes, IR satellite data, and the ERA (Berrisford et al., 2011).

Dry regions of the tropical and subtropical lower and mid-troposphere have a strong radiative impact on the climate system through their ability to radiate heat to space, preventing a "runaway greenhouse effect" (Pierrehumbert, 1995). Furthermore, they suppress deep convection (Brown and Zhang, 1997), are connected to cumulus congestus cloud top heights (Johnson et al., 1996), and affect boundary layer height and humidity (Parsons et al., 2000).

A number of studies have addressed the so-called dry intrusions in the normally moist mid- and lower troposphere of the tropical western Pacific. They were first investigated during TOGA-COARE, the Coupled Ocean–Atmosphere Response Experiment of the Tropical Ocean and Global Atmosphere project (Webster and Lukas, 1992). Mapes and Zuidema (1996), using soundings from TOGA-COARE, found that dry layers are generally too dry and not warm enough to be interpreted as adiabatic displacements within the tropics. Instead they suggest a subtropical origin. Dry layers typically have strong horizontal and vertical moisture gradients and sharp temperature inversions at the lower edge. They are stabilized by radiative cooling of the underlying moist air and heating of the dry air layer, thus inhibiting convection.

Cau et al. (2005) investigated the radiative impact and origin of dry intrusions observed by RS profiles in the tropical western Pacific using 40-year European Centre for Medium-Range Weather Forecasts (ECMWF) reanalysis (ERA-40) wind and humidity data. They showed an outgoing longwave radiation increase of $3\,\mathrm{W\,m^{-2}}$ per 100 hPa for dry intrusions with relative humidities of less than 20 %, almost independent of altitude. They pointed out the importance of the humidity distribution in a climate change scenario, considering that outgoing longwave radiation is more sensitive to small humidity perturbations in dry environments than in moist regions. Cau et al. (2005) also pointed out that cloud occurrence above or below the dry intrusion reduces the radiative impact. Furthermore, they used back trajectories to show that most dry events were associated with air descending from the extratropics. In their follow-up study, Cau et al. (2007) evaluated the origins of dry air in the tropics and subtropics using trajectory simulations for ERA-40 data for January 1993. They found four major transport mechanisms: (1) the descending branch of extratropical baroclinic waves; (2) the equatorial flank of the jet around subtropical anticyclones; (3) transport at regions of minimum subtropical jet strength via equatorward descent across the jet exit; and (4) dry air centering in the upper troposphere between regions of deep convection (see also Fig. 9 in Cau et al., 2007).

Regarding dry layer occurrence, Casey et al. (2009) created a 5-year climatology on dry layers between 600 and 400 hPa over deep convective regions of the tropical oceans using AIRS (Atmospheric Infrared Sounder) data. Their results show large spatial and seasonal variability for different ocean basins, pointing out the limits of applying case study trends to the whole basin.

Finally, Randel et al. (2016) performed a detailed comparison between aircraft measurements from the CONvective TRansport of Active Species in the Tropics (CONTRAST) experiment and GFS meteorological analyses, demonstrating that the analyses accurately capture the behavior of subtropical dry layers. A global climatology from GFS data shows that the dry layers are a ubiquitous feature of the subtropics, with maximum occurrence frequency in the winter hemisphere (linked to the strongest subtropical jets). The subtropical dry layers are highly correlated with enhanced ozone in both hemispheres, arguing for a source in the extratropical upper troposphere–lower stratosphere (UTLS).

A number of studies confirmed the capability of RO measurements to monitor the dry atmosphere (above around 8 km; Foelsche et al., 2008, 2009) and for climate change detection (Leroy et al., 2006; Ho et al., 2009; Steiner et al., 2011; Ho et al., 2012). RO data feature inherent high accuracy and precision, high vertical resolution (100 to 200 m), all-weather capability, and long-term stability (Anthes, 2011), making them highly valuable for studying a large number of atmospheric phenomena. Vergados et al. (2015) studied the spatial variability of relative humidity (RH) from RO compared to ECMWF and MERRA (Modern-Era Retrospective analysis for Research and Applications), focusing on time-averaged seasonal behavior; these comparisons suggest an overall reliable behavior of RO-derived humidity fields. So far no study has focused on RO and extreme dryness ($\mathrm{RH} < 10\,\%$).

RH is computed from measured water vapor pressure and saturation water vapor pressure over liquid or ice, depending on the temperature. The liquid formulation is used according to Murphy and Koop (2005).

This paper is structured as follows: in Sect. 2 we summarize the RO technique, the CONTRAST field campaign, and all other data sets we used. In Sect. 3 we show some example profile comparisons, explain features of dry layers, and discuss the contributions of a priori (first-guess) data and RO observations in the one-dimensional variational (1D-Var) retrieval. Section 4 focuses on one specific case in detail. In Sect. 5, we give a short overview of the results using all collocation pairs available. Section 6 discusses the global occurrence of dry layers derived from RO data. Section 7 provides a summary and conclusions.

2 Data and methods

2.1 The RO method

The RO method (Melbourne et al., 1994; Hajj et al., 2002; Kuo et al., 2004) is a limb-sounding technique that provides near-vertical profiles of atmospheric refractivity N. The re-

lation of N to atmospheric temperature T, pressure p, and water vapor pressure e can be approximated by the Smith and Weintraub (1953) formula:

$$N = 77.6\frac{p}{T} + 3.73 \times 10^5 \frac{e}{T^2} + [\ldots]. \quad (1)$$

Additional terms accounting for contributions from liquid water and the ionosphere can be neglected or are accounted for earlier in the retrieval. In the so-called dry air retrieval, the "dry temperature" is computed using Eq. (1) under the assumption $e = 0$. For a detailed retrieval description, see Kursinski et al. (1997).

Water vapor pressure e in Eq. (1) cannot be determined from an observed N without ancillary temperature data from some other source (either observations, a model, or analysis). The two common techniques for this calculation are discussed in Appendix A, as well the influence of the ancillary data in the 1D-Var retrieval (Appendix B).

For this study, we downloaded data from CDAAC[1] (COSMIC Data Analysis and Archive Center) for the RO missions COSMIC (Constellation Observing System for Meteorology, Ionosphere and Climate; reprocessed data cosmic2013), GRACE (Gravity Recovery and Climate Experiment; post-processed), Metop-A (Meteorological Operational Polar Satellite A; reprocessed data metopa2016), Metop-B (Meteorological Operational Polar Satellite B; post-processed), and TerraSAR-X (post-processed).

CDAAC provides profiles of physical parameters, which are derived by using a 1D-Var retrieval (COSMIC, 2005)). In the 1D-Var, ERA profiles (interpolated to the location and time of the RO measurement) are used as the initial (first-guess or a priori) temperature and moisture profiles in the iteration procedure. Furthermore, CDAAC also provides these a priori profiles, and collocated profiles from other (re-)analyses. In this study we use these RO-collocated profiles from ERA and GFS for comparisons. ERA vertical profiles are provided at 25 hPa steps between 1000 and 750 hPa and at 50 hPa steps between 750 and 300 hPa, yielding a total of 19 levels below 300 hPa. GFS analyses are given at 50 hPa steps from 1000 to 300 hPa and at 975 and 925 hPa additionally, yielding a total of 16 levels below 300 hPa.

2.2 The CONTRAST experiment

The CONTRAST experiement was conducted over the western Pacific warm pool region during the season characterized by intense convective storms to study the impact of deep convection on chemical composition and ozone photochemical budget (Pan et al., 2017). The experiment was conducted from Guam (13.5° N, 144.8° E) using the NSF/NCAR Gulfstream V (GV) research aircraft during January and February 2014. During the campaign, 16 research flights were conducted. Most research flights included several vertical profiles (covering altitudes from 0.1 to 15.2 km), and together with take-offs and landings at Guam there were over 80 vertical profiles obtained during the experiment. We use the aircraft observations of temperature, pressure, and water vapor pressure to derive high-resolution vertical profiles of RH.

Water vapor was measured by the Vertical Cavity Surface Emitting Laser (VCSEL) hygrometer (absolute concentration of water vapor in molecules per cubic centimeter). It is designed to work throughout the troposphere (and also the lower stratosphere) and has an accuracy of ±6 % mixing ratio +0.3 ppmv and a precision of ≤ 3 % (see Zondlo et al., 2010, for details). Temperature was measured by two Harco heated total air temperature sensors (estimated accuracy: 0.5 °C; precision: < 0.01 °C), pressure was measured using the Paroscientific, Ltd. sensor model 1000 transducer (accuracy: 0.1 hPa, precision: < 0.01 hPa)[2]. From the CONTRAST netcdf files, the variables used for T, e, and p are ATX, EW_VXL, and PSXC.

2.3 ERA-Interim reanalysis

In addition to the RO-collocated ERA profiles (as described in Sect. 2.1), we downloaded ERA-Interim reanalysis fields from European Centre for Medium-Range Weather Forecasts (2009) for the time range of the CONTRAST experiment. They are available every 6 h at 00:00, 06:00, 12:00, and 18:00 UT. We use the data on the lowest 27 levels, from 1000 to 100 hPa. ERA uses a 4D-Var method and assimilates RS observations, AIRS radiances, and RO bending angles, among other in situ and satellite data (Dee et al., 2011).

2.4 Radiosonde, AIRS, and MTSAT-2 observations

RS data from Guam were downloaded from NOAA[3]. Data are available at approximately midnight and noon UT (10:00 and 22:00 local times, respectively). Measurements are taken at standard pressure levels and significant thermodynamic levels. To convert the pressure grid to altitude, we used a constant temperature gradient of 6.5 K km^{-1}.

AIRS is a cross-track scanning instrument on the NASA Aqua satellite. Its sun-synchronous, near-polar orbit is designed to cross the Equator from south to north at 13:30 local time. The NASA Goddard Sciences Data and Information Center provides AIRS retrieved data products, such as profiles of physical parameters (temperature, humidity) and trace gas constituents, on a daily basis. We downloaded the version 6 level 2 standard retrieval data[4].

MTSAT-2 is a geostationary satellite located over Australia, East Asia, and the western Pacific, operated by the

[1] http://cdaac-www.cosmic.ucar.edu/cdaac/

[2] https://www2.acom.ucar.edu/sites/default/files/seac4rs/StateParameters.pdf

[3] https://www.ncdc.noaa.gov/data-access/weather-balloon/integrated-global-radiosonde-archive

[4] ftp://airsl2.gesdisc.eosdis.nasa.gov/ftp/data/s4pa/Aqua_AIRS_Level2/AIRS2RET.006/

Japan Meteorological Agency. Detailed information can be found at Knapp (2008). MTSAT-2 carries an imaging telescope, backed by detectors for five wavelength channels.

We use data from the infrared channel (10.3 to 11.3 µm) and the water vapor channel (6.5 to 7 µm). We downloaded MTSAT-2 data from NOAA[5].

The sampling characteristics of the different observation and model data sets compared in this study vary greatly. The radiosonde and aircraft data are essentially point measurements. Radiosonde measurements are taken on standard pressure levels and significant thermodynamic levels, which results in the vertical resolution varying strongly within the profile (from less than 20 to almost 1000 m). The vertical resolution of the aircraft measurements is around 10 m. The horizontal footprint of the radio occultation profiles is ∼200 km while the vertical resolution is 100 to 300 m (Anthes, 2011). The AIRS level 2 products are reported on 28 standard pressure levels between 1100 and 0.1 hPa. They have a horizontal resolution of 50 km[6] and a vertical resolution of ∼1 km for temperature and ∼2 km for humidity[7]. For the two models used in this study, we used GFS and ERA interpolated to the time and location of the RO profile. Furthermore, we used the ERA field, for which the horizontal footprint is given by the horizontal grid size (0.7° × 0.7°, about 78 km × (68 to 78) km, depending on the latitude). The vertical resolution is given by the model pressure levels every 25 or 50 hPa (resulting in a vertical resolution between 200 to 1000 m).

Because both radiosondes and the aircraft measurements are essentially rapid-response point values and have high vertical resolution, they are capable of measuring turbulence and small-scale horizontal features (such as individual clouds). AIRS, RO, and models, in contrast, represent averages over much larger horizontal and vertical scales of observation (larger horizontal and vertical footprints). Thus different volumes of air are sampled and compared, leading to representativeness errors or differences due to their different horizontal and vertical footprints, especially when measuring fields with high temporal and spatial variability such as water vapor and relative humidity.

In addition, all the observations and model data occur at different locations and times. The RS, RO, and aircraft observations occur at different horizontal positions in the vertical (can be ∼100 to 200 km) as the balloons, satellites, and aircraft move during the "vertical" sounding. All of these differences make comparisons challenging, adding to the uncertainties associated with each individual data set, and must be considered when interpreting the results.

[5]http://www.ncdc.noaa.gov/gibbs/availability/2014-02-20

[6]http://disc.gsfc.nasa.gov/uui/datasets/AIRS2RET_V006/summary

[7]http://airs.jpl.nasa.gov/data/physical_retrievals

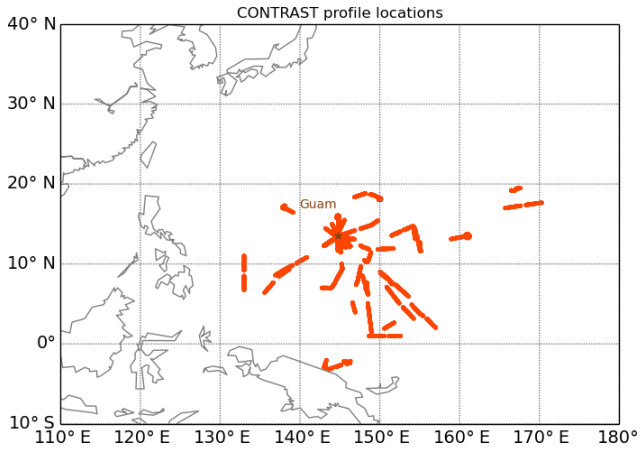

Figure 1. Profiles extracted from the CONTRAST flights during the experiment.

2.5 Collocating CONTRAST and RO profiles

From the 16 research flights, we extracted 75 profiles that extend over at least 6 km altitude and are within the region 5° S to 20° N latitude, 130 to 170° E longitude (Fig. 1). We tried different criteria for maximum time and distance for collocating RO with CONTRAST profiles. We made these comparisons only for the lowest 10 km, since RO observations do not provide reliable moisture values at altitudes above about 8 km (Kishore et al., 2011). Aircraft–RO profile pairs with less than 4 km overlap in the vertical were discarded (CONTRAST profiles are mostly limited by their maximum altitude; RO profiles are limited by their minimum altitude). The time and space coincidence criteria tested included 3 h and 600 km, 12 h and 300 km, and 24 h and 200 km, yielding 37, 41, and 24 profile pairs, respectively. Note that the shortest time windows in these criteria correspond to the longest spatial intervals; this is done to ensure enough pairs in sets matching each of the criteria. Using a criterion of the shortest time and space separation would not yield enough pairs to make the results as meaningful. As shown in Sect. 5 below, all three of our criteria gave similar results; thus we only show results for the 3 h and 600 km criteria.

3 Individual profile comparisons

Figure 2 shows an example of a dry layer sampled by the CONTRAST research flight 2 profile d (rf02d) and the collocated RO profile (Metop-A) for the parameters RH, T, q, and N. RH (upper left) shows a typical dry layer structure. There is a strong drop in RH at the bottom of the layer (at ∼2.5 km) from $>$ 80 to $<$ 10 %. All profiles (CONTRAST, RO, ERA, and GFS) show extremely dry air above 4 km. This layer is particularly thick and the RH remains below 20 % up to 10 km. The RO profile shows a remarkably similar shape when compared to CONTRAST, including the sharp humid-

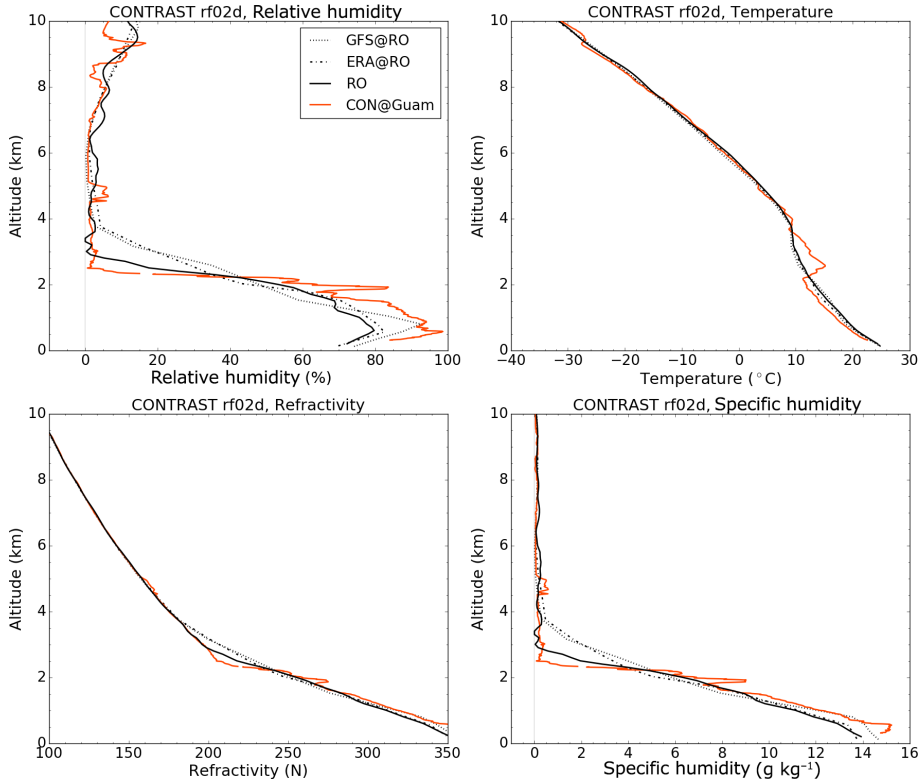

Figure 2. RH, T, N, and q profiles for CONTRAST (solid orange), RO (solid black), and RO-collocated profiles (ERA: dashed-dotted black; GFS: dotted black). Profile times and locations: CONTRAST on 14 January 2014, 00:58–01:11 UT, at 19.2° N, 166.5° E; RO on 13 January 2014, 22:18 UT, at 17.7° N, 164.4° E. The profiles are about 3 h and 390 km apart.

ity gradient at the bottom of the dry layer. Both ERA and GFS show a less sharp vertical moisture gradient, partly due to lower vertical resolution (RO provides 80 levels between the surface and 8 km, while ERA and GFS provide 18 and 15 levels, respectively). Profile differences are largest in the lowest 2.5 km, where RO and ERA RH are up to 20 % lower than the CONTRAST and GFS RH.

The aircraft T profile (Fig. 2, upper right) shows a strong inversion at the altitude of the bottom of the dry layer, as has been described by, e.g., Mapes and Zuidema (1996). Neither ERA and GFS nor RO not detect this strong inversion. RO generally has the capability to resolve such strong inversions in the middle and upper troposphere (Anthes, 2011). We conclude that RO not showing the T inversion could be explained by two factors: (1) CONTRAST and RO have different N values at this altitude (see Fig. 2, lower left). This implies that there has to be a difference in T and/or e at this altitude, too. (2) The 1D-Var retrieval generally produces an RO T close to the first-guess T, which does not show the inversion, and changes mainly e in the adjustment of the first-guess N towards the measured RO N.

Specific humidity q (lower right) shows extremely dry conditions above 2.5 km, but in less extreme cases dry layers are harder to detect using this parameter since it generally decreases exponentially with altitude. Thus we mainly use RH to investigate dry layers.

Figure 3 shows two more examples for CONTRAST–RO pairs (Metop-B and COSMIC-FM6). In the left panel, CONTRAST depicts a dry layer from 2.5 to 5.5 km, a relatively moist layer from 5.5 to 6.5 km, and very dry air from 6.5 to 8 km. The RO RH shows a very similar overall structure. Major differences are again in the lowest 2 km, where CONTRAST, GFS, and ERA RH are up to 20 % higher than RO RH, and between 2.5 and 4 km, where CONTRAST RH is up to 20 % lower. Furthermore, both GFS and ERA miss the 1 km thick moist layer around 6 km.

Figure 3, right, shows profiles with two drier layers in the mid-troposphere (at 3 and 5 km), but no extreme dryness. Both ERA and GFS show the correct overall shape of the RH profile, but they are often 20 to 30 % drier or moister than the CONTRAST RH. Again, RO captures more vertical structure than the models.

Generally both of these examples show how well the RO RH profile structure agrees with the one from CONTRAST.

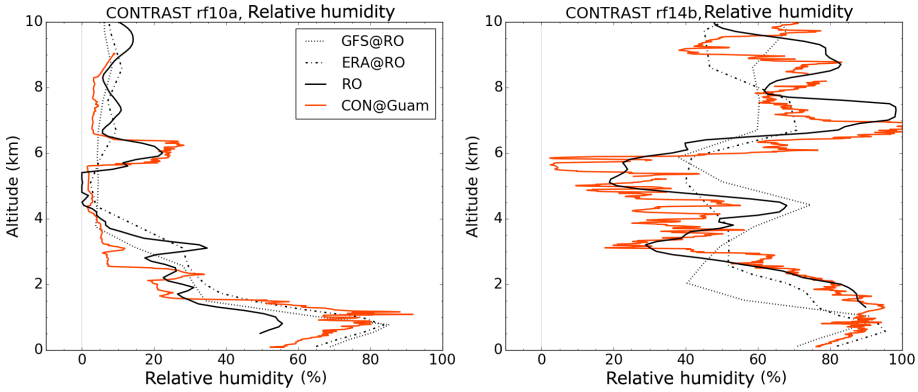

Figure 3. RH profile for CONTRAST (solid orange), RO (solid black), and RO-collocated profiles (ERA: dashed-dotted black; GFS: dotted black). Profile times and locations: CONTRAST (left) on 8 February 2014, 00:17–00:32 UT, at 13.5° N, 144.8° E; RO (left) on 7 February 2014, 22:57 UT, at 13.9° N, 148.1° E. CONTRAST (right) on 22 February 2014, 09:09–09:35 UT, at 13.5° N, 144.8° E; RO (right) on 22 February 2014, 12:06 UT, at 15.6° N, 148.1° E.

4 Case study: research flight 13

We found that many CONTRAST vs. RO profile pairs matched very closely, but some of the pairs showed RH differences of more than 60 % at certain levels. In this section we look into one of these cases in more detail to help explain these strong discrepancies. We consider two specific profiles, one measured by CONTRAST starting at Guam on 19 February 2014, 17:00 UT (Fig. 4, top), and one landing at Guam a few hours later (20 February 2014, 00:22 UT; Fig. 4, bottom).

For both cases, the left side shows the profiles for CONTRAST, the closest collocated RO, the RO-collocated ERA and GFS profiles, a RS launched at Guam (RS_G), and two AIRS profiles (one closest to Guam, labeled as $AIRS_G$; and one closest to the RO profile, labeled as $AIRS_{RO}$). Table 1 lists the time differences and distances between these profiles.

The right plots show the ERA RH field at 500 hPa, closest in time to the respective CONTRAST profiles. Also shown are the ERA ozone values and winds. The location of Guam is marked by a white X. CONTRAST, RO, RS, and AIRS profiles are labeled. Additional squares indicate other RO measurements. The color filling of the RO symbols (white squares) varies with the RH of the RO observation at this level, with the same color code as the ERA RH analysis (color bar). It is noteworthy that in almost all the cases the colors (and hence RH) of the RO observations agree very closely with the ERA values.

In Fig. 4, top left, all profiles show a deep dry layer. The depth of the layer varies slightly between the data sets. For CONTRAST, RS, and RO the depth with RH $\leq$ 10 % varies between 5 and 6.5 km. Both the ERA and GFS profiles and both AIRS profiles show a less sharp transition from moist to dry. The models also show a generally thinner dry layer. Major differences between the data sets occur below 2 km, where RO is significantly drier than all other data sets. The GFS profile agrees with the drier RO profile down to about 1 km and then strongly increases in RH. Sometimes superrefraction can cause a dry bias in RO profiles in the lowest few kilometers, which is probably the case in this particular RO profile.

Figure 4, top right, shows the ERA RH field at 500 hPa for the whole region. The large-scale region of very dry air extends from 110 to 180° E with a width of 1600 to 2200 km. It also shows the high horizontal variability of moisture. In some areas, extremely strong horizontal RH gradients occur, which clearly mark the edge of the dry air mass. In these areas RH can increase from less than 20 % to more than 70 % within 100 km. And since this is a model field, in which the gradients are likely to be smoother than the real atmosphere, the actual gradient could be even sharper. In this figure, it is also clearly visible that all the profiles from the left panel are located in the same air mass. Although ozone is not a focus of this study, we include contour lines of ozone in Fig. 4 (right panels) to illustrate that the ERA ozone fields show, in general, a coincidence of high ozone values with very dry air, suggesting the origin of at least some of the dry air from the lower stratosphere.

Next we consider the same region about 6 h later (Fig. 4, bottom panels). The profiles (left) show that the dry layer persists at Guam and is even deeper for CONTRAST. The RS profile and the AIRS profile at Guam still show a very deep dry layer. However, the RO shows only a very shallow dry layer, and RH increases from less than 20 % to more than 80 % between 3.5 and 4.5 km. The RO-collocated ERA and GFS profiles lack the dry layer entirely, having their RH minima at 45 and 50 %, respectively. They also both increase above 3.5 km to around 80 %. The AIRS profile at the RO location starts much drier than RO, ERA, or GFS at the surface. Overall, the AIRS profile has the same shape as RO, ERA, and GFS. It has weaker dry–moist transitions, similar to the (re-)analyses, and it stays drier than the other data sets

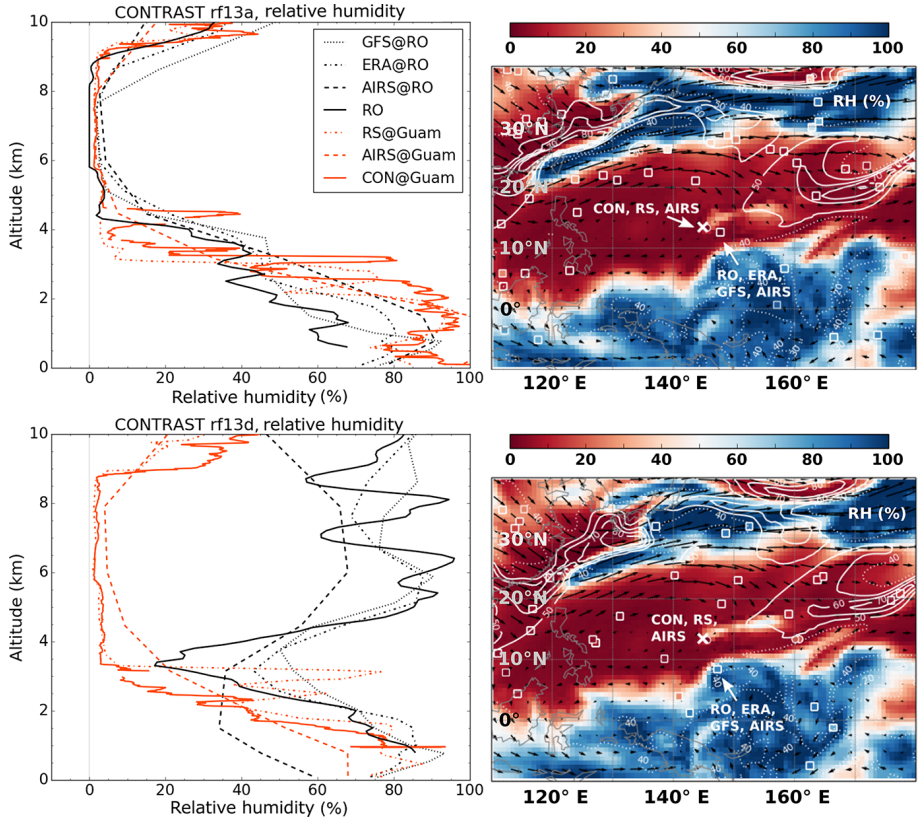

Figure 4. Two snapshots of the troposphere for (top) 19 February 2014 around 18:00 UT and (bottom) 20 February 2014 around 00:00 UT. Left panels: profiles for CONTRAST, RO, ERA, GFS, RS, and AIRS for the 2 days. Right panels: ERA RH (%, color shading) at 500 hPa, ozone values (white contours: values ≥ 50 ppbv are solid, otherwise dashed), and winds (black arrows). The white X marks the location of Guam. The locations of CONTRAST, RO, RS, and AIRS profiles are marked. Additional squares indicate other RO measurements. The squares marking the locations of the RO and CONTRAST locations are colored according to the RH of each profile at the 500 hPa level (matching the color bar).

Table 1. Distances and time differences between different the collocated profiles of rf13a and rf13d at the lowest point for each profile. Note that both the aircraft and RS profile will move away from Guam with higher altitudes and that RO profiles are also not completely vertical, especially in the lower and mid-troposphere.

Profile 13a					
	RO–CON	RS_G–CON	$AIRS_G$–CON	$AIRS_{RO}$–CON	$AIRS_{RO}$–RO
Distance (km)	345	4	16	331	18
Time diff (min)	−117	−289	−70	−70	47
Profile 13d					
	RO–CON	RS_G–CON	$AIRS_G$–CON	$AIRS_{RO}$–CON	$AIRS_{RO}$–RO
Distance (km)	599	4	34	588	128
Time diff (min)	87	1	236	234	147

above 4 km. Comparing the two AIRS profiles confirms the credibility of both RO and ERA: the strong difference between the aircraft profile and RO profile is neither an ERA nor an RO error, but caused by the combination of an imperfect collocation and strong spatial variability.

The lower right panel in Fig. 4 shows that the RO (and thus also the RO-collocated ERA and GFS) profiles are located in the moist air mass, just a few tens of kilometers from the edge of the moist–dry boundary, with much higher moisture

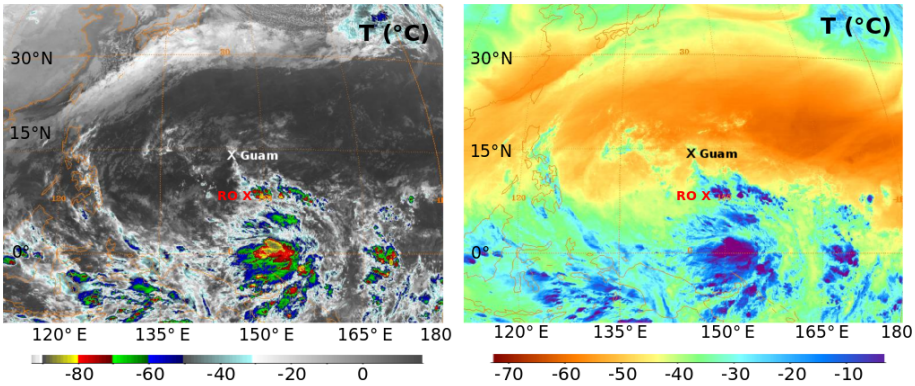

Figure 5. MTSAT-2 satellite images of brightness temperatures for 20 February 2014 around 00:00 UT. Left: MTSAT-2 IR (10.3 to 11.3 µm); right: MTSAT-2 IR water vapor (6.5 to 7 µm).

Table 2. Mean, RMS, and Pearson *R* coefficients for differences in relative humidity of RO–CONTRAST, ERA–CONTRAST, and GFS–CONTRAST for three different collocation criteria.

		3 h 600 km 644 points	12 h 300 km 687 points	24 h 200 km 419 points
RO–CONTRAST	mean	−4.0	−6.5	−0.2
	RMS	21.3	23.4	22.5
	Pearson *R*	0.782	0.758	0.751
ERA–CONTRAST	mean	−3.9	−5.4	0.6
	RMS	20.0	20.5	21.8
	Pearson *R*	0.807	0.807	0.760
GFS–CONTRAST	mean	−5.0	−6.3	−0.1
	RMS	20.7	21.4	21.9
	Pearson *R*	0.799	0.798	0.757

values above 3 km. This explains the very different profiles in the left panel.

Finally, Fig. 5 shows satellite images from MTSAT-2 for approximately the same time as the ERA field in Fig. 4, bottom right. The satellite images are cropped to the latitude and longitude range as ERA (as much as the different projections allowed). The Guam and RO locations are marked by an X.

The left panel depicts the brightness temperatures from IR in an atmospheric window (at 10.3 to 11.3 µm). It is derived from terrestrial IR radiation emitted by the Earth, cloud tops, and the atmosphere. Color enhancement shows the high, cold cloud tops south of Guam. Conditions are clear around Guam and the CONTRAST profile, but the RO profile is located in cloudy air.

The right panel shows the image from the MTSAT-2 water vapor channel. It depicts brightness temperatures derived from the water vapor emission spectrum between 6.5 and 7 µm. Higher amounts of water vapor absorb more radiation, which is re-emitted. Thus regions with high amount of water vapor, especially in the upper troposphere or above clouds, will have a higher brightness temperature. When compared to ERA (Fig. 4, bottom right), we see that the low RH region has a much lower brightness temperature than the moist region south of Guam.

5 Results of all collocations

To get a general overview of profile pair differences we computed statistics (not shown) and created scatter plots for all collocated profiles. Since humidity has a strong spatial variation (as seen in Fig. 4, right) and also varies strongly with time, we tested different sets of collocation criteria (described in Sect. 2.5). CONTRAST profiles are smoothed by taking 60 s averages in each profile (resulting in about 300–500 m vertical resolution). The RO profiles are interpolated to the related CONTRAST altitude grid. We did comparisons for RO and CONTRAST, ERA and CONTRAST, and GFS and CONTRAST. Generally, all three sets of collocation criteria and all data set comparisons show similar results for both the profile statistics and scatter plots. To illustrate the similarities, we show the mean, root mean square (RMS), and Pearson *R* correlation coefficient for RH for RO–CONTRAST, ERA–CONTRAST, and GFS–CONTRAST differences for all three criteria in Table 2. We

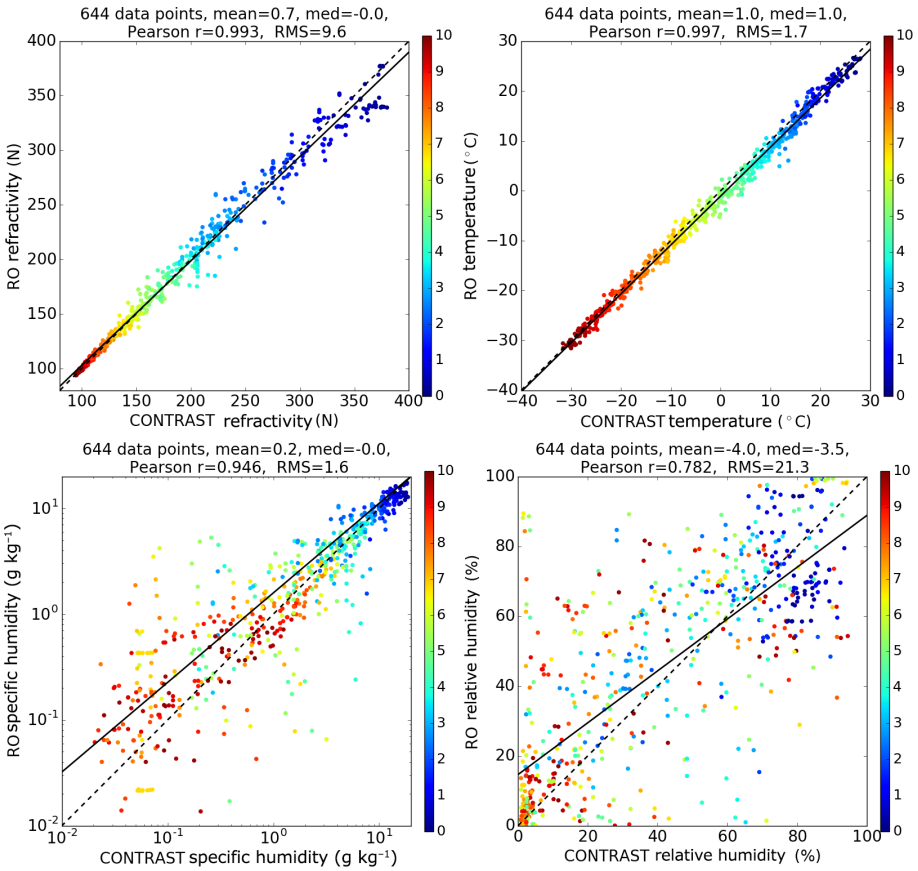

Figure 6. Scatter plots for N (top left), T (top right), q (bottom left, logarithmic scale), and RH (bottom right) for all 3 h 600 km collocation pairs for RO and CONTRAST. The color indicates the altitude of the measurement.

chose RH due to our focus on tropospheric moisture in this paper. Furthermore, RH is the only parameter without some inherent vertical correlation due to a general decrease with altitude (i.e., N, T, and q).

Figure 6 shows the scatter plots for refractivity N, temperature T, specific humidity q, and RH for RO compared to CONTRAST. The color of the dot indicates the altitude from 0 to 10 km as shown in the color bar. The black solid line is the fitted linear regression, and the dashed black line indicates perfect agreement between the two data sets (slope = 1, intercept = 0).

The upper left panel depicts the N comparison between RO and CONTRAST. N decreases exponentially with altitude, so the spread is larger at lower altitudes (blue) than at higher altitudes (red). Overall, there is a high correlation between the two data sets, and the fitted regression (solid black line) agrees well with the line of perfect agreement (dashed black line).

T (top right) also shows very good agreement (high correlation and little spread). We found a small warm bias of 0.5 to 1.5 K in CONTRAST temperatures when compared to any of the other data sets (RO, ERA, GFS). To test how much influence the collocation criteria have, we interpolated the ERA field to the CONTRAST profile location (spatial difference for latitude and longitude $< 0.5°$; time difference less than 30 min), which yielded a slightly smaller, more uniform bias. We conclude that there is likely a small T bias in the aircraft temperatures, possibly because of the effects of solar radiation as most of the flights occurred during the daytime.

The specific humidity q is depicted in the bottom left panel. The spread appears larger for low values (very dry air, $< 1\,\mathrm{g\,kg^{-1}}$), but the scales in this panel are logarithmic, which makes small differences of dry values appear larger. RO q values are biased positively compared to CONTRAST for low q values and biased negatively for high q values. Comparison on q between CONTRAST and GFS in Randel et al. (2016) shows a similar bias. Because of the highly accurate aircraft water vapor and temperature measurements and the very small scale of the observation (essentially a point observation), the CONTRAST measurements are capable of detecting extremes of dry and moist air more frequently than RO observations or model estimates, whose data represent averages over larger scales.

RH plots (bottom right) are highly scattered and have a lower correlation coefficient of around 0.78 with a bias and large spread in the data sets. The moist bias of RO for very

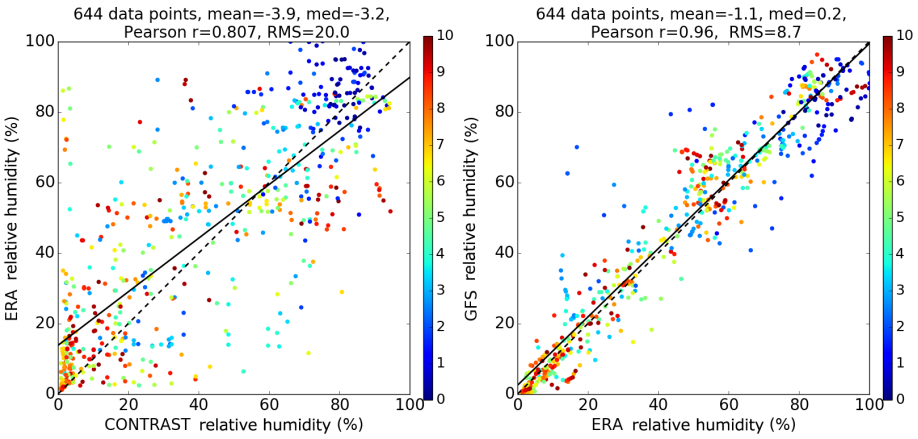

Figure 7. Scatter plots for RH for all 3 h 600 km collocation pairs for (left) ERA and CONTRAST on the 60 s smoothed CONTRAST altitude grid and (right) GFS and ERA on the ERA (pressure) grid. The color indicates the altitude of the measurement (left: km; right: hPa).

dry air was already noted in the paragraph above. Thus CONTRAST shows a much higher frequency of very low RH values than both RO (Fig. 6 lower right) and ERA (Fig. 7, left). The large spread can be explained by several factors: (1) RH is sensitive to both small variations in T and q, and thus representativeness differences or errors of both T and q contribute to differences in RH; (2) RH does not have a vertical profile with a mean structural or climatological variation in the vertical as N, T, q do (with an overall decrease with altitude); and (3) RH can undergo extremely strong changes in the vertical (80 % RH change over 1 km in Fig. 2), which leads to strong differences between two data sets if they do not capture this jump of RH at exactly the same altitude.

Furthermore, comparisons using 8 years of RS (two stations) and RO data using very tight collocation criteria (1 h, 100 km; figure not shown) also showed highly scattered data for RH, which indicates that collocation errors are not the dominant factor in the large scatter between RO and CONTRAST relative humidities.

Figure 7, left, compares ERA and CONTRAST RH, which shows a similar strong scatter as RO and CONTRAST. This suggests that the high variability in the CONTRAST data set also plays a role in the strong scatter of RH. Both the RO and ERA data sets are horizontally smoothed: RO shows an average over about 200 km (limb-sounding), and ERA is interpolated from the nearest grid points to the location of the profile (horizontal resolution is $< 0.7°$ in latitude and longitude). Finally, Fig. 7, right, compares GFS to ERA (this comparison is done on the ERA pressure grid). The correlation between the two analyses is high, but the scatter is surprisingly large considering these are smooth model data sets. This shows how highly variable RH is.

6 Global distribution

Having shown that the RO observations are capable of detecting extremely dry layers in the tropical western Pacific region, we carried out a global climatology of dry layers using only RO data. AIRS data have been used before to find tropical dry regions within areas of convection (OLR $< 240\,\mathrm{W\,m^{-2}}$; Casey et al., 2009); however, AIRS cannot provide reliable measurements below clouds.

Figure 8 shows the global occurrence (percentage of observations) for RH < 10 % on the 320 K potential temperature level for December–January–February (DJF) and June–July–August (JJA) 2014. We use the 320 K level because dry air travels from the stratosphere into the troposphere along isentropes. The 320 K level is at about 600 hPa or 4.5 km in the tropics and slopes to higher altitudes (∼9 km) in the extratropics. So the 320 K level represents the mid-troposphere in the tropics and the lower stratosphere in the extratropics.

Figure 8, left, shows the months DJF. Between 5 and 25° N, almost the entire latitude band shows an occurrence of dry air for 50 % of the time or more. The only break in the band is off the west coast of North and Central America. In some regions, dry layer occurrence is as high as 75 %, e.g., in parts of the Atlantic or near India and the Arab peninsula. Guam is located just on the edge of the band of high frequency of dry layer occurrence. In the SH, two regions with very strong occurrence are easy to identify: one off the west coast of South America, and one in the southern Atlantic Ocean.

In JJA (Fig. 8, right), dry layers occur over smaller regions of the world, but with a much higher frequency. In the SH, the entire region from mid-Atlantic via Africa and the Indian Ocean to Australia shows a frequency of occurrence of 80 to 100 % of the time. In the NH, only a region in the northern east Pacific and the northeast Africa/eastern Mediterranean region show moderate to high occurrence.

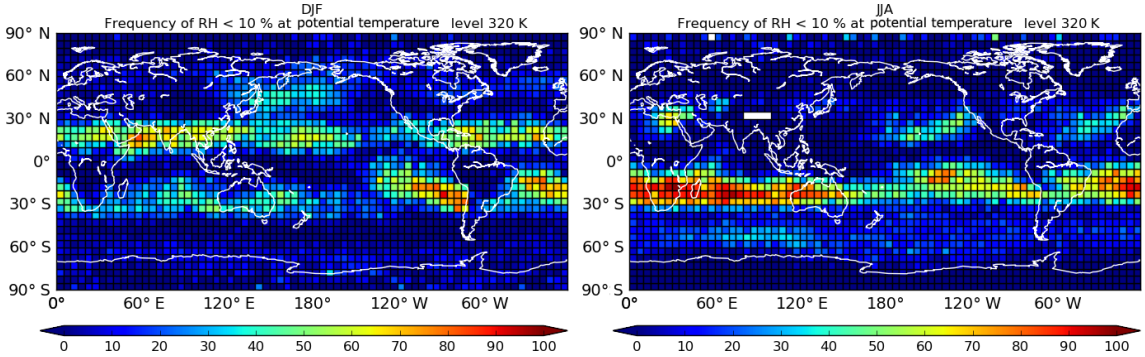

Figure 8. Frequency for RH < 10 % at the potential temperature level 320 K for DJF and JJA 2014.

Overall, dry layers occur throughout the year in some regions of the SH, but there is also a seasonal cycle with higher occurrence in the winter hemisphere. This behavior is consistent with the dry layer climatology derived from ERA (results not shown) and from GFS data in Randel et al. (2016).

7 Conclusions

In this study we compared GPS RO profiles with multiple data sets to examine their ability to detect extremely dry layers in the lower and mid-troposphere in the tropics and subtropics. The comparisons were made in the tropical western Pacific, making use of the field experiment in that region during January and February 2014. We used data from the NSF/NCAR GV research aircraft as a reference for RO profiles. This is a challenging comparison, since the aircraft provides high-resolution profiles consisting of point measurements (capturing a lot of variability), whereas the RO technique is a limb-sounding technique (measuring the limb-integrated value at each profile level). Furthermore, we used RS and AIRS profiles, as well as data from the GFS model and ERA reanalysis. Our main findings and conclusions are as follows:

1. Radio occultation is capable of detecting layers with very low humidity in the lower and mid-troposphere, despite the fact that the water vapor pressure is only a small fraction of the measured refractivity in dry air. Comparing RO to other types of observations also shows that the structure and intensity of dry layers are captured quite accurately.

2. Both simple and 1D-Var RO water vapor retrievals yield similar results, demonstrating the ability of RO to retrieve water vapor profiles with fine-scale vertical structure similar to that of the aircraft profile (Appendix A).

3. There is significant information content in the RO water vapor retrievals, and the 1D-Var retrieval does not depend strongly on an accurate first-guess (a priori) information (such as from ERA). However, poor a priori information for water vapor may have an effect of several Kelvin on the retrieved temperature (Appendix B).

4. When compared to CONTRAST, RO has a moist bias for low humidity values and a dry bias for high humidity values. Similar results are found when comparing RO to long records of tropical RS measurements (Appendix A).

5. Both the GFS and ERA analyses show the overall correct structure when compared with CONTRAST aircraft observations and RO. They often exhibit less small-scale vertical variations or sharp vertical gradients, probably due to lower vertical resolution.

6. A detailed case study illustrated how strong horizontal moisture gradients (more than 50 % RH change within 100 km) can yield nearby profile pairs that strongly disagree, even though they are close in space and time.

7. Globally, dry layers occur throughout the year, mainly between 10 and 30° N and S. Occurrence frequency is stronger in the winter hemisphere. The independent RO data confirm results from both ERA and GFS, which show a very similar seasonal occurrence of dry layers.

In summary, these diverse data sets show generally good agreement in spite of their large differences in sampling characteristics and technologies.

8 Data availability

For this study, we downloaded data from CDAAC (http://cdaac-www.cosmic.ucar.edu/cdaac/; COSMIC Data Analysis and Archive Center) for the RO missions COSMIC (Constellation Observing System for Meteorology, Ionosphere and Climate; reprocessed data cosmic2013), GRACE (Gravity Recovery and Climate Experiment; post-processed), Metop-A (Meteorological Operational Polar Satellite A; reprocessed data metopa2016), Metop-B (Meteorological Operational Polar Satellite B; post-processed), and TerraSAR-X (post-processed).

The CONTRAST data are available at https://data.eol.ucar.edu/dataset/383.012. The ERA data are available at the NCAR Research Data Archive: http://rda.ucar.edu/datasets/ds627.0/. The radiosonde data are available at https://www.ncdc.noaa.gov/data-access/weather-balloon/integrated-global-radiosonde-archive. The AIRS data have been downloaded from ftp://airsl2.gesdisc.eosdis.nasa.gov/ftp/data/s4pa/Aqua_AIRS_Level2/AIRS2RET.006/. MTSAT-2 data have been downloaded from http://www.ncdc.noaa.gov/gibbs/availability/2014-02-20.

Appendix A: RO water vapor retrievals

The two common techniques to retrieve physical temperature and water vapor profiles from RO are the so-called simple retrieval (Kursinski and Hajj, 2001) and the 1D-Var retrieval. For the simple retrieval, e is derived via Eq. (1) using the RO observed N, and T and p from an independent source (e.g., radiosonde, model, or analysis). Advantages of the simple retrieval are its simplicity and ease of calculation, and its independence of model moisture (and thus independence from errors in model moisture). Vergados et al. (2015) used the simple method for this reason, using ECMWF temperatures for the independent temperatures. Ware et al. (1996) (Eqs. 3 and 4) noted that for a perfect N and p, the error (difference) in e related to an error (difference) in T can be approximated by

$$\Delta e = \frac{2TN - 77.6p}{3.73 \times 10^5} \times \Delta T. \quad \text{(A1)}$$

The simple method provides good results ($\Delta e <$ 0.25 hPa) in the lower troposphere if the ancillary temperature data are reasonably accurate ($\Delta T <$ 1 K). In the 1D-Var procedure, a priori (first-guess or background) profiles of T and e are obtained from independent observations and adjusted toward the RO measurements by a statistical optimization procedure (Poli et al., 2002; COSMIC, 2005). The 1D-Var procedure considers the statistics of errors in the RO observations as well as the statistical errors in the a priori information, to achieve a consistent temperature and water vapor profile that minimizes, in a statistical sense, the errors in T and e.

Because both the 1D-Var and simple method are used in different studies to estimate water vapor, it is important to understand how the results from the two methods compare. In this Appendix we compare the two methods using the data in our study by first showing an example and then statistics using a large number of data pairs. Figure A1 shows the parameters RH, T, q, and e for the first-guess (ERA, solid) and retrieved from RO with the 1D-Var (dashed) and the simple retrieval (dotted) for an example profile.

The RH (top left) is very low between 4 and 9 km. The simple retrieval and the 1D-Var agree very well up to 4 km. At 4.2 and 6 to 9 km, the simple retrieval produces a negative RH (due to negative e values). In the simple retrieval, any error in T will produce an error in e, and for dry air (e close to zero) this error may lead to an unphysical negative value for e, q, and RH. The 1D-Var can theoretically also produce negative values in these situations, but it is artificially set to a very small positive value (10^{-6} hPa) in the COSMIC CDAAC 1D-Var retrieval.

The RO 1D-Var and first-guess (ERA) T (top right) agree very well; temperature differences are within 1.5 K throughout the profile. (The RO T in the simple retrieval assumes ERA T to be the truth, so it is identical to the ERA T in this figure.)

The bottom panels show q and e. Both parameters become negative above 4.2 km in the simple retrieval.

Generally, the moisture profiles derived from both the simple retrieval and the 1D-Var show much more vertical structure than the ERA profile; this structure comes from the vertical structure of the RO refractivity profile. The above example shows that the simple and 1D-Var methods give very similar results for temperature, specific humidity, water vapor pressure, and even relative humidity up to the bottom of the very dry layer (a little above 4 km) where the water vapor pressure becomes less than 0.1 hPa. The close agreement in this example is typical, as shown by a comparison of the simple and 1D-Var method over a large number of cases.

We compared values of T, q, and RH computed from the two methods, using ERA T directly for the simple retrieval and ERA T and q as the first guess for the 1D-Var estimates, against RS data from Vacoas, Mauritus (20.3° S, 57.5° E), which is located in a region that frequently contains very dry layers. We used the period 2006 to 2014, using collocation criteria of 2 h and 200 km. Because of large uncertainties in radiosonde humidity measurements above 10 km (Miloshevich et al., 2006), we focus on comparisons over 1000 to 200 hPa.

Scatter plots of q from the 1D-Var retrieval (left) and the simple retrieval (right) versus the independent radiosonde observations are shown in Fig. A2. The results are very similar with a correlation of 0.914 for the 1D-Var retrieval and 0.908 for the simple method.

Figure A3 uses the same data as above but shows the scatter plot of specific humidities from the 1D-Var versus simple retrieval. The retrieved values from the two methods are very similar with a correlation of 0.994. Approximately 15 points (blue, i.e., pressure altitudes of about 800 hPa) show 1D-Var values that are significantly higher than the simple values. We suspected that these points were from profiles where super-refraction occurs. In the case of super-refraction, N is biased negatively (Sokolovskiy, 2003) and e from the simple retrieval, which uses an accurate estimate of T, will be too low. In 1D-Var, the negative RO N bias will be mitigated to some extent and the resultant 1D-Var temperature will be too high and the water vapor pressure too low, but not as low as in the simple retrieval. Thus e from the simple method will be significantly lower than the e from the 1D-Var method under conditions of super-refraction.

To test this hypothesis, we checked all radiosonde profiles in the pairs for the criterion for super-refraction ($\mathrm{d}N/\mathrm{d}z < -157\,\mathrm{N\,km^{-1}}$). If a profile contained this critical value at some pressure level, we marked all data points of that profile with an X in Fig. A3. Indeed, most of the points with strong differences between 1D-Var and simple appear to occur with super-refraction.

We note that neither the 1D-Var nor the simple method for computing water vapor pressure at high altitudes

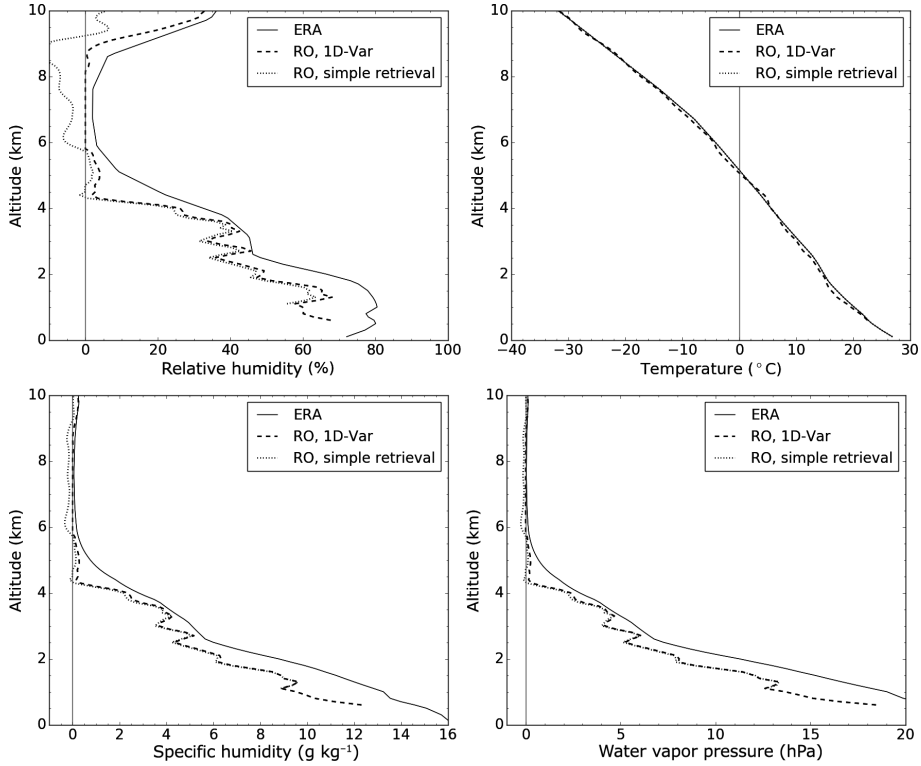

Figure A1. T, RH, q, and e profiles for ERA (solid, a priori), RO 1D-Var (dashed), and RO simple retrieval (dotted).

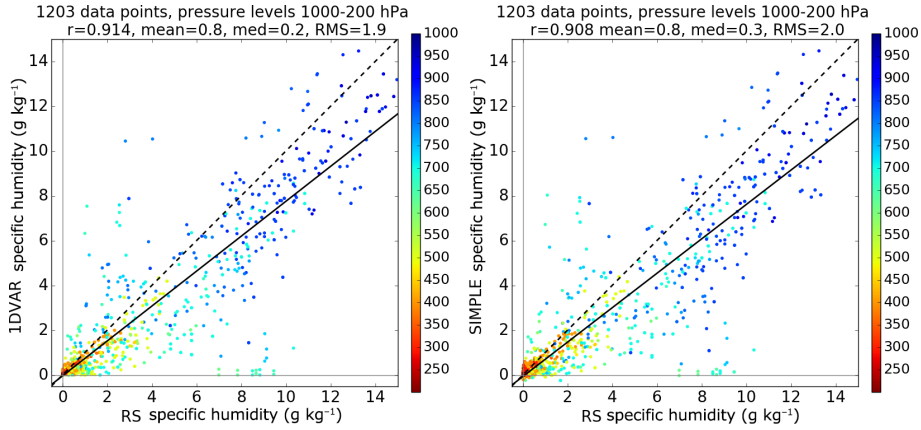

Figure A2. Specific humidity from the RO 1D-Var retrieval (left) and simple retrieval (right) versus radiosonde data. Collocation criteria: 2 h 200 km, altitude range 1000 to 200 hPa.

(p <200 hPa) from observed RO refractivity N will provide reliable estimates, because at these altitudes water vapor contributes very little to the refractivity; i.e., the so-called "wet" term in Eq. (1) is less than 1 % of the first, or "dry" term as noted by Wang et al. (2013). There is simply not enough information on water vapor pressure in refractivity at these altitudes to retrieve accurate estimates of water vapor. For example, the mean hurricane-season tropical atmosphere (Dunion and Marron, 2008) gives the following value of T at 200 hPa (about 12.4 km altitude): $T = -54.6\,^{\circ}\mathrm{C}$ (218.6 K). The saturation vapor pressure at this temperature is 0.04 hPa; thus for 100 % relative humidity, the dry term for N is 71.0 and the wet term is 0.31, or 0.4 % of the refractivity value. For the above values, the relationship between errors in e and T (Eq. A1) gives $\Delta e = 0.042\Delta T$ (hPa). So a temperature error (difference) of 0.5 K gives a difference in e of 0.021 hPa, which is more than 50 % of the saturation vapor pressure at this temperature. This example illustrates the difficulty in calculating water vapor pressure and relative humidity in the upper troposphere. Vergados et al. (2014) estimated the re-

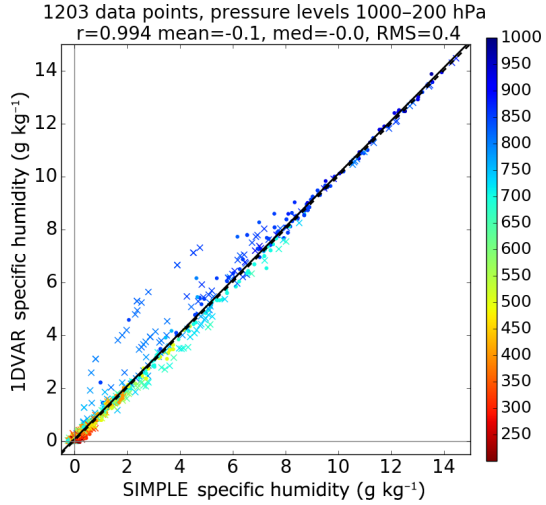

Figure A3. Specific humidity from the RO 1D-Var retrieval compared to the RO simple retrieval, using the same profiles as in Fig. A2. Points from profiles for which the collocated radiosonde profile experiences super-refraction are marked by an X.

trieval errors in specific humidity at different pressure levels (925, 850, 700, 500, and 400 hPa). They estimated that in the lower troposphere (925, 850, and 700 hPa) the percentage error in specific humidity for a temperature uncertainty of 1 K was less than 3 % in the tropics, 6 % in middle latitudes, and 10 % in high latitudes. At 400 hPa, the percent errors grew to 18 % in the tropics, 45 % in middle latitudes, and 67 % in high latitudes.

Appendix B: Contribution of RO in the 1D-Var

The simple retrieval of water vapor from N_{RO} and T_{model} is strongly dependent on an accurate T_{model} but completely independent from the a priori model water vapor. The 1D-Var, however, uses the a priori moisture from ERA. In this section we investigate how the 1D-Var retrieval reacts to a poor humidity first guess and how much information the RO refractivity contributes in the 1D-Var.

As an experiment to test the sensitivity of the 1D-Var method to the first-guess water vapor profile, we change e of the first guess such that the RH is greater than 20, 40, or 60 % within the lowest 10 km (leaving T unchanged). Then we use these fictitious a priori "high moisture" data in the 1D-Var retrieval. Figure B1 shows the results for the original RO and first guess and for the "high moisture" cases.

The top left panel shows RH: the three changed a priori profiles are clearly different from the original profile. At 4 km, the original profile shows a RH of < 5 %, while the changed ones are 20 (dark red), 40 (red), and 60 % (orange). Using these a priori in the 1D-Var yields the original (solid blue) RO and the "high moisture" ROs (solid, shades of red). The solid red lines all decrease strongly between 2.5 and 3 km and follow the shape of the original RO at all levels. Up to 5.5 km, the difference is between 2 and 6 %. Above that, the RH profiles begin to fan out and differences up to 20 % occur between 5.5 and 8 km. Overall, the results show that RO refractivity contributes significant information to the water vapor in the 1D-Var retrieval and strongly corrects for the artificially high moisture from the a priori profiles.

The top right panel in Fig. B1 shows that the RO T profiles show some differences due to the erroneous a priori water vapor profiles at all levels. Differences are < 1 K for the original and the 20 % a priori case and ~ 3 K for the original and the 60 % a priori case.

The lower panels of Fig. B1 depict q and e. They show how much the 1D-Var adjusts the high humidity values from the first guess towards the low, realistic humidity values.

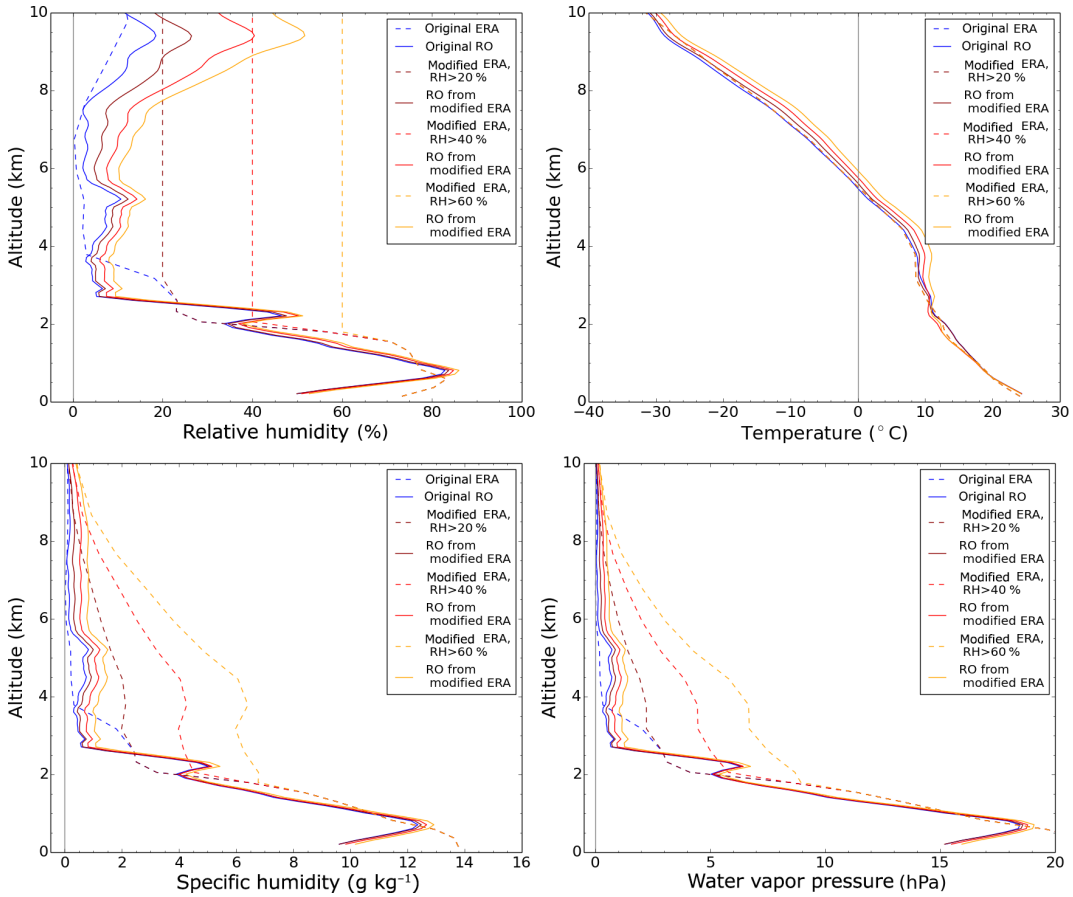

Figure B1. RH, T, q, and e profiles with the original ERA first guess (dashed blue), the original 1D-Var output (solid blue), the "high moisture" first guess (dashed, shades of red), and the 1D-Var output for the modified first guess (solid, shades of red).

Author contributions. Therese Rieckh and William Randel formulated the initial idea of this work. Richard Anthes and Shu-Peng Ho helped to develop the design of the study further. Together with Ulrich Foelsche, they contributed ideas and provided valuable feedback. Therese Rieckh collected the data, performed all the computational work and coding necessary, performed the analysis, and prepared the manuscript. Richard Anthes and William Randel contributed significantly to the data analysis and the writing.

Competing interests. The authors declare that they have no conflict of interest.

Acknowledgements. Therese Rieckh, Richard Anthes, and Shu-Peng Ho were supported by the NSF-NASA grant AGS-1522830. William Randel was supported through the NSF-UCAR cooperative agreement for the management of NCAR and NASA RNSS Science Team grant NNX12AQ18G.

The CONTRAST data set was provided by NCAR/EOL under sponsorship of the NSF (http://data.eol.ucar.edu/). The ERA data were provided by the Data Support Section of the Computational and Information Systems Laboratory, NCAR, which is sponsored by the NSF. We thank the COSMIC CDAAC team for providing the RO Level-2 data. We also thank Eric DeWeaver (NSF) and Jack Kaye (NASA) for their long-term advice and support to the COSMIC science program. COSMIC is supported by the National Space Office (NSPO) of Taiwan, NSF, NASA, NOAA, and the US Air Force.

We thank the two anonymous reviewers for their constructive comments and improving this manuscript.

Edited by: T. Islam
Reviewed by: two anonymous referees

References

Anthes, R. A.: Exploring Earth's atmosphere with radio occultation: contributions to weather, climate and space weather, Atmos. Meas. Tech., 4, 1077–1103, doi:10.5194/amt-4-1077-2011, 2011.

Berrisford, P., Kållberg, P., Kobayashi, S., Dee, D., Uppala, S., Simmons, A., Poli, P., and Sato, H.: Atmospheric conservation properties in ERA-Interim, Q. J. Roy. Meteorol. Soc., 137, 1381–1399, doi:10.1002/qj.864, 2011.

Brown, R. G. and Zhang, C.: Variability of midtropospheric moisture and its effect on cloud-top height distribution during TOGA COARE, J. Atmos. Sci., 54, 2760–2774, doi:10.1175/1520-0469(1997)054<2760:VOMMAI>2.0.CO;2, 1997.

Casey, S. P. F., Dessler, A. E., and Schumacher, C.: Five-Year Climatology of Midtroposphere Dry Air Layers in Warm Tropical Ocean Regions as Viewed by AIRS/Aqua, J. Appl. Meteorol. Clim., 48, 1831–1842, doi:10.1175/2009JAMC2099.1, 2009.

Cau, P., Methven, J., and Hoskins, B.: Representation of dry tropical layers and their origins in ERA-40 data, J. Geophys. Res., 110, D06110, doi:10.1029/2004JD004928, 2005.

Cau, P., Methven, J., and Hoskins, B.: Origins of Dry Air in the Tropics and Subtropics, J. Climate, 20, 2745–2759, doi:10.1175/JCLI4176.1, 2007.

COSMIC: Variational Atmospheric Retrieval Scheme (VARS) for GPS Radio Occultation Data, COSMIC technical report, version 1.1, University Corporation for Atmospheric Research, 2005.

Dee, D. P., Uppala, S. M., Simmons, A. J., Berrisford, P., Poli, P., Kobayashi, S., Andrae, U., Balmaseda, M. A., Balsamo, G., Bauer, P., Bechtold, P., Beljaars, A. C. M., van de Berg, L., Bidlot, J., Bormann, N., Delsol, C., Dragani, R., Fuentes, M., Geer, A. J., Haimberger, L., Healy, S. B., Hersbach, H., Hólm, E. V., Isaksen, L., Kållberg, P., Köhler, M., Matricardi, M., McNally, A. P., Monge-Sanz, B. M., Morcrette, J.-J., Park, B.-K., Peubey, C., de Rosnay, P., Tavolato, C., Tépaut, J.-N., and Vitart, F.: The ERA-Interim reanalysis: configuration and performance of the data assimilation system, Q. J. Roy. Meteorol. Soc., 137, 553–597, doi:10.1002/qj.828, 2011.

Dunion, J. P. and Marron, C. S.: A Reexamination of the Jordan Mean Tropical Sounding Based on Awareness of the Saharan Air Layer: Results from 2002, J. Climate, 21, 5242–5253, doi:10.1175/2008JCLI1868.1, 2008.

European Centre for Medium-Range Weather Forecasts: ERA-Interim Project, doi:10.5065/D6CR5RD9, 2009.

Foelsche, U., Borsche, M., Steiner, A. K., Gobiet, A., Pirscher, B., Kirchengast, G., Wickert, J., and Schmidt, T.: Observing upper troposphere-lower stratosphere climate with radio occultation data from the CHAMP satellite, Clim. Dynam., 31, 49–65, doi:10.1007/s00382-007-0337-7, 2008.

Foelsche, U., Pirscher, B., Borsche, M., Kirchengast, G., and Wickert, J.: Assessing the climate monitoring utility of radio occultation data: From CHAMP to FORMOSAT-3/COSMIC, Terr. Atmos. Ocean. Sci., 20, 155–170, doi:10.3319/TAO.2008.01.14.01(F3C), 2009.

Hajj, G. A., Kursinski, E. R., Romans, L. J., Bertiger, W. I., and Leroy, S. S.: A technical description of atmospheric sounding by GPS occultation, J. Atmos. Sol.-Terr. Phy., 64, 451–469, doi:10.1016/S1364-6826(01)00114-6, 2002.

Ho, S.-P., Kirchengast, G., Leroy, S., Wickert, J., Mannucci, A. J., Steiner, A. K., Hunt, D., Schreiner, W., Sokolovskiy, S., Ao, C., Borsche, M., von Engeln, A., Foelsche, U., Heise, S., Iijima, B., Kuo, Y.-H., Kursinski, E. R., Pirscher, B., Ringer, M., Rocken, C., and Schmidt, T.: Estimating the uncertainty of using GPS radio occultation data for climate monitoring: Intercomparison of CHAMP refractivity climate records from 2002 to 2006 from different data centers, J. Geophys. Res., 114, doi:10.1029/2009JD011969, 2009.

Ho, S.-P., Zhou, X., Kuo, Y.-H., Hunt, D., and Wang, J.-H.: Global evaluation of radiosonde water vapor systematic biases using GPS radio occultation from COSMIC and ECMWF analysis, Remote Sensing, 2, 1320–1330, doi:10.3390/RS2051320, 2010.

Ho, S.-P., Hunt, D., Steiner, A. K., Mannucci, A. J., Kirchengast, G., Gleisner, H., Heise, S., von Engeln, A., Marquardt, C., Sokolovskiy, S., Schreiner, W., Scherllin-Pirscher, B., Ao, C., Wickert, J., Syndergaard, S., Lauritsen, K. B., Leroy, S., Kursinski, E. R., Kuo, Y.-H., Foelsche, U., Schmidt, T., and Gorbunov, M.: Reproducibility of GPS radio occultation data for climate monitoring: Profile-to-profile inter-comparison of CHAMP climate records 2002 to 2008 from six data centers, J. Geophys. Res., 117, D18111, doi:10.1029/2012JD017665, 2012.

Johnson, R. H., Ciesielski, P. E., and Hart, K. E.: Tropical inversions near the 0°C Level, J. Atmos. Sci., 53, 1838–1855, 1996.

Kishore, P., Ratnam, M. V., Namboothiri, S., Velicogna, I., Basha, G., Jiang, J., Igarashi, K., Rao, S., and Sivakumar, V.: Global (50° S–50° N) distribution of water vapor observed by COSMIC GPS RO: Comparison with GPS radiosonde, NCEP, ERA-Interim, and JRA-25 reanalysis data sets, J. Atmos. Sol.-Terr. Phy., 73, 1849–1860, doi:10.1016/j.jastp.2011.04.017, 2011.

Knapp, K. R.: Scientific data stewardship of International Satellite Cloud Climatology Project B1 global geostationary observations, J. Appl. Remote Sens., 2, 023548, doi:10.1117/1.3043461, 2008.

Kuo, Y.-H., Wee, T.-K., Sokolovskiy, S., Rocken, C., Schreiner, W., Hunt, D., and Anthes, R. A.: Inversion and error estimation of GPS radio occultation data, J. Meteorol. Soc. Jpn., 82, 507–531, 2004.

Kursinski, E. R. and Hajj, G. A.: A comparison of water vapor derived from GPS occultations and global weather analyses, J. Geophys. Res., 106, 1113–1138, doi:10.1029/2000JD900421, 2001.

Kursinski, E. R., Hajj, G. A., Schofield, J. T., Linfield, R. P., and Hardy, K. R.: Observing Earth's atmosphere with radio occultation measurements using the Global Positioning System, J. Geophys. Res., 102, 23429–23465, doi:10.1029/97JD01569, 1997.

Leroy, S. S., Dykema, J. A., and Anderson, J. G.: Climate benchmarking using GNSS occultation, in: Atmosphere and Climate: Studies by Occultation Methods, edited by: Foelsche, U., Kirchengast, G., and Steiner, A. K., 287–302, Springer, 2006.

Mapes, B. E. and Zuidema, P.: Radiative-dynamical consequences of dry tongues in the tropical troposphere, J. Atmos. Sci., 53, 620–638, 1996.

Melbourne, W. G., Davis, E. S., Duncan, C. B., Hajj, G. A., Hardy, K. R., Kursinski, E. R., Meehan, T. K., Young, L. E., and Yunck, T. P.: The application of spaceborne GPS to atmospheric limb sounding and global change monitoring, JPL Publication, 147, 94–18, 1994.

Miloshevich, L. M., Vömel, H., Whiteman, D. N., Lesht, B. M., Schmidlin, F. J., and Russo, F.: Absolute accuracy of water vapor measurements from six operational radiosonde types launched during AWEX-G and implications for AIRS validation, J. Geophys. Res., 111, D09S10, doi:10.1029/2005JD006083, 2006.

Murphy, D. M. and Koop, T.: Review of the vapour pressures of ice and supercooled water for atmospheric applications, Q. J. Roy. Meteorol. Soc., 131, 1539–1565, doi:10.1256/qj.04.94, 2005.

Pan, L., Atlas, E., Salawitch, R., Honomichl, S., Bresch, J., Randel, W., Apel, E., Hornbrook, R., Weinheimer, A., Anderson, D., Andrews, S., Baidar, S., Beaton, S., Campos, T., Carpenter, L., Chen, D., Dix, B., Donets, V., Hall, S., Hanisco, T., Homeyer, C., Huey, L., Jensen, J., Kaser, L., Kinnison, D., Koenig, T., Lamarque, J., Liu, C., Luo, J., Luo, Z., Montzka, D., Nicely, J., Pierce, R., Riemer, D., Robinson, T., Romashkin, P., Saiz-Lopez, A., Schauffler, S., Shieh, O., Stell, M., Ullmann, K., Vaughan, G., Volkamer, R., and Wolfe, G.: The Convective Transport of Active Species in the Tropics (CONTRAST) Experiment, B. Am. Meteorol. Soc., 98, 106–128, doi:10.1175/BAMS-D-14-00272.1, 2017.

Parsons, D. B., Redelsperger, J.-L., and Yoneyama, K.: The evolution of the tropical western Pacific atmosphere–ocean system following the arrival of a dry intrusion, Q. J. Roy. Meteorol. Soc., 126, 517–548, doi:10.1002/qj.49712656307, 2000.

Pierrehumbert, R. T.: Thermostats, Radiator Fins, and the Local Runaway Greenhouse, J. Atmos. Sci., 52, 1784–1806, 1995.

Poli, P., Joiner, J., and Kursinski, E.: 1DVAR analysis of temperature and humidity using GPS radio occultation refractivity data, J. Geophys. Res., 107, D20, doi:10.1029/2001JD000935, 2002.

Randel, W. J., Rivoire, L., Pan, L., and Honomichl, S.: Dry layers in the tropical troposphere observed during CONTRAST and global behavior from GFS analyses, J. Geophys. Res., 121, 23, doi:10.1002/2016JD025841, 2016.

Smith, E. and Weintraub, S.: The constants in the equation for atmospheric refractive index at radio frequencies, Proc. IRE, 41, 1035–1037, 1953.

Sokolovskiy, S.: Effect of superrefraction on inversions of radio occultation signals in the lower troposphere, Radio Sci., 38, 3, doi:10.1029/2002RS002728, 2003.

Steiner, A. K., Lackner, B. C., Ladstädter, F., Scherllin-Pirscher, B., Foelsche, U., and Kirchengast, G.: GPS radio occultation for climate monitoring and change detection, Radio Sci., 46, RS0D24, doi:10.1029/2010RS004614, 2011.

Vergados, P., Mannucci, A. J., and Ao, C. O.: Assessing the performance of GPS radio occultation measurements in retrieving tropospheric humidity in cloudiness: A comparison study with radiosondes, ERA-Interim, and AIRS data sets, J. Geophys. Res., 119, 7718–7731, doi:10.1002/2013JD021398, 2014.

Vergados, P., Mannucci, A. J., Ao, C. O., Jiang, J. H., and Su, H.: On the comparisons of tropical relative humidity in the lower and middle troposphere among COSMIC radio occultations and MERRA and ECMWF data sets, Atmos. Meas. Tech., 8, 1789–1797, doi:10.5194/amt-8-1789-2015, 2015.

Wang, B.-R., Liu, X.-Y., and Wang, J.-K.: Assessment of COSMIC radio occultation retrieval product using global radiosonde data, Atmos. Meas. Tech., 6, 1073–1083, doi:10.5194/amt-6-1073-2013, 2013.

Ware, R., Exner, M., Gorbunov, M., Hardy, K., Herman, B., Kuo, Y., Meehan, T., Melbourne, W., Rocken, C., Schreiner, W., Sokolovskiy, S., Solheim, F., Zou, X., Anthes, R., Businger, S., and Trenberth, K.: GPS Sounding of the Atmosphere from Low Earth Orbit: Preliminary Results, B. Am. Meteorol. Soc., 77, 1, 1996.

Webster, P. J. and Lukas, R.: TOGA-COARE: The Coupled Ocean–Atmosphere Response Experiment, B. Am. Meteorol. Soc., 73, 1377–1416, 1992.

Zondlo, M. A., Paige, M. E., Massick, S. M., and Silver, J. A.: Vertical cavity laser hygrometer for the National Science Foundation Gulfstream-V aircraft, J. Geophys. Res., 115, D20309, doi:10.1029/2010JD014445, 2010.

Atmos. Meas. Tech., 11, 3091–3109, 2018
https://doi.org/10.5194/amt-11-3091-2018

Atmospheric Measurement Techniques
Open Access
EGU

Evaluating tropospheric humidity from GPS radio occultation, radiosonde, and AIRS from high-resolution time series

Therese Rieckh[1,2], **Richard Anthes**[1], **William Randel**[3], **Shu-Peng Ho**[1], **and Ulrich Foelsche**[4,2]

[1]COSMIC Program Office, University Corporation for Atmospheric Research (UCAR), Boulder, Colorado, USA
[2]Wegener Center for Climate and Global Change (WEGC), University of Graz, Graz, Austria
[3]National Center for Atmospheric Research (NCAR), Boulder, Colorado, USA
[4]Institute for Geophysics, Astrophysics, and Meteorology/Institute of Physics, University of Graz, Graz, Austria

Correspondence: Therese Rieckh (rieckh@ucar.edu)

Received: 29 December 2017 – Discussion started: 25 January 2018
Revised: 29 April 2018 – Accepted: 2 May 2018 – Published: 30 May 2018

Abstract. While water vapor is the most important tropospheric greenhouse gas, it is also highly variable in both space and time, and water vapor concentrations range over 3 orders of magnitude in the troposphere. These properties challenge all observing systems to accurately measure and resolve the vertical structure and variability of tropospheric humidity. In this study we characterize the humidity measurements of various observing techniques, including four separate Global Positioning System (GPS) radio occultation (RO) humidity retrievals (University Corporation for Atmospheric Research (UCAR) direct, UCAR one-dimensional variational retrieval (1D-Var), Wegener Center for Climate and Global Change (WEGC) 1D-Var, Jet Propulsion Laboratory (JPL) direct), radiosonde, and Atmospheric Infrared Sounder (AIRS) data. Furthermore, we evaluate how well the ERA-Interim reanalysis and NCEP Global Forecast System (GFS) model perform in analyzing water vapor at different levels. To investigate detailed vertical structure, we analyzed time–height cross sections over four radiosonde stations in the tropical and subtropical western Pacific for the year 2007. We found that the accuracy of RO humidity is comparable to or better than both radiosonde and AIRS humidity over 800 to 400 hPa, as well as below 800 hPa if super-refraction is absent. The various RO retrievals of specific humidity agree within 20 % in the 1000–400 hPa layer, and differences are most pronounced above 600 hPa.

1 Introduction

Tropospheric humidity is one of the key parameters driving weather and climate, and it plays an important role in the development of many extreme events. To accurately model current and future climate, it is crucial to understand the distribution, transport, and vertical structure of tropospheric water vapor. However, measuring water vapor accurately is a great challenge, as it is highly variable on both spatial and temporal scales, and its tropospheric concentration varies over 3 orders of magnitude between the tropical planetary boundary layer (PBL) and the tropopause. At present, no single observing system can provide accurate tropospheric humidity data on a global scale with high vertical resolution.

Passive (microwave and infrared) nadir-sounding systems provide data globally, but with relatively low vertical resolution. Weighting functions are used to quantify vertically resolved humidity information, and these vertical scales are large (2 to 3 km) compared to the variability of water vapor in the vertical. Furthermore, infrared-based systems cannot provide data within or below clouds.

Radiosonde (RS) balloon measurements are launched globally, although with sparse coverage in many areas, such as over oceans or in the Southern Hemisphere. They can have a high vertical resolution, but data quality varies strongly depending on the sensor type (Miloshevich et al., 2006; Ho et al., 2010). Operational weather forecasting still benefits greatly from RS measurements, but the current global RS network is neither designed nor suitable for detecting and monitoring climate change. First, many different sensor types are used globally, each with their unique known and un-

Published by Copernicus Publications on behalf of the European Geosciences Union.

known biases. Second, sensor types at different locations change over time, and these changes have been poorly documented in the past, which can lead to artificial trends or jumps in the station's record (Dai et al., 2011). The GCOS (Global Climate Observing System) Reference Upper-Air Network (GRUAN) aims to address this issue by providing long-term high-quality vertical profiles of selected essential climate variables, including an estimate of the measurement uncertainty (Bodeker et al., 2016). GRUAN will play an important role for calibrating data from other global networks; however, at this point in time certified data are available at only a few locations with a relatively short time range (less than 4 years).

Research aircraft can provide high-quality, high-resolution profiles, but these missions are infrequent and cannot provide a complete global picture continuously over time by themselves. They are, however, important to evaluate measurements from other observing systems or models (Rieckh et al., 2017).

The Global Positioning System (GPS) radio occultation (RO) technique provides near-vertical profiles of refractivity with high vertical resolution and high accuracy and precision. Other features of the RO technique are global coverage, all-weather capability, and SI traceability. Profiles penetrating down into the lower troposphere became available with open-loop tracking (Sokolovskiy et al., 2006). Since refractivity depends on temperature and water vapor pressure, tropospheric specific humidity can be derived from refractivity via a so-called direct retrieval (using ancillary temperature information) or a one-dimensional variational retrieval (1D-Var), which finds the optimal solution for water vapor pressure, temperature, and refractivity, taking their prescribed errors into account. Thus the RO water vapor retrievals and their quality vary depending on the a priori (and the accuracy of the prescribed data) and inversion method used. Several RO processing centers currently provide RO water vapor profile retrievals: University Corporation for Atmospheric Research (UCAR), Jet Propulsion Laboratory (JPL), Danish Meteorological Institute (DMI), and Wegener Center for Climate and Global Change (WEGC).

The above observing techniques have been used to investigate the global humidity distribution, trends, and radiative impact. RO, despite being a relatively young observing technique, has shown the potential to provide data of climate benchmark quality for refractivity and temperature between about 8 and 25 km (Ho et al., 2009, 2012; Steiner et al., 2013). The quality of RO humidity is subject to research since ancillary data are required to retrieve humidity from refractivity. Kursinski et al. (1995) provided a first estimate for water vapor accuracy of less than 5 % for individual profiles in the boundary layer and 20 % up to about 7 km. Chou et al. (2009) found humidity differences smaller than 40 % below 7 km for individual profile comparisons between dropsondes and RO. For observations near strong typhoons, they found differences up to 100 % in the mid- and upper troposphere. Regarding global specific-humidity distributions, Chou et al. (2009) found good agreement within 15 % between RO and Atmospheric Infrared Sounder (AIRS) but significant discrepancy between NCEP/NCAR reanalysis and RO humidity. Ho et al. (2010) showed that UCAR COSMIC (Constellation Observing System for Meteorology, Ionosphere, and Climate) water vapor profiles agree well with those of European Centre for Medium-range Weather Forecasts (ECMWF) analysis over different regions, demonstrating the quality of the RO humidity data. Furthermore, they used RS and RO co-located data to identify biases of various RS types. Wang et al. (2013) also used UCAR COSMIC water vapor products and global RS data with very strict co-location criteria (1 h, 100 km) to verify the quality of UCAR RO humidity and found a mean specific-humidity bias of $-0.012\,\mathrm{g\,kg^{-1}}$, with a standard deviation of $0.666\,\mathrm{g\,kg^{-1}}$ over the 925–200 hPa layer. Ladstädter et al. (2015) compared WEGC RO profiles from multiple missions to a 5-year record of GRUAN RS profiles (both of which have the potential to serve as reference observations in the GCOS) and to a standard 11-year record of RS profiles (Vaisala RS90/92). Vaisala RS90/92 shows a dry bias of 40 % in the troposphere compared to RO, whereas GRUAN, with an elaborate humidity bias correction scheme, agrees within 5 % with RO below 300 hPa. Ladstädter et al. (2015) state that the good agreement of the RO and GRUAN RS data sets strongly encourages further development and advancement of both systems for the benefit of future climate monitoring and research. Vergados et al. (2015) compared relative humidity (RH) of JPL RO, ECMWF ERA-Interim reanalysis, and Modern-Era Retrospective analysis for Research and Applications (MERRA) in the tropics and showed that, from a climatological standpoint, MERRA and JPL RO are in agreement, whereas the ECMWF reanalysis is drier. Vergados et al. (2018) compared JPL and UCAR RO humidity data sets to MERRA, ERA-Interim, and AIRS from 2007 to 2015 for the $\pm 40°$ latitude range between 700 and 400 hPa. They found that both RO humidity retrievals agree well with MERRA and ERA-Interim, but the JPL retrieval is overall moister than all other data sets, while both the UCAR retrieval and AIRS are overall drier than all other data sets.

All of the above work considered differences averaged over large geographical regions and long time periods (a month or longer). While useful for climate and error estimations, these averages obscure variability that takes place on smaller temporal and spatial scales. Case studies fill this gap, but they often focus on a single particular event that occurs over only a few days.

In this study we focus on the water vapor variability in both a temporal and spatial sense by comparing data from multiple observing techniques (RO, RS, AIRS) and model (re)analyses (ERA-Interim, Global Forecast System (GFS)) at particular locations in the tropics and sub-tropics over an entire year. We chose the year 2007, when the maximum number of COSMIC RO profiles was available (COS-

MIC was launched in 2006; Anthes et al., 2008). We compare each of these individual data sets with co-located ERA-Interim humidity results for (a) the surface to the upper troposphere, (b) four locations, (c) four seasons, and (d) during typhoon passages. We quantify the structural uncertainty of RO-derived humidity profiles in the troposphere, which results from different inversion implementations and a priori. To understand how the RO humidity data sets are different from other humidity products, we collected RS–ERA pairs, AIRS–ERA pairs, and GFS–ERA pairs near the four RS stations. Although these data pairs may not sample the same local times, the errors due to local time sampling differences are probably small over these oceanic regions.

As humidity varies strongly in time and space, this study allows us to show in detail how humidity conditions change over time, both daily and seasonally, and how atmospheric conditions affect the ability of these data sets to provide accurate and precise humidity information. We can identify high-frequency variability and patterns at selected locations that would be obscured if only statistical parameters were analyzed.

We focus on several challenging locations in the tropics and sub-tropics where water vapor is highly variable. We show the entire 1000–400 hPa range to show how data quality for different observing and modeling systems varies with altitude. For example, the humidity data from many RS sensors are biased in the mid- and upper troposphere. RO-derived humidity can be biased in the lowest few kilometers (due to super-refraction in the atmosphere) and is unreliable once temperatures get as low as 250 K in the upper troposphere (around 350 hPa in the tropics). Using data from 1000 to 400 hPa without layer averaging allows us to identify details in the vertical humidity structure as measured by these systems.

ERA-Interim reanalysis (hereafter ERA) is used as a reference for all comparisons. Although all data sets used in this comparison are assimilated in the ERA, comparisons are still valuable since (i) data from a large number of different observing techniques are assimilated (number of assimilated observations more than 10^7 per day in 2010 (Dee et al., 2011), thus lowering the impact of any single observation), and (ii) the RO uncertainties used in data assimilation are large in the mid- and lower troposphere, and hence RO makes a relatively small contribution in the ERA reanalysis. In the ERA, the standard deviation of the RO observation error distribution (in bending angle space) is assumed to decrease linearly with increasing height, from 20 % at the surface to 1 % at 10 km impact height (Poli et al., 2010).

In a companion paper (Anthes and Rieckh, 2018), these data sets are compared statistically in different ways to estimate the error variances of each data set. This method indicates that the ERA-Interim data set has the smallest errors in refractivity, temperature, specific humidity, and relative humidity from 1000 to 200 hPa. The current paper sets the stage for this statistical comparison by describing the data sets in detail and showing how they vary over the year at the four locations.

The structure of this paper is as follows: Sect. 2 explains the data sets used in this study. Section 3 shows an overview of the results for the different observing systems, which are analyzed in greater detail in Sect. 4. Section 7 provides a summary and conclusions.

2 Data and method

2.1 Radio occultation

Radio occultation (RO) is a limb-sounding technique that provides near-vertical profiles with high vertical resolution of bending angles (Melbourne et al., 1994; Hajj et al., 2002), which can be used to retrieve atmospheric refractivity N. N can be related to atmospheric temperature T, pressure p, and water vapor pressure e via the Smith–Weintraub formula (Smith and Weintraub, 1953):

$$N = 77.6\frac{p}{T} + 3.73 \times 10^5 \frac{e}{T^2} + [\ldots]. \quad (1)$$

The contribution to N from liquid water (the terms in [...] in Eq. 1) can be neglected in most conditions (Ho et al., 2018). When e is negligible (at temperatures lower than 250 K; Kursinski et al., 1997), the second term is assumed zero and atmospheric temperature can be computed using Eq. (1).

In the troposphere, where water vapor content is significant, Eq. (1) is ambiguous and ancillary temperature data from another data source (usually model or analysis temperature) are required to solve for e. Direct retrievals use a prescribed T from another source to derive e. In a 1D-Var retrieval, a cost function is minimized to find the optimal solution for e, T, and N with their prescribed errors (Poli et al., 2002). In this study, three different RO retrievals and four different humidity retrievals are compared in order to provide an indication of the uncertainty in RO-derived water vapor.

GPS RO humidity accuracy varies depending on the choice of retrieval (direct versus 1D-Var retrieval). For a direct retrieval, humidity accuracy is determined by both the quality of the a priori temperature (Vergados et al., 2014, Fig. 1) and the refractivity accuracy. For the 1D-Var retrieval, humidity accuracy depends on the a priori temperature and humidity quality, the GPS RO refractivity accuracy, and the error variances for the input parameters. A general estimate for RO specific-humidity accuracy is given in Vergados et al. (2018) (and references therein) as $\sim$ 10–20 %.

2.1.1 UCAR 1D-Var

A one-dimensional variational (1D-Var) retrieval generally uses an a priori state of the atmosphere (background vertical profile), an observable (RO refractivity or bending angle), and their specified associated errors to minimize a quadratic

cost function. At COSMIC Data Analysis and Archive Center (CDAAC), ERA profiles of temperature and humidity are used as background, which are interpolated to the time and location of the RO (accounting for tangent point drift during the occultation). The humidity retrieval allows specified errors for both T and e, but only a very small error for bending angle/refractivity. CDAAC provides the resulting profiles of N, T, e, and p (wetPrf[1]), hereafter called UCAR 1D-Var.

2.1.2 UCAR direct

A direct retrieval uses background temperature and RO refractivity to compute humidity using Eq. (1). The influence of a T error on e (i.e., the relation between δT and δe) can be directly derived from Eq. (1) (Ware et al., 1996), under the assumption that N and p are constant:

$$\mathrm{d}N = \frac{\delta N}{\delta T}\delta T + \frac{\delta N}{\delta e}\delta e = 0 \longrightarrow \tag{2}$$

$$\delta e = \frac{1}{3.73 \times 10^5}(2NT - 77.6p)\delta T. \tag{3}$$

Ware et al. (1996) showed that e could be estimated to within 0.25 hPa in the lower troposphere if temperature were known to within 1 K. Vergados et al. (2014) depict the retrieval errors of specific humidity q due to temperature uncertainty for several latitude bands and pressure levels and show that humidity errors increase with increasing altitude and latitude, since humidity, and thus its contribution to atmospheric refractivity, decreases. In the tropics (relevant for this study), the q uncertainty for 1 K T uncertainty is less than ± 3 % below 700 hPa and increases to 18 % at 400 hPa (cutoff altitude in this study).

We use the RO variable "N_obs" (observed N before going through the 1D-Var) from the UCAR CDAAC wetPrfs. We chose T from the co-located GFS profiles as prescribed temperatures in the humidity retrieval for a greater independence between RO and ERA. For the four locations in this study, the maximum T difference between GFS and ERA occurs at Guam, with up to 2 K in the 800–500 hPa layer for the individual profiles. Comparisons of the UCAR direct retrieval using GFS T versus ERA T as background temperature shows specific-humidity differences of less than 3.5 % for seasonal and 200 hPa layer averages within the 800–300 hPa layer.

2.1.3 WEGC 1D-Var

The Wegener Center for Climate and Global Change (WEGC) developed a simplified version of a 1D-Var method. As a background, they use ECMWF 24 or 30 h forecast fields, which are spatially interpolated to the location of the RO (Schwärz et al., 2016). Combining the Smith–Weintraub equation and the hydrostatic equations for dry and moist air, they are solved for e and p with prescribed T, and for T and p with prescribed e. Iteration continues until the retrieved e and T converge within a set tolerance. Then the results are combined to get the optimally estimated T and e profiles. More information about the retrieval and error characteristics can be found in Ladstädter et al. (2015) and references within.

2.1.4 JPL direct

JPL's direct retrieval is similar to the UCAR direct but uses the ECMWF Tropical Ocean and Global Atmosphere (TOGA) T as a priori. Humidity is only derived below the level of tropospheric $T = 250$ K (Kursinski et al., 1997). JPL RO data were downloaded via the Atmospheric Grid Analysis and Profile Extraction tool[2].

2.2 ERA-Interim reanalyses

We use the ERA as a reference (or baseline) for our comparisons[3]. We do not consider the ERA as "truth", but we do consider the ERA to be the most accurate data set (Anthes and Rieckh, 2018) because it uses quality-checked observations with a 4D-Var data assimilation scheme and an accurate forecast model in a research mode to produce the variables of interest here (temperature and water vapor) on a $0.7° \times 0.7°$ grid. In 2007 ERA assimilated measurements from many different observing techniques, including RS observations, AIRS radiances, and RO bending angles (Dee et al., 2011). Thus, when using the word "bias" for a data set in a comparison, we refer to the bias difference with respect to ERA.

Apart from using ERA as a reference, we also created two baseline data sets from ERA for comparison to the observations. The first one is the climatology (hereafter CLIMO) for 2007, which is simply the ERA 2007 annual mean. The second one is the persistence (PERSIST) value of each variable from the value of the time series 24 h earlier. It represents a measure of the day-to-day variability in the ERA data set. These two simple data sets represent a baseline against which the value of observations can be compared. A minimum requirement for an observation type to be useful is that it must contribute additional information above those contributed by these baseline data sets; i.e., they must be more accurate than these data sets.

2.3 Radiosonde, AIRS, and GFS

RS data for Guam (13.5° N, 144.8° E) and three Japanese stations (Ishigakijima: 24.2° N, 124.5° E; Minamidaitojima:

[1] http://cdaac-www.cosmic.ucar.edu/cdaac/ (last access: 17 September 2017)

[2] https://genesis.jpl.nasa.gov/agape/ (last access: 18 September 2017)

[3] https://rda.ucar.edu/datasets/ds627.0/ (last access: 26 June 2017)

25.6° N, 131.5° E; Naze: 28.4° N, 129.4° E) (Fig. S1, in the Supplement) were downloaded from the National Oceanic and Atmospheric Administration[4]. The RS are given on six standard pressure levels between 1000 and 400 hPa, plus additional levels if there is higher-resolution vertical structure. The RS at the four stations are generally launched twice daily during the hour before midnight and noon (UTC). The four stations use the following sensors: Guam: Sippican VIZ-B2; Ishigakijima: Meisei; Minamidaitojima: Vaisala RS92; and Naze: Meisei[5]. The Sippican VIZ-B2 humidity sensor has a nighttime wet bias (Wang and Zhang, 2008; Ho et al., 2010) and performs poorly in dry conditions (Holger Vömel, personal communication, 2017). Ho et al. (2010) found no obvious bias for the Meisei sensor. The Vaisala RS92 sensor is known for its dry bias (Vömel et al., 2007) of $\sim 9\,\%$ at surface, and up to 50 % at 15 km altitude, and several correction schemes have been developed to address this (Miloshevich et al., 2006; Vömel et al., 2007).

AIRS is a nadir-looking instrument aboard the National Aeronautics and Space Administration (NASA) Aqua satellite, which was launched in May 2002. AIRS provides atmospheric variables on 28 standard pressure levels between 1100 and 0.1 hPa (8 levels between 1100 and 400 hPa)[6]. The vertical resolution is ~ 1 km for temperature and ~ 2 km for humidity[7]. The horizontal resolution[8] is 50 km. We use the AIRS Version 6 Level 2 (AIRS2RET) data with a quality flag of "BEST" or "GOOD".

The AIRS retrieval is a cloud-clearing retrieval. Susskind et al. (2003) describe the cloud-clearing process that yields the "clear" radiances from which all parameters except clouds are retrieved (Kahn et al., 2014). The humidity retrieval of Version 6 is basically the same as in Version 5 but still yields improved humidity results due to the improved first guess provided by the Neural-Net start-up system, improvements in the determination of other atmospheric variables, and improvements in cloud-cleared radiances (Susskind et al., 2014).

RO co-located profiles for GFS are added in the comparison to show results from an analysis that is different from ERA. GFS profiles are given on a 25 or 50 hPa grid (depending on altitude) and are linearly interpolated to the time and location of the UCAR 1D-Var profiles.

[4]https://www.ncdc.noaa.gov/data-access/weather-balloon/integrated-global-radiosonde-archive (last access: 7 June 2017)

[5]https://www1.ncdc.noaa.gov/pub/data/igra/history/igra2-metadata.txt (last access: 2 June 1017)

[6]ftp://airsl2.gesdisc.eosdis.nasa.gov/ftp/data/s4pa/Aqua_AIRS_Level2/AIRS2RET.006/ (last access: 13 December 2017)

[7]http://airs.jpl.nasa.gov/data/physical_retrievals (last access: 13 December 2017)

[8]http://disc.gsfc.nasa.gov/uui/datasets/AIRS2RET_V006/summary (last access: 13 December 2017)

2.4 Design of the comparisons

Since we are investigating humidity differences of various observing systems, we chose regions where humidity conditions are highly variable in both space and time with extremely high and low values during the year. We use the tropical location Guam, which frequently experiences dry air intrusions from the subtropical upper troposphere–lower stratosphere (UTLS) region from December to March (Rieckh et al., 2017). This leads to sharp vertical humidity gradients (relative humidity changes from less than 10 to about 80 % within a small vertical layer), conditions that are favorable for RO super-refraction (Garratt, 1992). Super-refraction, in turn, will lead to a negative bias in the RO-observed N and q. See Fig. S3 for the ERA 2007 time series of specific humidity, relative humidity, temperature, and refractivity at Guam.

The other RS locations are subtropical stations around Japan, which experience a large seasonal variability as well as extreme conditions associated with occasional typhoons. See Fig. S4 for the ERA 2007 time series of specific humidity, relative humidity, temperature, and refractivity at Ishigakijima.

To increase the number of co-located profiles, we picked the year 2007 for our analysis, when all COSMIC satellites were operating reliably. Since the measurement techniques for RO, RS, and AIRS are different, we use different co-location criteria to get a maximum number of high-quality co-locations. For the ERA reference grid points matched to the RS stations, the distance between any of the RS stations and the respective ERA grid point is between 15 and 35 km, and the time difference less than an hour from the 00:00 and 12:00 UTC ERA data. RO observations are co-located within 3 h and 300 km, and a co-location correction as described by Gilpin et al. (2018) is applied:

$$\begin{aligned}\Delta X_{\mathrm{SC}} &= (X_{\mathrm{RO}} - X_{\mathrm{RS}})_{\mathrm{SC}} \\ &= (X_{\mathrm{RO}} - X_{\mathrm{RS}}) - \left(X_{\mathrm{ERA}}^{\mathrm{RO\,loc}} - X_{\mathrm{ERA}}^{\mathrm{RS\,loc}}\right), \end{aligned} \quad (4)$$

where ΔX_{SC} denotes the spatially corrected difference of X, X is a variable measured by RO and RS, and the co-location correction is the difference in the ERA values of X at the RS and RO locations. Gilpin et al. (2018) show that double-differencing correction significantly reduces the mean and root mean square (rms) differences of the RO and RS observations. Since our reference location is an ERA grid point, we replace RS with ERA in Eq. (4), which simplifies to $\Delta X_{\mathrm{SC}} = X_{\mathrm{RO}} - X_{\mathrm{ERA}}^{\mathrm{RO\,location}}$.

AIRS profiles are extracted within 30 km from the ERA reference point; the maximum time difference is 3 h. Figure S2 depicts the co-location process for all data sets and one time.

Due to the restrictions as explained above, the resulting profile pairs (and number of profile pairs) between ERA and any of the data sets are different. Furthermore, the four RO

retrievals have different quality control schemes, which especially lowers the number of available JPL profiles. The penetration depths also vary for the RO data sets and retrievals; for example, the UCAR 1D-Var data are available on lower levels than UCAR direct because the bottom height is given as $z_{OB} - e_{CL}$, where z_{OB} is the bottom height of observation, and e_{CL} is the background error correlation length (which is 500 m in the UCAR 1D-Var).

All data sets are interpolated to a common 25 hPa grid. We chose this grid as a compromise between the effective resolutions of all data sets used. The effective resolution of RO is estimated to be higher than 100 m in the troposphere (Gorbunov et al., 2004). The RS has observations on additional levels (significant levels) if there are significant changes in the vertical profile. ERA and GFS are provided on a pressure grid with 25 or 50 hPa increments. AIRS is sampled on a sparser vertical grid and thus does not resolve small-scale features in the vertical. But any biases over deep layers will be evident, and if interpolation leads to biases in certain pressure layers, a pattern will be clearly visible in the individual profiles.

The horizontal scale (footprint) of each data set varies. The horizontal resolutions of the ERA and GFS models (grid size) are approximately $80\,\text{km} \times 80\,\text{km}$ and $28\,\text{km} \times 28\,\text{km}$, respectively. The AIRS footprint is approximately $50\,\text{km} \times 50\,\text{km}$. The RO observations have a horizontal length scale along the ray path of order 200 km (Anthes, 2011). Finally, the RS is essentially a point measurement. These differences can lead to representativeness errors, or differences, because the finer-scale data sets can resolve horizontal variability on smaller scales than the lower resolution of the RO (200 km). Some of this representativeness difference is reduced by the vertical averaging to 25 hPa layers. The remaining differences tend to cancel in the mean because the ERA, RS, and RO observations are located randomly with respect to each other, and the smaller-scale structures that they resolve vary randomly within the model grid volumes. However, these differences in representative scale will contribute to the rms differences from the ERA data set.

Profile pairs of ERA and each data set are extracted, and the computed differences are normalized by the ERA 2007 mean value (CLIMO) at each level: normalized difference $(\text{ND}) = 100 \cdot (\text{dataset} - \text{ERA})/\text{CLIMO}$ (expressed as %). To make it easier to transfer results from normalized to actual differences, the constant value CLIMO is used to normalize all data sets. The values for CLIMO are shown in Fig. 1, and the exact values are provided in the Supplement in Table S1 for an easy reproduction of the original values.

3 Results

3.1 Overview: general agreement and correlation between the data sets

Figure 2 shows values of q for UCAR direct, UCAR 1D-Var, WEGC 1D-Var, JPL direct, RS, AIRS, and GFS (left to right) versus ERA from high- to low-pressure layers (top to bottom), depicting the correlation between the observational data sets and ERA at Guam (log–log correlation coefficients in the title of each panel). Additionally, the mean and standard deviation values of the differences for each pressure layer are depicted in each panel (since values are not normalized, values from the lower levels will have a larger influence on the result).

There is good agreement and high correlation for all data sets in the 1000–400 hPa layer (Fig. 2, bottom panels). The RS shows the largest difference (~ 1 order of magnitude) for generally low humidity values. Some larger differences can also be seen for the UCAR direct, UCAR 1D-Var, JPL direct, and GFS when these data sets are much drier than ERA (primarily happening in the DJF season). The large differences occur generally for q values less than $1\,\text{g}\,\text{kg}^{-1}$, with many lower than $0.1\,\text{g}\,\text{kg}^{-1}$, which indicates dry higher altitudes (i.e., above 500 hPa). RO refractivity becomes less sensitive to water vapor at these higher altitudes, and the RO retrievals of water vapor, whether direct or 1D-Var, are less reliable at these levels (Kursinski et al., 1995). The UCAR 1D-Var can also have difficulties retrieving very low humidity values (which is the case in the DJF season at Guam). If the a priori temperature is too low, it can happen that the UCAR 1D-Var humidity values are set to zero, which would lead to a dry RO bias overall for low values of specific humidity. The data sets look similar in the 400–300 hPa layer, and a dry bias for the RS becomes visible. In the 300–200 hPa layer, the UCAR direct spread becomes very large (indicating limited usefulness for RO direct retrievals at this level), while the UCAR 1D-Var and WEGC 1D-VAR agree very well with ERA, since they are using ERA and ECMWF short-range forecast profiles as background in the retrieval, respectively. JPL direct humidity data are not available at these pressure levels. Both RS and AIRS show a dry bias. Finally, in the 200–100 hPa layer the UCAR direct data are useless, the UCAR 1D-Var is practically identical to ERA (simply recovering ERA a priori values), and the RS and AIRS data both have a strong dry bias. The GFS agrees fairly well with ERA in the upper layers and has no obvious bias.

3.2 Time series at Guam

Figure 3a shows the time–height cross section of RH over 2007 from 1000 to 400 hPa at Guam. Overall, the conditions at Guam are moist ($\text{RH} > 80\,\%$ and $q \sim 17\,\text{g}\,\text{kg}^{-1}$) year-round in the boundary layer and in the mid-troposphere from July to November, and dry in the mid-troposphere during

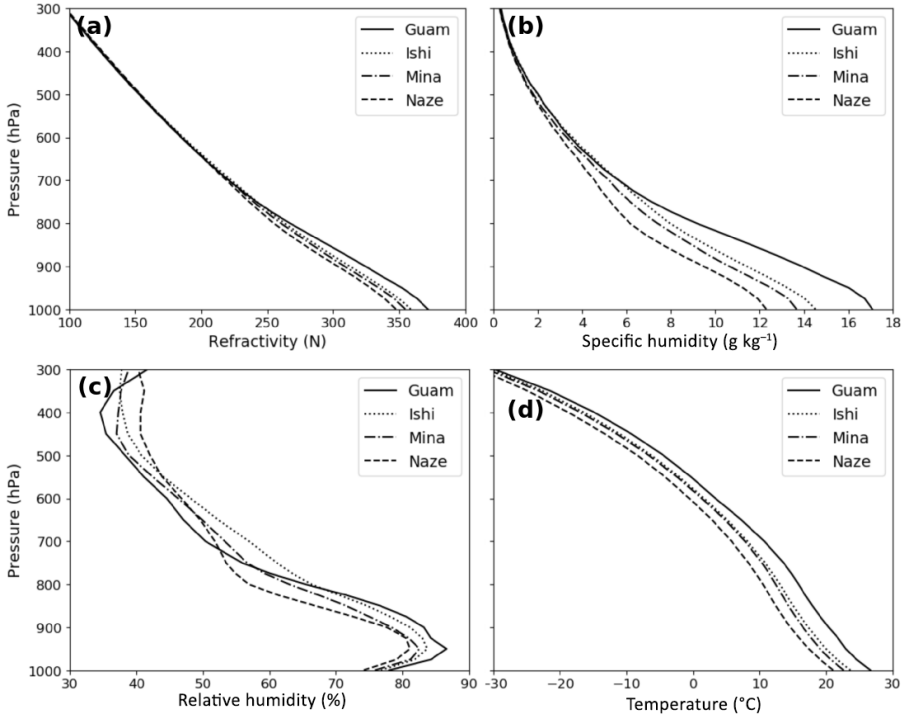

Figure 1. ERA annual average profiles on the 25 hPa grid for **(a)** refractivity, **(b)** specific humidity, **(c)** relative humidity, and **(d)** temperature at all four locations.

the rest of the year. The changing humidity pattern above 800 hPa results from the alternation of the high-humidity tropical conditions and dry air intrusions from the subtropical UTLS in December to June (Randel et al., 2016). These dry intrusions (relative humidity as low as a few percent) are very stable and suppress convection. The sharp humidity gradient between the very dry lower mid-troposphere and the moist boundary layer around 800 hPa often leads to conditions of super-refraction, which results in a negative bias of N and thus q in the RO profiles (Xie et al., 2010).

The ND of specific humidity q between the PERSIST data set and ERA (which represents the day-to-day variability of ERA) shows that q has almost no day-to-day variability in the 1000–800 hPa layer during the entire year and in the 800–600 hPa layer in August and September (Fig. 3b). Above, day-to-day variability is significant. Exceptions occur in the 600–400 hPa layer during December through May, when persistent dry air intrusions occur. This shows just how stable and persistent these layers can be, suppressing major changes in humidity for up to 20 days in a row.

The ND of q between GFS and ERA (Fig. 3c) shows that the differences between the two model values of q are much smaller than the differences between PERSIST and ERA, as might be expected. GFS is up to 50 % moister than ERA in the 800–600 hPa layer in the dry season, and in the 800–550 hPa layer in the wet season. This is essentially the layer of strong humidity variability above the bottom layer of constant (about 80 %) relative humidity. This behavior may be due to GFS difficulties in capturing the sharp transition between dry and wet conditions on the bottom of dry layers in December to June. This is supported by individual profiles (e.g., Randel et al., 2016, Fig. 4), as well as our comparison of ERA with RS (Fig. 4a), which supports the ERA in this respect.

The ND show a small wet bias of the RS relative to ERA in the lower troposphere and large wet and dry biases in the middle and upper troposphere throughout the year (Fig. 4a). The large biases are likely caused by RS sensor malfunctions (Holger Vömel, personal communication, 2017), which can start as low as at 800 hPa. At some point during the ascent, the sensor gets stuck and keeps reporting the same humidity value, which manifests itself as a dry or wet bias compared to ERA, depending on if tropospheric conditions are drier (December through May) or wetter (June through November) than the incorrect reported value.

AIRS shows an overall dry bias compared to ERA throughout the entire troposphere in all seasons (Fig. 4b). The dry bias appears to be less during the dry-air-intrusion events in the 600–400 hPa layer in the dry season (December to June). This indicates that AIRS is less biased if the overall atmospheric conditions are dry. The AIRS dry bias agrees well with the findings of Wong et al. (2015), who studied the uncertainties of AIRS Level 2 Version 6 q and T depending on cloud types. They found reduced dry biases in the middle

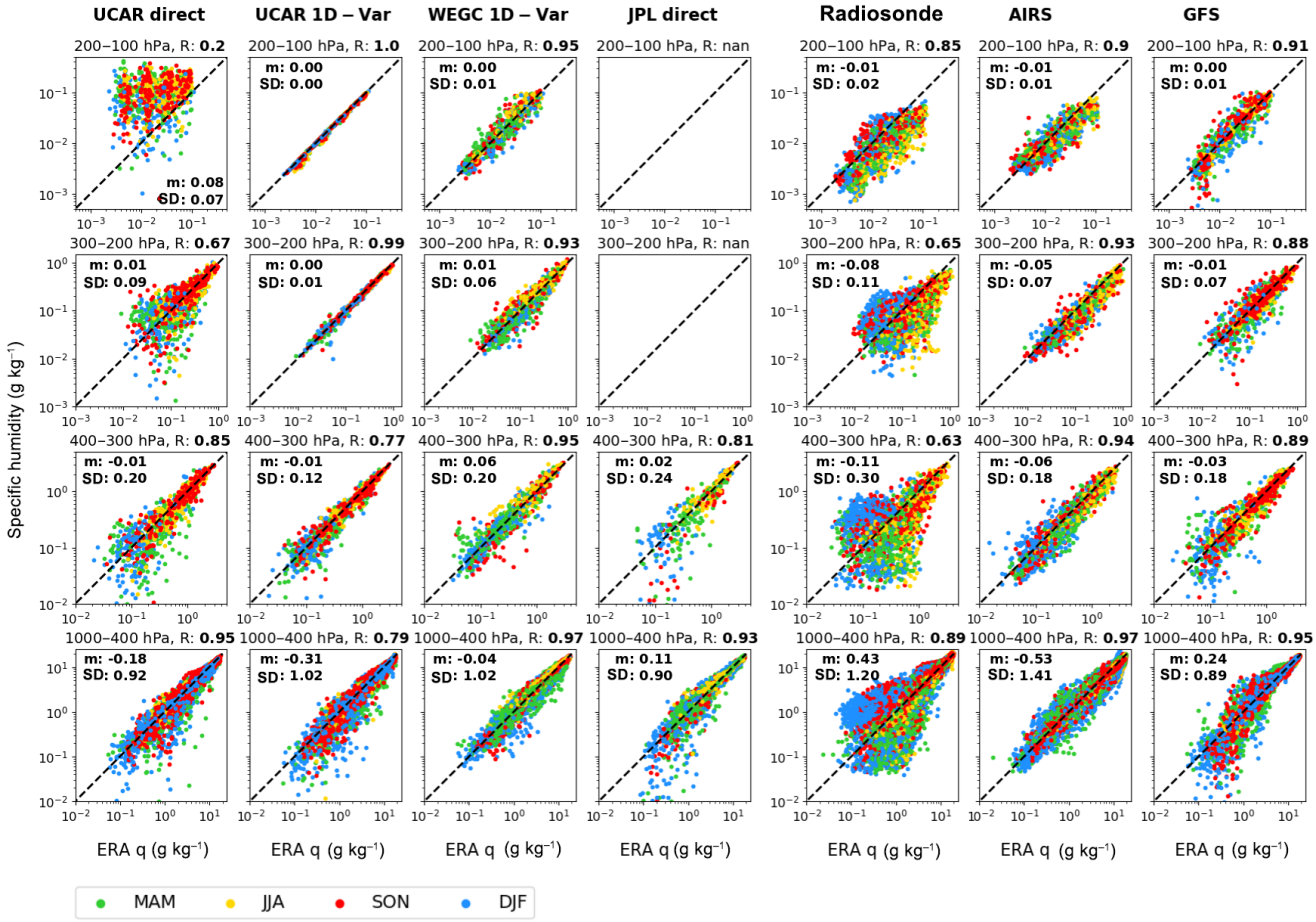

Figure 2. Guam: scatterplots of q for seven data sets versus ERA for four pressure layers. Left to right: UCAR direct, UCAR 1D-Var, WEGC 1D-Var, JPL direct, RS, and AIRS. Correlation coefficients as well as mean and standard deviation of the differences are given for each panel. Note that both axes are on a logarithmic scale and that axis limits vary for different pressure layers.

troposphere under thin clouds, but large dry biases (> 30 %) in the lower troposphere with low thick clouds, and dry biases throughout the troposphere in the presence of high thick clouds.

The normalized differences of the four RO retrievals to ERA show similar patterns in the 1000–800 hPa layer but larger differences in the mid- and upper troposphere (Fig. 5). The UCAR direct data develop a wet bias above 600 hPa in the wet season and alternate between dry and wet during the other seasons. The UCAR 1D-Var data show an overall dry bias throughout the troposphere with a few exceptions. Both JPL and WEGC data develop a strong wet bias above 600 hPa in the wet season. Common features of all four RO retrievals include the very small differences to ERA in the wet season in the 1000–800 hPa layer and a dry bias and/or frequent reduced penetration depth (loss of signal) in the dry season. The latter is a signature of super-refraction, which itself is caused by strong humidity gradients, usually between the planetary boundary layer and the free troposphere.

Figure 5 also shows that all RO data sets are biased dry with respect to ERA in December through February in the 800–600 hPa layer, which is clearly above the layer of strong humidity gradients (compare to Fig. 3a). We found similar behavior in previous work. In Rieckh et al. (2017), Fig. 2, lower right panel, ERA data are given on the 775, 750, 700, and 650 hPa pressure levels (about 2.3, 2.6, 3.1, and 3.8 km, respectively). The 775 and 650 hPa levels agree well with the aircraft and RO measurements; however, the two levels in between smear the sharp profile, and the ERA shows humidity values 1.5 to 2.5 g kg^{-1} (20 to 35 %) larger than the observations. Thus we conclude that the bias in Fig. 5 may not be a dry bias in RO but could be a wet bias in ERA in the layer just above the strong humidity transition from wet (PBL) to dry (above). The assumed errors for assimilating RO in ERA are large in the lower troposphere, and all assimilated nadir-viewing instruments only provide vertical resolutions of about 2 to 3 km. Unless a nearby approved RS contributes information locally, ERA does not have any vertically well-

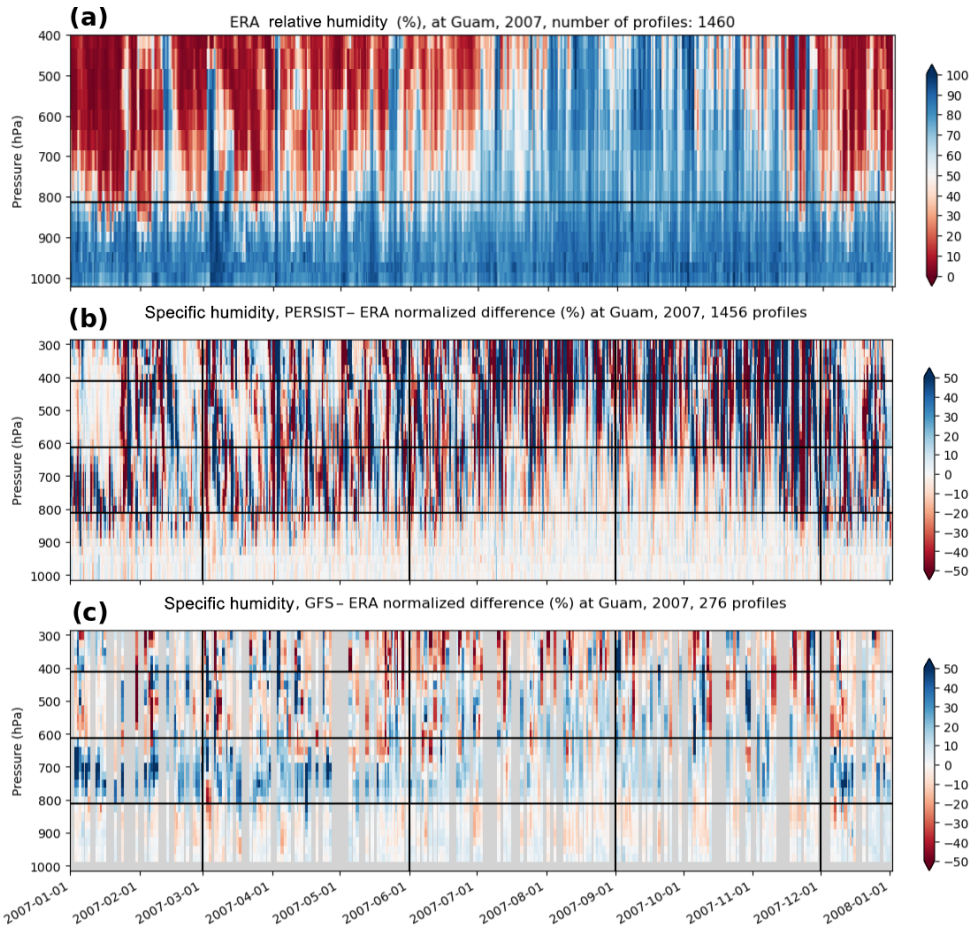

Figure 3. 2007 time series at Guam: **(a)** ERA relative humidity (%) with blue representing moist air and red representing dry air; **(b)** normalized difference of q (%) between PERSIST and ERA; **(c)** normalized difference of q (%) between GFS and ERA. The bottom panel shows that there are significant (±50%) differences in the two model data sets. The color bar on the right indicates relative humidity (%) in **(a)** and specific-humidity normalized differences (%) in **(b)** and **(c)**.

resolved humidity data that will cause the ERA analysis to develop such sharp humidity gradients.

The 2007 time series of the q normalized difference for all data sets are depicted for a Japanese station (Minamidaitojima) in Figs. S5 and S6.

The 2007 time series of the refractivity N normalized difference for all data sets are depicted for Guam in Figs. S7 and S8.

3.3 Mean and rms differences from ERA at Guam

We compute the mean and root mean square (rms) of the normalized differences at Guam to get a statistical overview of the differences from the ERA for all data sets for three pressure layers (1000 to 400 hPa in 200 hPa layers) and four seasons (Fig. 6).

Some general aspects of the different data sets seen in the individual time series are clearly visible in the mean (Fig. 6, top), such as the large negative (dry) difference of RO compared to ERA (green and blue bars) in DJF for the 1000–600 hPa layer. In the 1000–800 hPa layer, a dry bias for RO exists throughout the year. The dry bias is largest in DJF, but it is smaller than and comparable in magnitude to the biases of the RS and AIRS in MAM, JJA, and SON. RO retrievals show the greatest differences from each other in the 600–400 hPa layer year-round and in the 800–600 hPa layer in the wet season. AIRS shows an overall dry bias at all pressure layers and seasons. As expected, PERSIST has essentially no bias at any pressure layer or season. Because of the large seasonal variation in water vapor, CLIMO has large seasonal positive and negative biases above 800 hPa that are much larger than the biases of any other data set. GFS shows significant differences from ERA, especially in the dry season (DJF and MAM) in the 800–600 hPa layer.

Since the mean of the paired normalized differences is no indicator of their variability, we also show the rms (Fig. 6, bottom). The magnitude of the rms is a measure of the accuracy and scatter of the data compared to the reference.

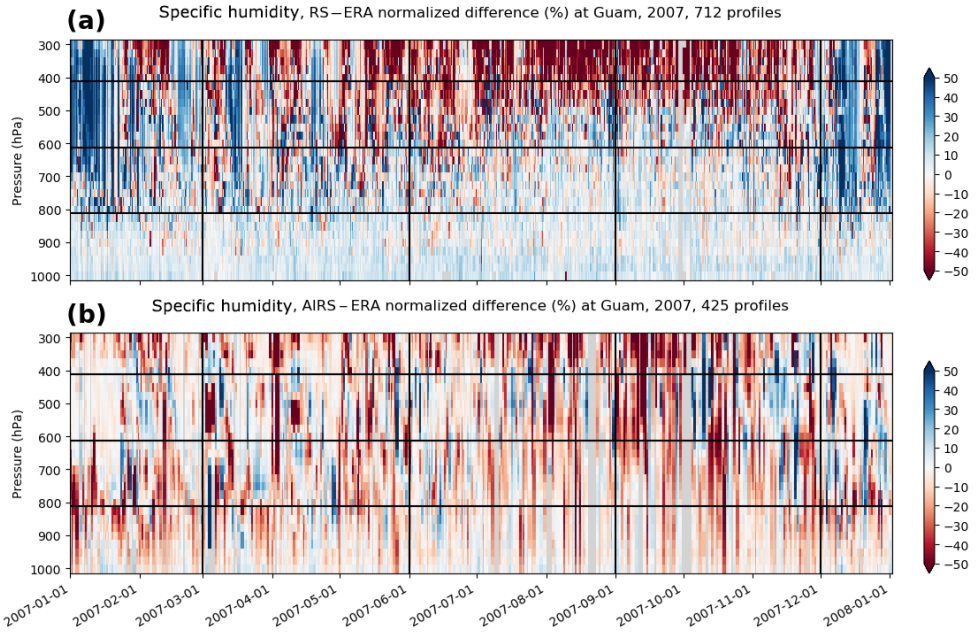

Figure 4. 2007 time series of the q normalized difference between **(a)** RS and ERA, and between **(b)** AIRS and ERA at Guam. The color bar on the right indicates specific-humidity normalized differences (%).

All data sets have a rms comparable to (below 800 hPa) or considerably smaller than (above 800 hPa) both CLIMO and PERSIST in all seasons (Fig. 6, bottom). The former is expected, considering how little humidity changes throughout the year in the 1000–800 hPa layer. The latter indicates the value (over persistence and climatology) of all observation techniques above 800 hPa. As for the individual data sets, we see that the RO rms for all retrievals is comparable to or lower than RS and AIRS rms for all seasons and pressure layers. This increases our confidence regarding the value of RO mid- and lower-tropospheric humidity data.

3.4 Statistics at the subtropical Minamidaitojima

At Minamidaitojima all data sets have a smaller bias compared to ERA (Fig. 7, top) than at Guam. The strong RO humidity bias in the dry-season lower troposphere (as seen at Guam) is not present, and biases of all observational data sets (with the exception of AIRS) are less than 5 % in the 800–600 hPa layer. Biases are larger in the 600–400 hPa layer, especially for the RS. The rms values at Minamidaitojima (Fig. 7, bottom) show a similar pattern to the one at Guam, with the RO and GFS rms differences being smaller than the RS and AIRS differences. The statistics of the other two Japanese stations (Ishigakijima and Naze) are similar (not shown).

4 Differences from ERA in dry versus wet atmospheric conditions

In Sect. 3 we saw how the general atmospheric humidity conditions (wet versus dry) can have an influence on the biases in the data sets with respect to ERA, especially for RO (superrefraction with strong vertical humidity gradients) and AIRS (smaller bias in dry conditions). In this section, we investigate the different error characteristics for dry and wet conditions in more detail at both the tropical and subtropical locations. We created a "dry" and "wet" data set. For every profile pair, we computed the average relative humidity (RH) of the ERA (background) profile for the 800–400 hPa layer ($\overline{\mathrm{RH}}_{800-400}$). This layer was chosen according to the humidity distribution throughout the year (see Fig. 3, top). If $\overline{\mathrm{RH}}_{800-400} \leq 30\,\%$, the entire profile is added to the dry data set. If $\overline{\mathrm{RH}}_{800-400} \geq 70\,\%$, the entire profile is added to the wet data set. Then the mean and rms are computed for both these data sets separately. These statistical values are depicted for the 1000–800 hPa layer and the 800–400 hPa layer (Fig. 8).

The mean of the normalized differences shows different patterns for the dry and wet data sets at both Guam and Minamidaitojima. At Guam, we see a dry bias of 6 to 14 % in the 1000–800 hPa layer for all RO retrievals for the dry data set (Fig. 8, left). We assume that the dry air intrusions and sharp humidity transitions above the PBL with associated superrefraction conditions are primarily responsible for the negative N and thus negative q bias at Guam. The RO biases in the 800–400 hPa layer vary around zero (−4 to 2 %). For the

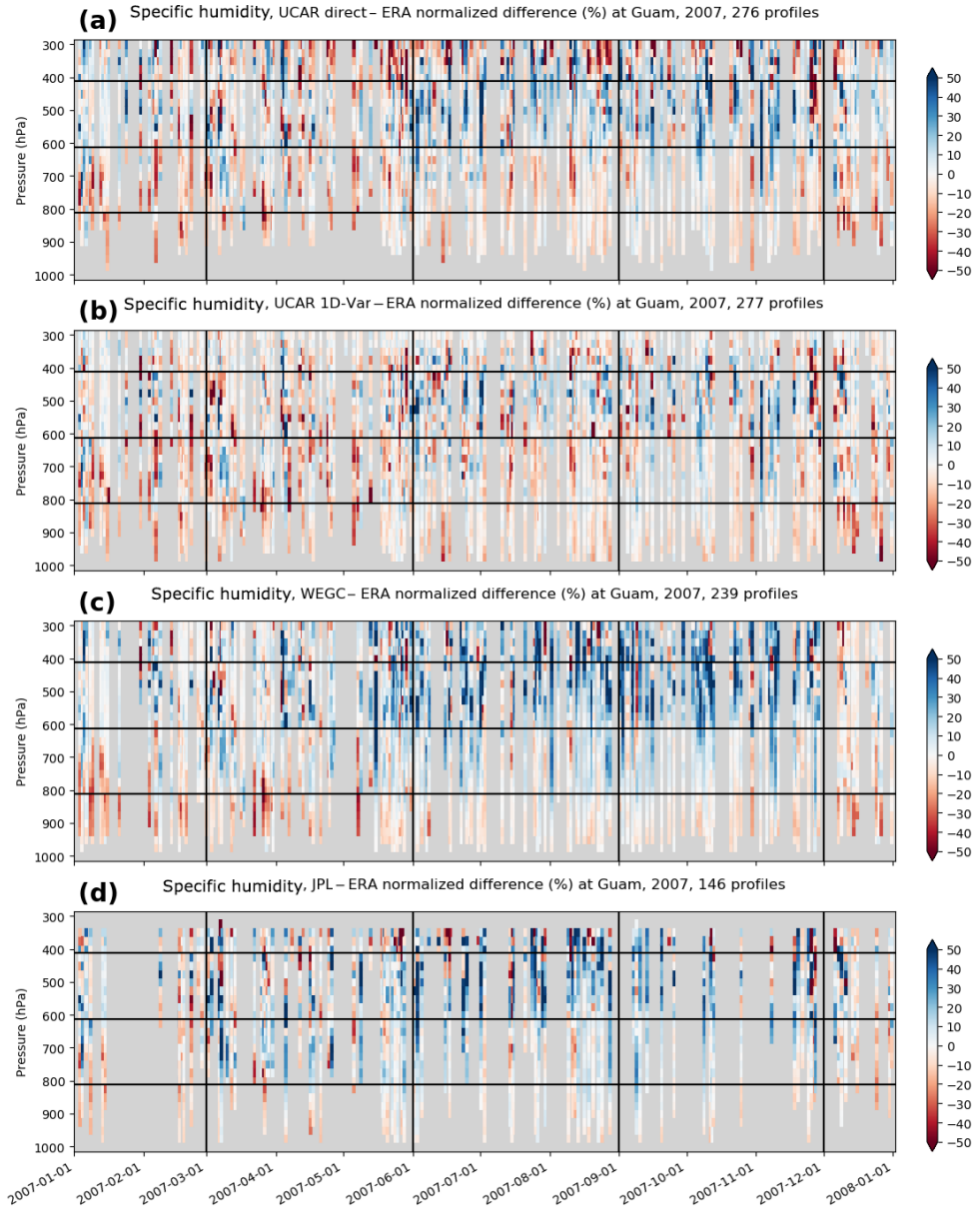

Figure 5. The 2007 time series of the q normalized difference at Guam for the **(a)** UCAR direct, **(b)** UCAR 1D-Var, **(c)** WEGC 1D-Var, and **(d)** JPL direct retrieval. The color bar on the right indicates specific-humidity normalized differences (%).

wet data set, the mean RO differences from ERA vary significantly in the 800–400 hPa layer from 0 to 16 %, while the bias in the 1000–800 hPa layer is between 0 and −5 % for the RO retrievals. At Minamidaitojima, the RO data sets show smaller and similar biases for both pressure layers (Fig. 8, right). The dry RO data set has no bias in the 800–400 hPa layer and very small biases (2 to 5 %) in the 1000–800 hPa layer. The bias with respect to ERA of the wet RO data set ranges from −4 to 4 % in the 800–400 hPa layer and from −4 to 2 % in the 1000–800 hPa layer. Overall, we conclude that there are no major differences in the RO error characteristics between the dry and wet data sets or between the two pressure layers at Minamidaitojima, in contrast to Guam, where background humidity conditions clearly matter for the different error characteristics.

AIRS clearly shows a strong dry bias for both pressure layers for wet background conditions. The bias is stronger at Minamidaitojima, reaching more than −30 % in the 800–400 hPa layer and −20 % in the 1000–800 hPa layer. For dry conditions, the AIRS bias ranges from −8 to 2 % for all locations and pressure layers. This agrees well with the small bias seen in the regions of dry air intrusions (December to June) in the profile time series (Fig. 4, bottom).

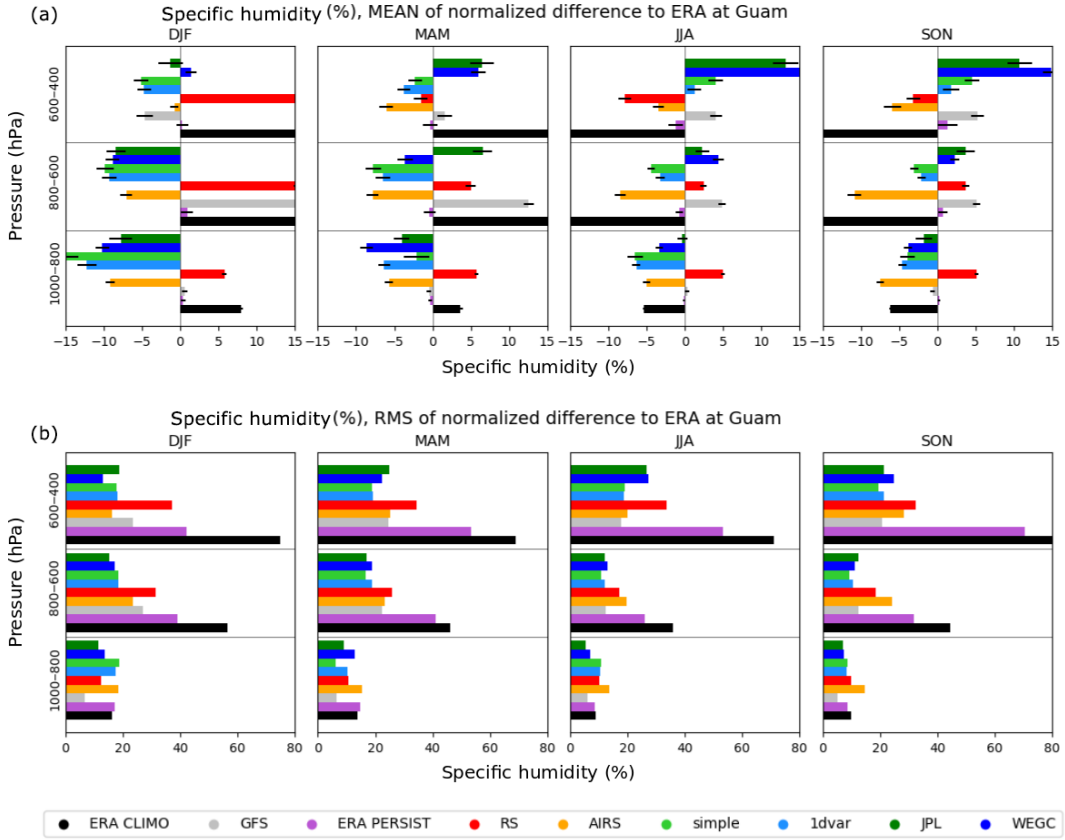

Figure 6. Guam: The mean **(a)** and rms **(b)** of the q normalized difference for all data sets, three pressure layers, and four seasons. Data sets from top to bottom (per pressure layer): JPL direct, WEGC 1D-Var, UCAR direct, UCAR 1D-Var, RS, AIRS, GFS, PERSIST, CLIMO.

Finally, the RS shows a small wet bias in the 1000–800 hPa layer for both the dry and wet data sets and both locations. In the 800–400 hPa layer, the dry data set shows a large wet bias, which is likely due to the Sippican VIZ-B2 sensor's poor performance in dry conditions (see Sect. 2.3). At Minamidaitojima, both the dry and wet data sets show a dry bias in the 800–400 hPa layer, as described in Vömel et al. (2007) for the Vaisala RS92 sensor for higher altitudes due to a radiation bias.

5 Variability during typhoon passages

We used the subtropical RS station Ishigakijima to investigate how the different data sets perform during the extreme conditions of typhoon passages. In 2007, six typhoons passed Ishigakijima within 350 km (the tracks and other details of the typhoons can be found online[9]):

- typhoon #4, 6–16 July, date of closest approach (320 km): 12 July, as typhoon category 4;
- typhoon #7, 4–10 August, date of closest approach (260 km): 7 August, as typhoon category1;
- super typhoon #9, 11–19 August, date of closest approach (300 km): 17 August, as typhoon category 4;
- typhoon #12, 11–17 September, date of closest approach (330 km): 14 September, as typhoon category 4;
- super typhoon #13, 14–20 September, date of closest approach (40 km): 18 September, as typhoon category 3;
- super typhoon #17, 1–8 October, date of closest approach (110 km): 6 October, as typhoon category 4.

The time series of differences to ERA q for Ishigakijima do not show a specific bias during typhoon passages, which indicates that all data sets as well as ERA report a signal similar in magnitude during the typhoon passages.

We computed the ERA average over the July–October time range ($\mathrm{CLIMO_{JulOct}}$) to create a typhoon season climatology. We then compared all data sets to $\mathrm{CLIMO_{JulOct}}$ to see how q and T deviate from the summer average during the passage of a typhoon. All data sets show a rapid increase in

[9] http://weather.unisys.com/hurricane/w_pacific/2007/ (last access: 10 December 2017)

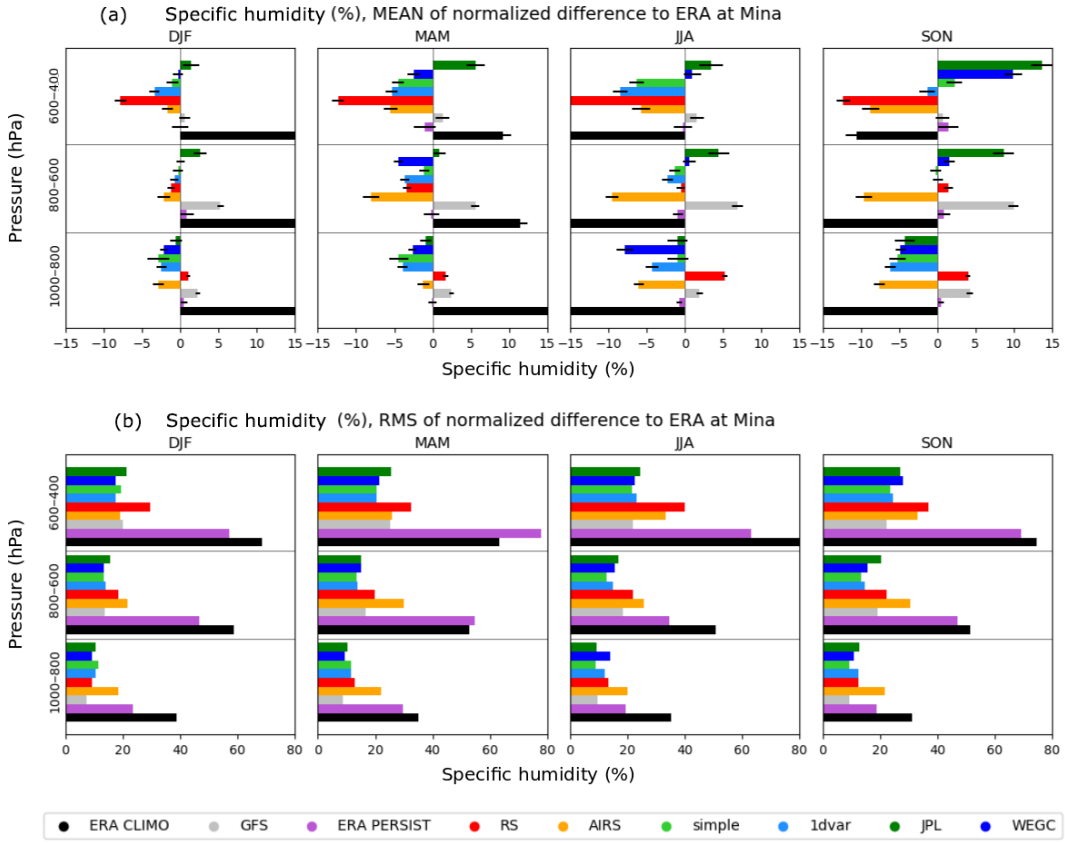

Figure 7. Mina: Mean **(a)** and rms **(b)** of the q normalized difference for all data sets, three pressure layers, and four seasons

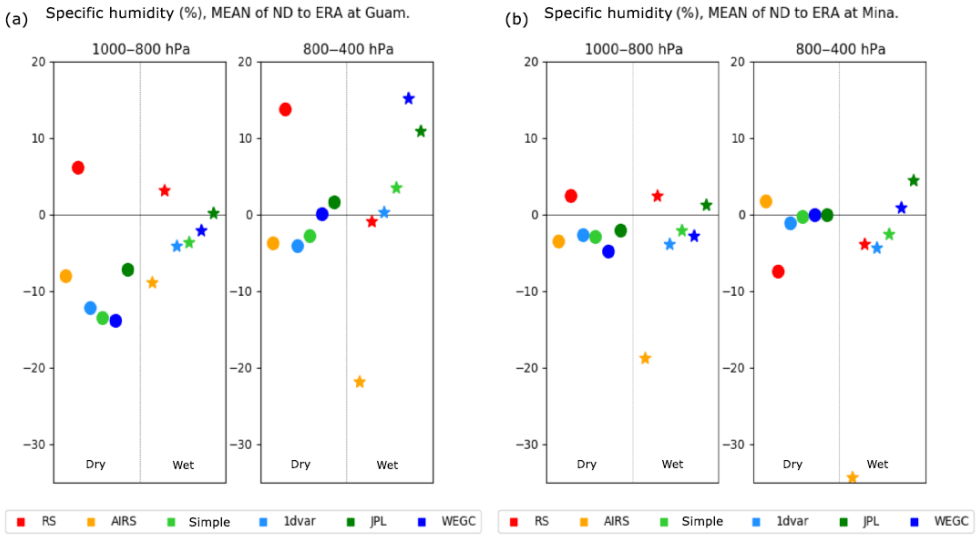

Figure 8. Mean differences for dry versus wet atmospheric conditions based on $\overline{\mathrm{RH}}_{800-400}$ at Guam **(a)** and Minamidaitojima **(b)**. The different colors represent the different data sets. Circles and stars represent the data sets for dry and wet conditions in the mid-troposphere, respectively.

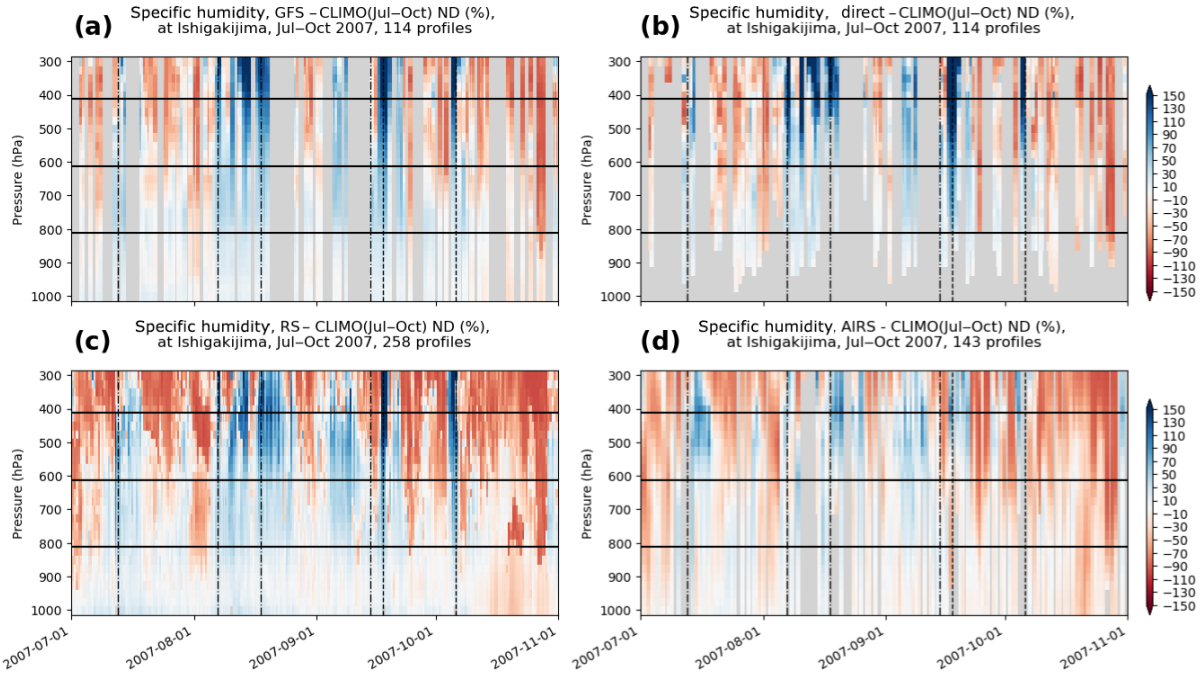

Figure 9. The q difference from $\mathrm{CLIMO_{JulOct}}$ for **(a)** GFS, **(b)** UCAR direct, **(c)** RS, and **(d)** AIRS shows increased humidity during typhoon passages near Ishigakijima. Typhoon passages are marked by vertical lines (dashed: closer than 110 km; dash-dotted: closer than 330 km).

humidity (Fig. 9) and higher temperature values (not shown) as the typhoons approach and pass close to Ishigakijima. The signal is strongest above 600 hPa, where deep convection associated with the typhoons transports large amounts of water vapor and releases latent heat in the middle and upper troposphere (Emanuel, 1991).

GFS, RS, and all RO retrievals show similar results. The AIRS moist deviation during a passage is much weaker than for any other data set, likely because of all the cloud cover associated with the typhoons, which limits the AIRS retrievals.

All data sets show increased temperature during the typhoon event (not shown), especially in the upper troposphere. The UCAR and WEGC 1D-Var show a similar T structure. The signal also agrees well with the GFS T signal. Neither of the direct retrievals (UCAR and JPL) provides physical temperature information on the troposphere.

The signals in q, T, and N during a typhoon passage are similar for Minamidaitojima and Naze (not shown), but fewer typhoons passed in close proximity to these two stations.

6 Structural uncertainty of RO

Since we have data from several RO retrievals available, we have the opportunity to compute the structural uncertainty of RO humidity for our data set, following the methods of Steiner et al. (2013) and Ho et al. (2009, 2012). The structural uncertainty is computed to get an estimate of the variability among the various RO retrievals.

First we create sub-data-sets, which are limited to the profiles and pressure levels that are available for all four RO humidity retrievals. The sub-data-set for Guam consists of 141 profiles, and the sub-data-set for the combined Japanese stations (since atmospheric conditions are very similar among them) consists of 543 profiles. For each retrieval, the normalized deviation for N and q from the inter-center mean is computed (per pressure level):

$$\Delta X = \frac{1}{k}\sum_{k}\left(X_k - \overline{X}_k^{\text{inter-center}}\right)\frac{100}{\overline{X}_{\text{annual}}^{\text{ERA}}}, \tag{5}$$

where k indicates the profile number, $\overline{X}_k^{\text{inter-center}}$ is the inter-center average for the kth profile ($1/4(X_k^{\text{UCAR direct}} + X_k^{\text{UCAR 1D-Var}} + X_k^{\text{JPL direct}} + X_k^{\text{WEGC 1D-Var}})$, and ΔX is the deviation (of q or N) of one particular RO retrieval from the inter-center average.

Figure 10 shows the mean deviations of the four RO retrievals from the inter-center mean for Guam (left) and all three Japanese stations combined (right) for N (top) and q (bottom). Cutoff pressure is 350 hPa since JPL does not provide humidity data above that level. For N (Fig. 10a, b), the absolute value of the mean deviation from the inter-center mean is largest between 900 and 700 hPa for all data sets (maximum of 0.7 %) and decreases to about 0.1 % at 350 hPa (about 8 km) at both locations. The latter result agrees well

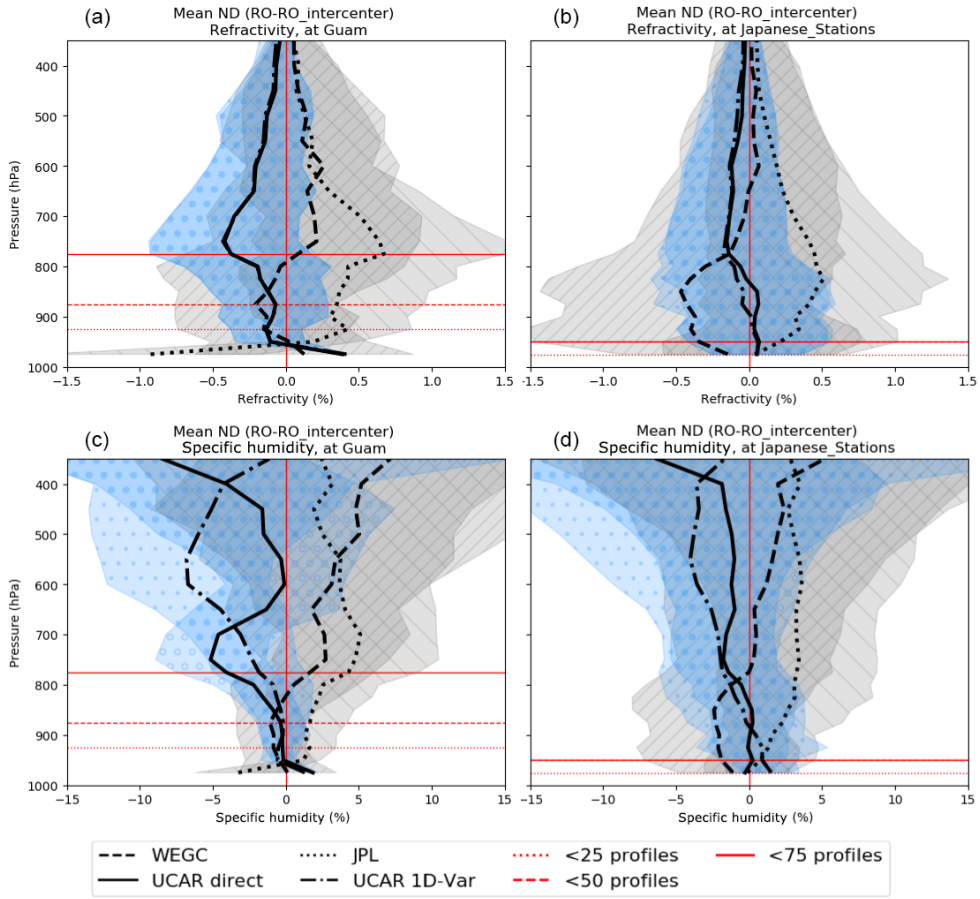

Figure 10. Deviations for four RO retrievals from the inter-center mean for refractivity **(a, b)** and specific humidity **(c, d)** at Guam **(a, c)** and the Japanese stations **(b, d)**. The mean (and standard deviation) of each data set is shown by line style (and as shaded and hatched area): UCAR direct: black solid (and o o o, blue); UCAR 1D-Var: black dash-dotted (and · · ·, blue); WEGC 1D-Var: black dashed (and ///, gray); JPL direct: black dotted (and \ \ \, gray). Red horizontal lines indicate the number of profile pairs at that pressure level.

with the estimate of Ho et al. (2009), who showed that the absolute values of fractional N anomalies among four centers (UCAR, WEGC, JPL, and GFZ (German Research Centre for Geosciences)) are 0.2 % from 8 to 25 km altitude. The larger differences between the various RO processing centers at lower altitudes primarily come from different handling of profiles experiencing (1) atmospheric multipath, (2) receiver tacking errors, and (3) super-refraction (see Ho et al., 2009, for details on the RO processing center procedures). This is especially true for direct retrievals (such as the UCAR direct and JPL direct), where both RO N and a priori T are assigned zero error, and the differences in Fig. 10a and b are dominated by the previously mentioned conditions. For 1D-Var retrievals, another potential source of differences is the N error model in the respective 1D-Var retrieval. All these factors vary with latitude and general atmospheric conditions.

For q (Fig. 10c, d), the structural uncertainty generally increases with increasing altitude (since the impact of water vapor on N decreases with increasing altitude). At Guam, it is about 2 % in the PBL, increases sharply to 5 % around 800 hPa, and stays around 5 to 8 % above. At the Japanese stations, the structural uncertainty increases constantly with increasing altitude, from 2 % close to the surface to 5 % at 400 hPa. At both locations, the center anomalies increase sharply at 350 hPa, which indicates again that RO-derived humidity has high uncertainty at and above that level.

7 Conclusions

We compared three observational data sets (RO, RS, and AIRS) and two model data sets (ERA and GFS) over the year 2007. Rather than comparing averages over larger timescales and regions, we compared individual profiles over specific locations (in the tropical and subtropical west Pacific). The data sets that were compared to ERA, which we considered the reference data set, include profiles from four different RO retrievals (UCAR direct, UCAR 1D-Var, WEGC 1D-Var, JPL direct), RS, AIRS, GFS analysis, ERA PERSIST, and ERA CLIMO (the last two to set a quality baseline). We

studied both the time series of profile pairs and the mean and rms computed for the four seasons and three pressure layers (1000 to 800, 800 to 600, and 600 to 400 hPa). As expected, we found different characteristics for each data set. Our main conclusions are as follows:

1. For all four RO humidity retrievals, the magnitude of the mean biases relative to ERA is smaller than or comparable to those of the RS and AIRS in the 800–400 hPa layer. Above 600 hPa, differences between the various RO humidity retrievals generally become larger (Figs. 6 and 7, top).

2. All data sets have smaller rms differences than both CLIMO and PERSIST (Figs. 6 and 7, bottom). The exception is the tropical 1000–800 hPa layer, where all rms values are comparable in magnitude due to the nearly constant humidity conditions throughout the year. This confirms that all observational data sets contribute valuable information compared to persistence and climatology.

3. The rms of all RO retrievals is comparable to or lower than the rms of the RS and AIRS for all pressure layers below 400 hPa, which confirms the high quality of RO profiles (Figs. 6 and 7, bottom). The agreement among the four different retrievals of specific humidity in the lower and middle troposphere validates the stability of the four retrievals.

4. In the time series, the four RO retrievals agree within 10 % in the 1000–600 hPa layer (Fig. 5). Differences become larger in the 600–400 hPa layer, where the UCAR 1D-Var gets drier, the UCAR direct alternates between too dry and too wet, and both the WEGC 1D-Var and JPL direct become too wet. Since water vapor decreases exponentially with altitude, the retrieval becomes more and more sensitive to the prescribed temperature, which can lead to larger humidity differences.

5. The structural uncertainty of RO humidity retrievals is estimated from anomalies of RO retrievals from the inter-center mean. Maximum differences among retrievals from 1000 to 400 hPa are between 1 and 0.2 % for refractivity, and 3 and 10 % for specific humidity (Fig. 10).

6. RO has the potential to contribute valuable information on water vapor via data assimilation in the mid- and lower troposphere, especially when high-quality RS are unavailable (Southern Hemisphere, over oceans). In contrast to infrared or microwave sounders, RO can resolve strong vertical gradients of humidity.

7. AIRS is biased dry throughout the entire troposphere, as noted previously (Wong et al., 2015). This bias is particularly strong for wet atmospheric conditions (Fig. 8).

8. All data sets show increased humidity and temperature values during a typhoon passage (Fig. 9). Differences from ERA do not change noticeably during a typhoon passage, indicating that all data sets and ERA report a signal that is similar in magnitude during the typhoon passages.

We find that the alternating wet and dry seasons at Guam, together with the very sharp transition at the top of the planetary boundary layer in the dry season at Guam, are especially challenging for the RO, RS, and AIRS observational systems compared to the conditions at the subtropical Japanese locations. The results comparing the different data sets to the ERA are similar at the three Japanese RS stations.

All the observational data sets at the Japanese stations show a response to the rapid increase of water vapor throughout the troposphere during the passage of typhoons; however, the AIRS response is weaker than the RS and RO responses, probably because of the extensive clouds associated with the typhoons.

Our results support the findings of Vergados et al. (2018), e.g., the relative dryness of the UCAR 1D-Var and wetness of the JPL RO humidity retrieval, and the dry bias of AIRS. While Vergados et al. (2018) draw their conclusions from large-scale multi-year climatologies, we use high-resolution time series to depict the short-term and small-scale variability of humidity, and we add results below 700 hPa, where the tropospheric water vapor content is highest.

We conclude that the accuracy of RO humidity retrievals is comparable to or better than both standard RS and AIRS data at the four tropical and subtropical locations studied here above 800 hPa, as well as below 800 hPa if super-refraction is absent. If assigned smaller errors (and therefore greater weights) in the assimilation process, RO could have a positive impact on improving the water vapor analysis in data assimilation in the lower and mid-troposphere.

Code and data availability. Code and data will be made available by the authors upon request.

The Supplement related to this article is available online at https://doi.org/10.5194/amt-11-3091-2018-supplement.

Author contributions. TR and RA formulated the initial idea and developed the design of this work. WR, UF, and SPH contributed ideas and provided valuable feedback. TR collected the data, performed all the computational work and coding necessary, performed the analysis, and prepared the manuscript. RA contributed significantly to the data analysis and the writing.

Competing interests. The authors declare that they have no conflict of interest.

Acknowledgements. Therese Rieckh, Richard Anthes, and Shu-Peng Ho were supported by the National Science Foundation (NSF)-NASA grant AGS-1522830. William Randel was supported through the NSF-UCAR cooperative agreement for the management of NCAR and NASA RNSS Science Team grant NNX16AK37G. The ERA data were provided by the Data Support Section of the Computational and Information Systems Laboratory, NCAR, which is sponsored by the NSF. We thank the COSMIC CDAAC team for providing the RO Level 2 data. We also thank Eric DeWeaver (NSF) and Jack Kaye (NASA) for their long-term advice and support to the COSMIC science program. COSMIC is supported by the National Space Office (NSPO) of Taiwan, NSF, NASA, NOAA, and the U.S. Air Force. We thank the WEGC processing team members (Marc Schwärz, Florian Ladstädter, Barbara Angerer) for providing the OPSv5.6 RO data, and we thank Robert Khachikyan for making the JPL RO retrievals publicly available through the AGAPE interactive search tool. We thank the NASA Earth Observing System Data and Information System for making the AIRS data publicly available. We thank the team of the Integrated Global Radiosonde Archive for documenting and providing global radiosonde data. We thank two anonymous reviewers for their constructive comments.

Edited by: Brian Kahn
Reviewed by: two anonymous referees

References

Anthes, R. and Rieckh, T.: Estimating observation and model error variances using multiple data sets, Atmos. Meas. Tech. Discuss., https://doi.org/10.5194/amt-2017-487, in review, 2018.

Anthes, R. A.: Exploring Earth's atmosphere with radio occultation: contributions to weather, climate and space weather, Atmos. Meas. Tech., 4, 1077–1103, https://doi.org/10.5194/amt-4-1077-2011, 2011.

Anthes, R. A., Ector, D., Hunt, D. C., Kuo, Y.-H., Rocken, C., Schreiner, W. S., Sokolovskiy, S. V., Syndergaard, S., Wee, T.-K., Zeng, Z., Bernhardt, P. A., Dymond, K. F., Chen, Y., Liu, H., Manning, K., Randel, W. J., Trenberth, K. E., Cucurull, L., Healy, S. B., Ho, S.-P., McCormick, C., Meehan, T. K., Thompson, D. C., and Yen, N. L.: The COSMIC/FORMOSAT-3 Mission: Early Results, B. Am. Meteorol. Soc., 89, 313–333, https://doi.org/10.1175/BAMS-89-3-313, 2008.

Bodeker, G. E., Bojinski, S., Cimini, D., Dirksen, R. J., Haeffelin, M., Hannigan, J. W., Hurst, D. F., Leblanc, T., Madonna, F., Maturilli, M., Mikalsen, A. C., Philipona, R., Reale, T., Seidel, D. J., Tan, D. G. H., Thorne, P. W., Vömel, H., and Wang, J.: Reference Upper-Air Observations for Climate: From Concept to Reality, B. Am. Meteorol. Soc., 97, 123–135, https://doi.org/10.1175/BAMS-D-14-00072.1, 2016.

Chou, M.-D., Weng, C.-H., and Lin, P.-H.: Analyses of FORMOSAT-3/COSMIC humidity retrievals and comparisons with AIRS retrievals and NCEP/NCAR reanalyses, J. Geophys. Res., 114, D00G03, https://doi.org/10.1029/2008JD010227, 2009.

Dai, A., Wang, J., Thorne, P. W., Parker, D. E., Haimberger, L., and Wang, X. L.: A New Approach to Homogenize Daily Radiosonde Humidity Data, J. Climate, 24, 965–991, https://doi.org/10.1175/2010JCLI3816.1, 2011.

Dee, D. P., Uppala, S. M., Simmons, A. J., Berrisford, P., Poli, P., Kobayashi, S., Andrae, U., Balmaseda, M. A., Balsamo, G., Bauer, P., Bechtold, P., Beljaars, A. C. M., van de Berg, L., Bidlot, J., Bormann, N., Delsol, C., Dragani, R., Fuentes, M., Geer, A. J., Haimberger, L., Healy, S. B., Hersbach, H., Hólm, E. V., Isaksen, L., Kållberg, P., Köhler, M., Matricardi, M., McNally, A. P., Monge-Sanz, B. M., Morcrette, J.-J., Park, B.-K., Peubey, C., de Rosnay, P., Tavolato, C., Thépaut, J.-N., and Vitart, F.: The ERA-Interim reanalysis: configuration and performance of the data assimilation system, Q. J. Roy. Meteor. Soc., 137, 553–597, https://doi.org/10.1002/qj.828, 2011.

Emanuel, K. A.: The theory of hurricanes, Annu. Rev. Fluid Mech., 23, 179–196, https://doi.org/10.1146/annurev.fl.23.010191.001143, 1991.

Garratt, J.: The Atmospheric Boundary Layer, Cambridge Univ. Press, 1992.

Gilpin, S., Rieckh, T., and Anthes, R.: Reducing representativeness and sampling errors in radio occultation-radiosonde comparisons, Atmos. Meas. Tech., 11, 2567–2582, https://doi.org/10.5194/amt-11-2567-2018, 2018.

Gorbunov, M. E., Benzon, H.-H., Jensen, A. S., Lohmann, M. S., and Nielsen, A. S.: Comparative analysis of radio occultation processing approaches based on Fourier integral operators, Radio Sci., 39, RS6004, https://doi.org/10.1029/2003RS002916, 2004.

Hajj, G. A., Kursinski, E. R., Romans, L. J., Bertiger, W. I., and Leroy, S. S.: A technical description of atmospheric sounding by GPS occultation, J. Atmos. Sol.-Terr. Phy., 64, 451–469, https://doi.org/10.1016/S1364-6826(01)00114-6, 2002.

Ho, S.-P., Kirchengast, G., Leroy, S., Wickert, J., Mannucci, A. J., Steiner, A. K., Hunt, D., Schreiner, W., Sokolovskiy, S., Ao, C., Borsche, M., von Engeln, A., Foelsche, U., Heise, S., Iijima, B., Kuo, Y.-H., Kursinski, E. R., Pirscher, B., Ringer, M., Rocken, C., and Schmidt, T.: Estimating the uncertainty of using GPS radio occultation data for climate monitoring: Intercomparison of CHAMP refractivity climate records from 2002 to 2006 from different data centers, J. Geophys. Res., 114, D23107, https://doi.org/10.1029/2009JD011969, 2009.

Ho, S.-P., Zhou, X., Kuo, Y.-H., Hunt, D., and Wang, J.-H.: Global evaluation of radiosonde water vapor systematic biases using GPS radio occultation from COSMIC and ECMWF analysis, Remote Sensing, 2, 1320–1330, https://doi.org/10.3390/RS2051320, 2010.

Ho, S.-P., Hunt, D., Steiner, A. K., Mannucci, A. J., Kirchengast, G., Gleisner, H., Heise, S., von Engeln, A., Marquardt, C., Sokolovskiy, S., Schreiner, W., Scherllin-Pirscher, B., Ao, C., Wickert, J., Syndergaard, S., Lauritsen, K. B., Leroy, S., Kursinski, E. R., Kuo, Y.-H., Foelsche, U., Schmidt, T., and Gorbunov, M.: Reproducibility of GPS radio occultation data for climate monitoring: Profile-to-profile inter-comparison of CHAMP climate records 2002 to 2008 from six data centers, J. Geophys. Res., 117, D18111, https://doi.org/10.1029/2012JD017665, 2012.

Ho, S.-P., Peng, L., Mears, C., and Anthes, R. A.: Comparison of global observations and trends of total precipitable water derived from microwave radiometers and COSMIC radio occultation from 2006 to 2013, Atmos. Chem. Phys., 18, 259–274, https://doi.org/10.5194/acp-18-259-2018, 2018.

Kahn, B. H., Irion, F. W., Dang, V. T., Manning, E. M., Nasiri, S. L., Naud, C. M., Blaisdell, J. M., Schreier, M. M., Yue, Q., Bowman, K. W., Fetzer, E. J., Hulley, G. C., Liou, K. N., Lubin, D., Ou, S. C., Susskind, J., Takano, Y., Tian, B., and Worden, J. R.: The Atmospheric Infrared Sounder version 6 cloud products, Atmos. Chem. Phys., 14, 399–426, https://doi.org/10.5194/acp-14-399-2014, 2014.

Kursinski, E. R., Hajj, G. A., Hardy, K. R., Romans, L. J., and Schofield, J. T.: Observing tropospheric water vapor by radio occultation using the Global Positioning System, Geophys. Res. Lett., 22, 2365–2368, https://doi.org/10.1029/95GL02127, 1995.

Kursinski, E. R., Hajj, G. A., Schofield, J. T., Linfield, R. P., and Hardy, K. R.: Observing Earth's atmosphere with radio occultation measurements using the Global Positioning System, J. Geophys. Res., 102, 23429–23465, https://doi.org/10.1029/97JD01569, 1997.

Ladstädter, F., Steiner, A. K., Schwärz, M., and Kirchengast, G.: Climate intercomparison of GPS radio occultation, RS90/92 radiosondes and GRUAN from 2002 to 2013, Atmos. Meas. Tech., 8, 1819–1834, https://doi.org/10.5194/amt-8-1819-2015, 2015.

Melbourne, W. G., Davis, E. S., Duncan, C. B., Hajj, G. A., Hardy, K. R., Kursinski, E. R., Meehan, T. K., Young, L. E., and Yunck, T. P.: The application of spaceborne GPS to atmospheric limb sounding and global change monitoring, JPL Publication, 94–18, 147, 1994.

Miloshevich, L. M., Vömel, H., Whiteman, D. N., Lesht, B. M., Schmidlin, F. J., and Russo, F.: Absolute accuracy of water vapor measurements from six operational radiosonde types launched during AWEX-G and implications for AIRS validation, J. Geophys. Res., 111, D09S10, https://doi.org/10.1029/2005JD006083, 2006.

Poli, P., Joiner, J., and Kursinski, E.: 1DVAR analysis of temperature and humidity using GPS radio occultation refractivity data, J. Geophys. Res., 107, 4448, https://doi.org/10.1029/2001JD000935, 2002.

Poli, P., Healy, S. B., and Dee, D. P.: Assimilation of Global Positioning System radio occultation data in the ECMWF ERA-Interim reanalysis, Q. J. Roy. Meteor. Soc., 136, 1972–1990, https://doi.org/10.1002/qj.722, 2010.

Randel, W. J., Rivoire, L., Pan, L., and Honomichl, S.: Dry layers in the tropical troposphere observed during CONTRAST and global behavior from GFS analyses, J. Geophys. Res., 121, 14142–14158, https://doi.org/10.1002/2016JD025841, 2016.

Rieckh, T., Anthes, R., Randel, W., Ho, S.-P., and Foelsche, U.: Tropospheric dry layers in the tropical western Pacific: comparisons of GPS radio occultation with multiple data sets, Atmos. Meas. Tech., 10, 1093–1110, https://doi.org/10.5194/amt-10-1093-2017, 2017.

Schwärz, M., Kirchengast, G., Scherllin-Pirscher, B., Schwarz, J., Ladstädter, F., and Angerer, B.: Multi-Mission Validation by Satellite Radio Occultation – Extension Project, Wegener center/uni graz technical report for esa/esrin no. 01/2016, issue 1.1, Wegener Center for Climate and Global Change, University of Graz, 2016.

Smith, E. and Weintraub, S.: The constants in the equation for atmospheric refractive index at radio frequencies, P. IRE, 41, 1035–1037, 1953.

Sokolovskiy, S., Rocken, C., Hunt, D., Schreiner, W., Johnson, J., Masters, D., and Esterhuizen, S.: GPS profiling of the lower troposphere from space: Inversion and demodulation of the open-loop radio occultation signals, Geophys. Res. Lett., 33, 14, https://doi.org/10.1029/2006GL026112, 2006.

Steiner, A. K., Hunt, D., Ho, S.-P., Kirchengast, G., Mannucci, A. J., Scherllin-Pirscher, B., Gleisner, H., von Engeln, A., Schmidt, T., Ao, C., Leroy, S. S., Kursinski, E. R., Foelsche, U., Gorbunov, M., Heise, S., Kuo, Y.-H., Lauritsen, K. B., Marquardt, C., Rocken, C., Schreiner, W., Sokolovskiy, S., Syndergaard, S., and Wickert, J.: Quantification of structural uncertainty in climate data records from GPS radio occultation, Atmos. Chem. Phys., 13, 1469–1484, https://doi.org/10.5194/acp-13-1469-2013, 2013.

Susskind, J., Barnet, C. D., and Blaisdell, J.: Retrieval of atmospheric and surface parameters from AIRS/AMSU/HSB data in the presence of clouds, IEEE T. Geosci. Remote, 41, 390–409, https://doi.org/10.1109/TGRS.2002.808236, 2003.

Susskind, J., Blaisdell, J. M., and Iredell, L.: Improved methodology for surface and atmospheric soundings, error estimates, and quality control procedures: the atmospheric infrared sounder science team version-6 retrieval algorithm, J. Appl. Remote Sens., 8, https://doi.org/10.1117/1.JRS.8.084994, 2014.

Vergados, P., Mannucci, A. J., and Ao, C. O.: Assessing the performance of GPS radio occultation measurements in retrieving tropospheric humidity in cloudiness: A comparison study with radiosondes, ERA-Interim, and AIRS data sets, J. Geophys. Res., 119, 7718–7731, https://doi.org/10.1002/2013JD021398, 2014.

Vergados, P., Mannucci, A. J., Ao, C. O., Jiang, J. H., and Su, H.: On the comparisons of tropical relative humidity in the lower and middle troposphere among COSMIC radio occultations and MERRA and ECMWF data sets, Atmos. Meas. Tech., 8, 1789–1797, https://doi.org/10.5194/amt-8-1789-2015, 2015.

Vergados, P., Mannucci, A. J., Ao, C. O., Verkhoglyadova, O., and Iijima, B.: Comparisons of the tropospheric specific humidity from GPS radio occultations with ERA-Interim, NASA MERRA, and AIRS data, Atmos. Meas. Tech., 11, 1193–1206, https://doi.org/10.5194/amt-11-1193-2018, 2018.

Vömel, H., Selkirk, H. B., Miloshevich, L., Valverde-Canossa, J., Valdés, J., Kyrö, E., Kivi, R., Stolz, W., Peng, G., and Diaz, J. A.: Radiation Dry Bias of the Vaisala RS92 Humidity Sensor, J. Atmos. Ocean. Tech., 24, 953–963, https://doi.org/10.1175/JTECH2019.1, 2007.

Wang, B.-R., Liu, X.-Y., and Wang, J.-K.: Assessment of COSMIC radio occultation retrieval product using global radiosonde data, Atmos. Meas. Tech., 6, 1073–1083, https://doi.org/10.5194/amt-6-1073-2013, 2013.

Wang, J. and Zhang, L.: Systematic Errors in Global Radiosonde Precipitable Water Data from Comparisons with Ground-Based GPS Measurements, J. Climate, 21, 2218–2238, https://doi.org/10.1175/2007JCLI1944.1, 2008.

Ware, R., Exner, M., Gorbunov, M., Hardy, K., Herman, B., Kuo, Y., Meehan, T., Melbourne, W., Rocken, C., Schreiner, W., Sokolovskiy, S., Solheim, F., Zou, X., Anthes, R., Businger, S., and Trenberth, K.: GPS Sounding of the Atmosphere from Low Earth Orbit: Preliminary Re-

sults, B. Am. Meteorol. Soc., 77, https://doi.org/10.1175/1520-0477(1996)077<0019:GSOTAF>2.0.CO;2, 1996.

Wong, S., Fetzer, E. J., Schreier, M., Manipon, G., Fishbein, E. F., Kahn, B. H., Yue, Q., and Irion, F. W.: Cloud-induced uncertainties in AIRS and ECMWF temperature and specific humidity, J. Geophys. Res., 120, 1880–1901, https://doi.org/10.1002/2014JD022440, 2015.

Xie, F., Wu, D., Ao, C., Kursinski, E., Manucci, A., and Syndergaard, S.: Super-refraction effects on GPS radio occultation refractivity in marine boundary layers, Geophys. Res. Lett., 37, https://doi.org/10.1029/2010GL043299, 2010.

Supplement of Atmos. Meas. Tech., 11, 3091–3109, 2018
https://doi.org/10.5194/amt-11-3091-2018-supplement

Atmospheric Measurement Techniques
Open Access
EGU

Supplement of

Evaluating tropospheric humidity from GPS radio occultation, radiosonde, and AIRS from high-resolution time series

Therese Rieckh et al.

Correspondence to: Therese Rieckh (rieckh@ucar.edu)

immediate

1 Co-Location of ERA, RO, RS, and AIRS

A map with the locations of the 4 chosen RS stations is shown in Fig. S1. Details about the co-location process are depicted in Fig. S2.

2 2007 annual mean profiles

The constant value CLIMO (ERA 2007 annual mean) is used to normalize all data sets. The values for CLIMO are listed in Table S1.

3 Setting the stage: ERA 2007 time series of N, T, q, and RH

Time series for ERA refractivity, temperature, specific humidity, and relative humidity for 2007 are shown in Fig. S3 for Guam and in Fig. S4 for Ishigakijima. All data are interpolated to a common 25 hPa grid.

4 Normalized difference for specific humidity between various data sets and ERA

The Minamidaitojima 2007 RH time series are shown in Fig. S5 (top). Time series for q normalized differences between various data sets and ERA are shown in Fig. S5 (panels 2–5) and Fig. S6.

5 Normalized difference for refractivity between various data sets and ERA

Time series for refractivity N normalized differences between various data sets and ERA are shown in Fig. S7 and Fig. S8.

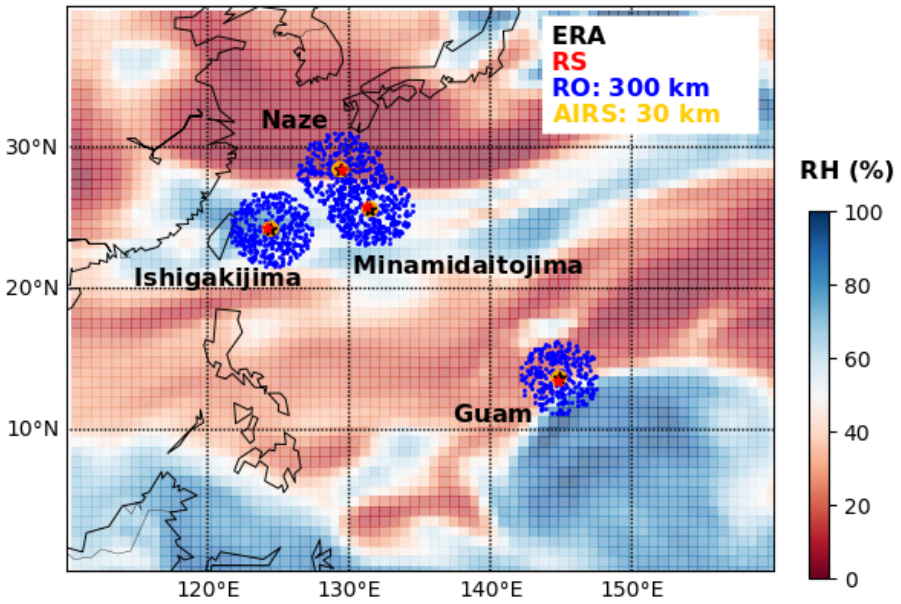

Figure S1. Map with the locations of Guam, Ishigakijima, Minamidaitojima, and Naze, and the locations of the data sets: ERA (black star), radiosonde (red star), RO (blue dots), and AIRS (yellow circle). The ERA relative humidity field at 700 hPa for one day is shown in the background.

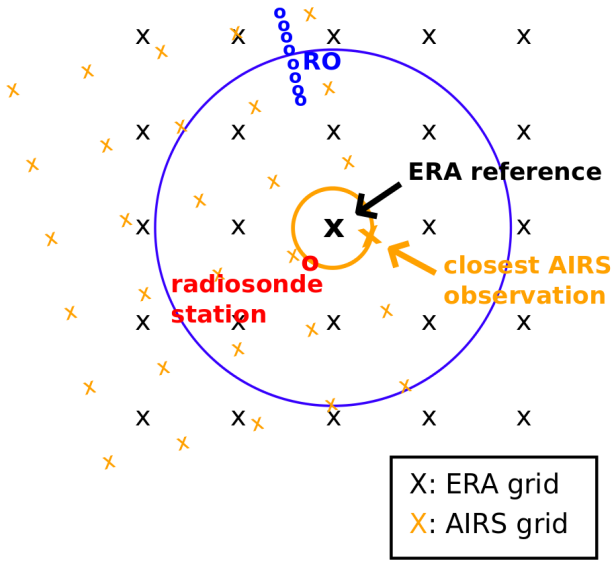

Figure S2. Sketch of the co-location of RO, RS, and AIRS with the ERA reference point for one point in time. ROs are chosen if their mean tangent point is within 300 km from the ERA reference.

Table S1. Mean annual values for refractivity, specific humidity, relative humidity, and temperature for ERA in 2007, interpolated on a 25 hPa grid.

Pressure	**Refractivity (N-units)**				**Specific Humidity ($g\,kg^{-1}$)**				**Relative Humidity (%)**				**Temperature (°C)**			
(hPa)	Guam	Ishi	Mina	Naze	Guam	Ishi	Mina	Naze	Guam	Ishi	Mina	Naze	Guam	Ishi	Mina	Naze
300	96.7	96.8	97.0	97.5	0.3	0.3	0.3	0.3	41.6	37.8	38.8	40.3	-29.8	-30.3	-30.9	-32.1
325	103.1	103.3	103.5	104.1	0.4	0.4	0.4	0.4	39.1	37.6	38.3	40.7	-25.6	-26.5	-27.0	-28.5
350	109.8	110.3	110.4	111.2	0.6	0.6	0.5	0.5	36.6	37.5	37.7	41.2	-21.5	-22.6	-23.2	-24.9
375	116.4	117.1	117.1	117.9	0.7	0.7	0.7	0.6	35.6	37.7	37.5	40.9	-18.1	-19.5	-20.1	-21.8
400	123.5	124.3	124.3	125.1	0.9	0.9	0.9	0.8	34.5	37.9	37.3	40.6	-14.8	-16.4	-16.9	-18.7
425	130.4	131.3	131.1	132.0	1.1	1.1	1.0	1.0	35.0	38.3	37.1	40.6	-12.0	-13.7	-14.2	-16.0
450	137.7	138.7	138.4	139.3	1.4	1.4	1.3	1.2	35.5	38.7	37.0	40.6	-9.3	-11.0	-11.5	-13.3
475	145.0	146.0	145.6	146.4	1.7	1.7	1.5	1.5	36.9	39.7	37.9	41.3	-6.9	-8.6	-9.1	-10.8
500	152.8	153.7	153.2	154.0	2.0	2.0	1.8	1.7	38.3	40.8	38.9	42.0	-4.4	-6.3	-6.6	-8.4
525	160.4	161.4	160.8	161.4	2.3	2.3	2.1	2.0	39.7	42.4	40.7	43.0	-2.4	-4.2	-4.5	-6.3
550	168.4	169.5	168.9	169.3	2.7	2.7	2.5	2.3	41.1	44.0	42.4	43.9	-0.3	-2.1	-2.4	-4.2
575	176.4	177.7	176.9	177.1	3.0	3.1	2.9	2.6	42.8	46.1	44.4	45.3	1.5	-0.2	-0.6	-2.4
600	184.7	186.3	185.4	185.4	3.5	3.6	3.3	3.0	44.6	48.2	46.3	46.8	3.4	1.7	1.3	-0.6
625	193.1	195.0	193.8	193.5	3.9	4.0	3.7	3.4	45.8	50.2	48.1	48.2	5.3	3.4	3.1	1.1
650	202.0	204.1	202.7	202.0	4.5	4.6	4.2	3.8	47.1	52.3	49.9	49.6	7.3	5.1	4.8	2.8
675	211.2	213.3	211.5	210.3	5.0	5.1	4.7	4.1	48.7	54.6	51.6	50.7	9.0	6.7	6.3	4.3
700	220.8	222.9	220.8	219.0	5.7	5.7	5.2	4.6	50.4	56.9	53.3	51.8	10.7	8.2	7.8	5.8
725	231.1	232.4	229.9	227.5	6.3	6.2	5.6	4.9	53.1	59.0	55.0	52.6	12.1	9.5	9.1	7.0
750	241.8	242.3	239.5	236.3	7.1	6.8	6.2	5.3	55.9	61.1	56.6	53.5	13.6	10.8	10.3	8.3
775	253.9	252.4	249.5	245.3	8.1	7.3	6.7	5.7	60.1	63.4	59.3	54.9	14.8	12.0	11.4	9.4
800	267.1	263.0	260.3	254.9	9.2	8.0	7.4	6.2	65.4	66.3	63.0	56.9	15.9	13.1	12.4	10.5
825	281.5	274.7	271.9	265.7	10.4	8.7	8.2	6.8	71.5	70.5	67.4	61.3	16.9	14.0	13.4	11.5
850	295.9	287.0	283.8	277.7	11.6	9.6	8.9	7.6	76.6	74.7	71.5	66.9	17.9	15.1	14.3	12.4
875	310.2	299.6	295.8	290.2	12.8	10.5	9.7	8.5	80.5	78.1	75.0	72.5	19.1	16.1	15.4	13.5
900	324.2	312.5	308.4	303.3	13.9	11.4	10.6	9.5	83.2	81.1	78.3	77.6	20.4	17.3	16.5	14.6
925	337.6	325.4	321.5	316.1	14.9	12.4	11.6	10.4	84.2	83.0	80.9	80.5	21.8	18.6	17.8	16.0
950	352.0	338.2	334.5	328.2	16.0	13.3	12.5	11.2	86.6	83.7	82.5	81.1	22.9	20.0	19.1	17.4
975	363.4	349.7	346.1	338.9	16.7	14.0	13.3	11.9	84.3	81.8	81.2	79.1	24.6	21.6	20.7	19.1
1000	371.6	358.8	354.5	347.3	17.1	14.5	13.7	12.3	78.0	76.7	75.8	74.1	26.6	23.6	22.7	21.1

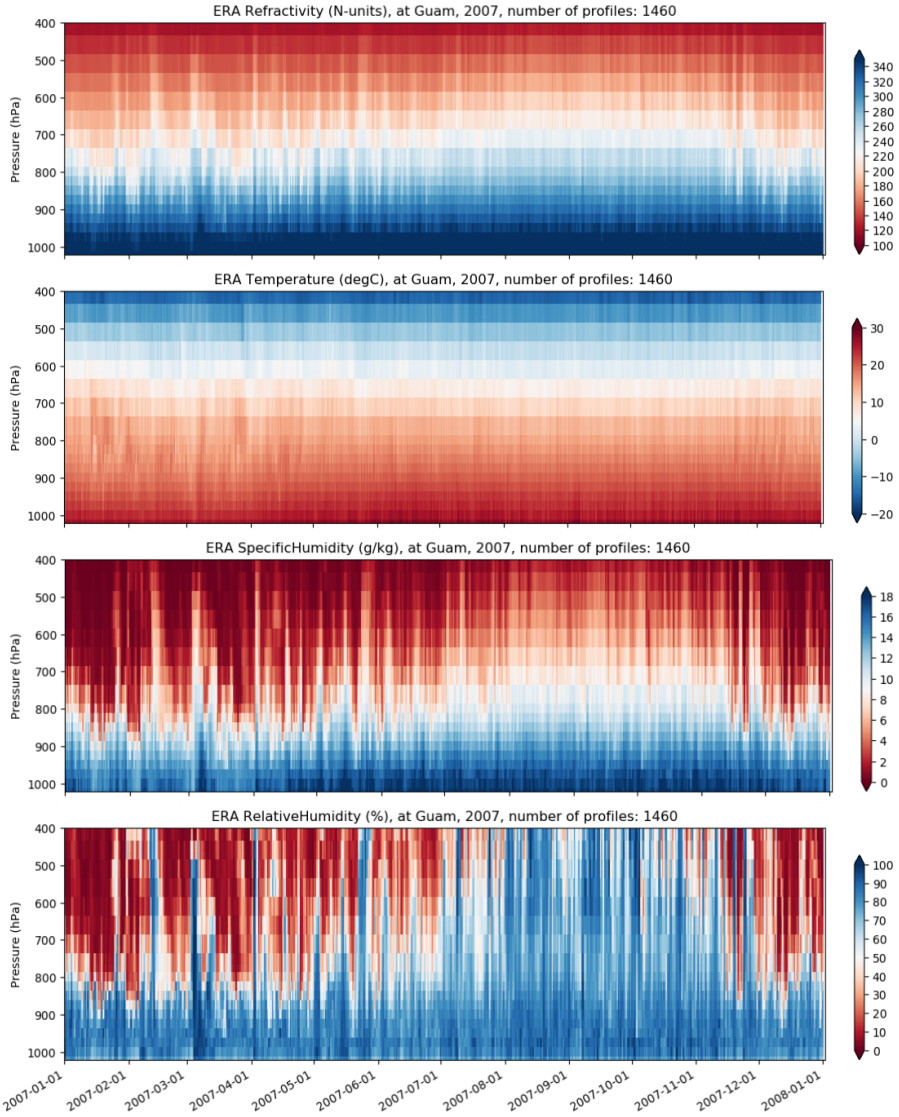

Figure S3. ERA 2007 time series at Guam for refractivity, temperature, specific humidity, and relative humidity (top to bottom).

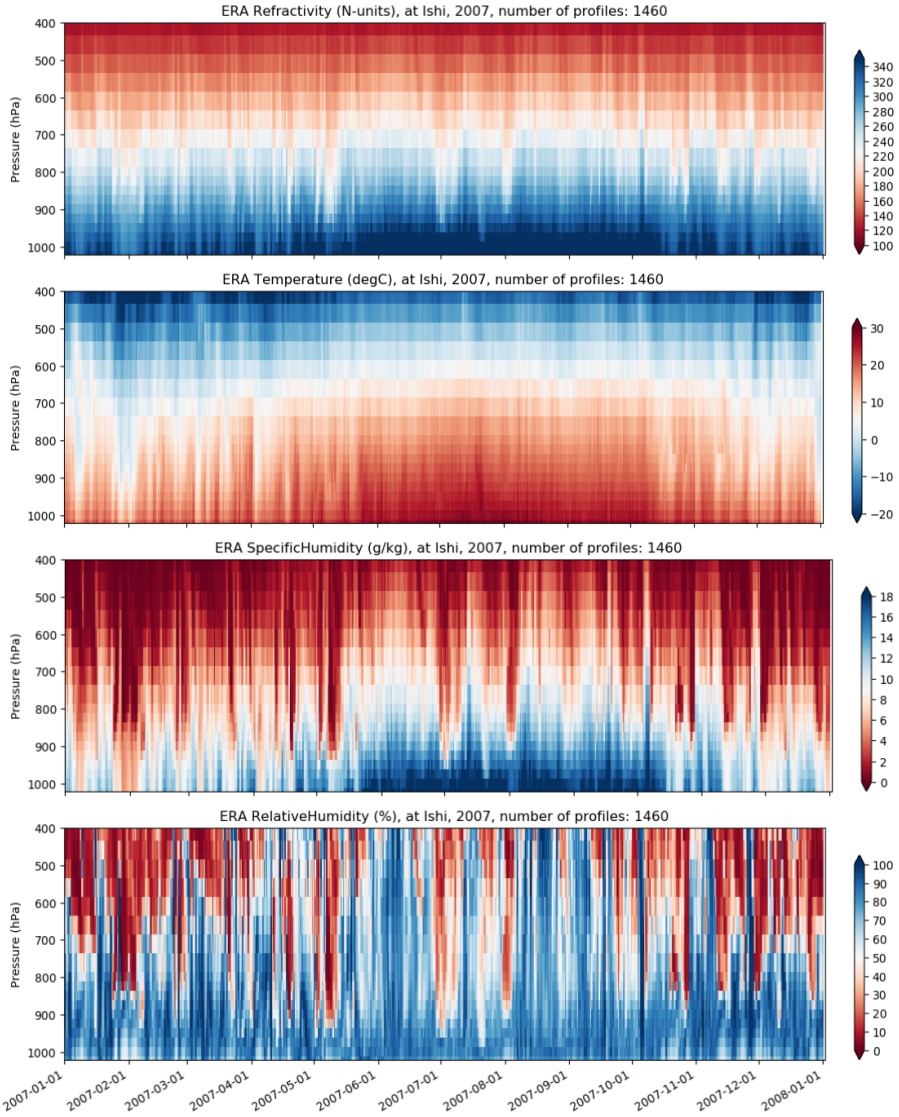

Figure S4. ERA 2007 time series at Ishigakijima for refractivity, temperature, specific humidity, and relative humidity (top to bottom).

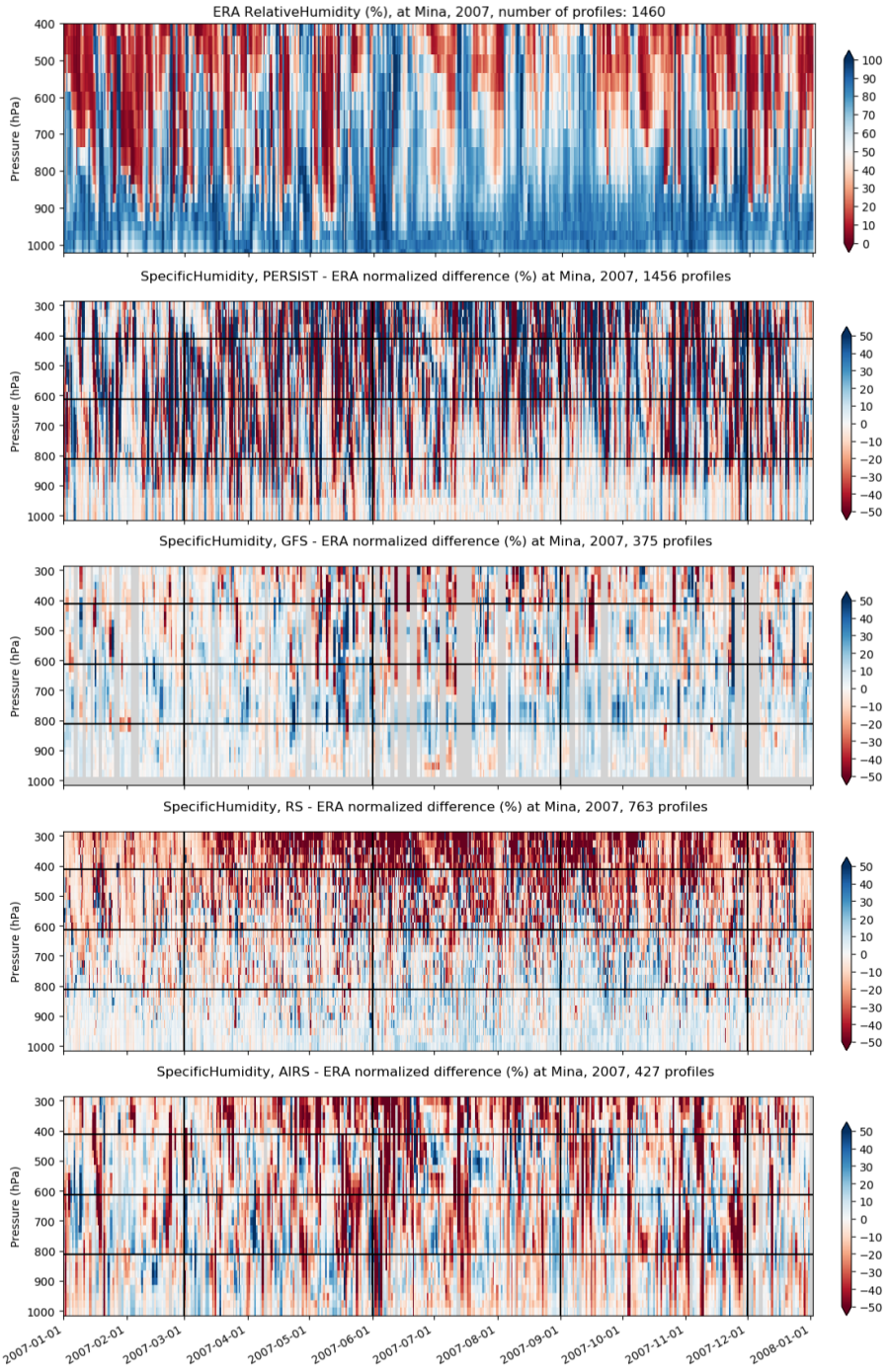

Figure S5. Top panel: 2007 time series of the relative humidity (%) at Minamidaitojima over 2007 with blue representing moist air and red representing dry air. Other panels: Normalized difference of specific humidity for PERSIST, GFS, RS, and AIRS compared to ERA at Minamidaitojima, 2007.

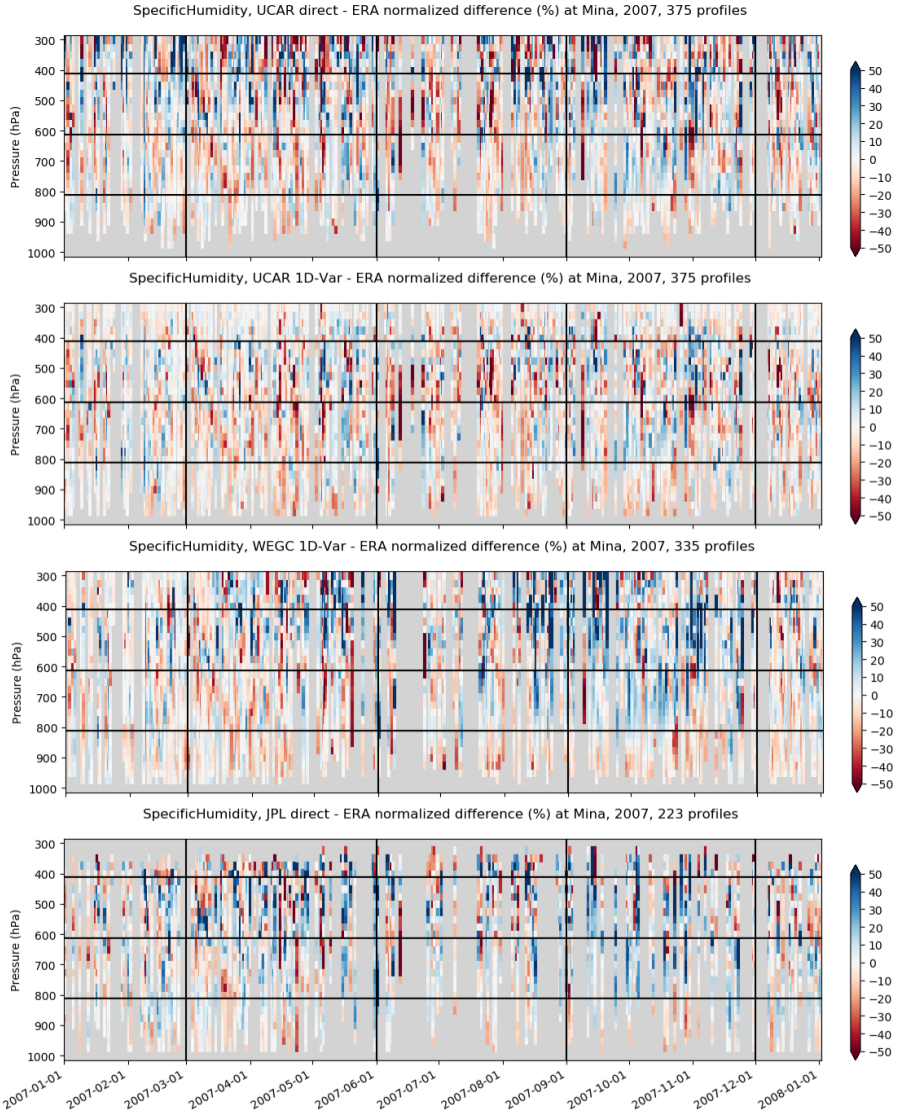

Figure S6. Normalized difference of specific humidity for the RO retrievals UCAR direct, UCAR 1D-Var, WEGC 1D-Var, and JPl direct compared to ERA at Minamidaitojima, 2007.

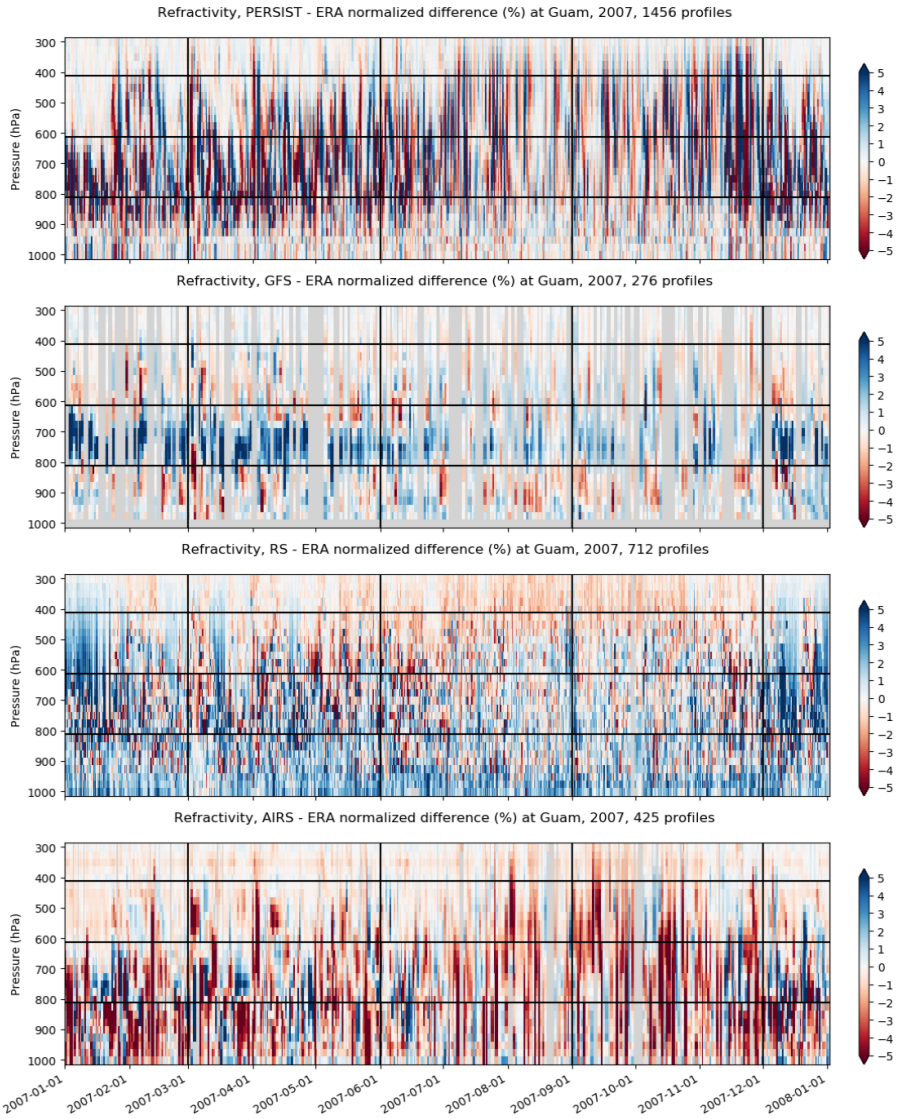

Figure S7. Normalized difference for refractivity for PERSIST, GFS, RS, and AIRS compared to ERA at Guam, 2007.

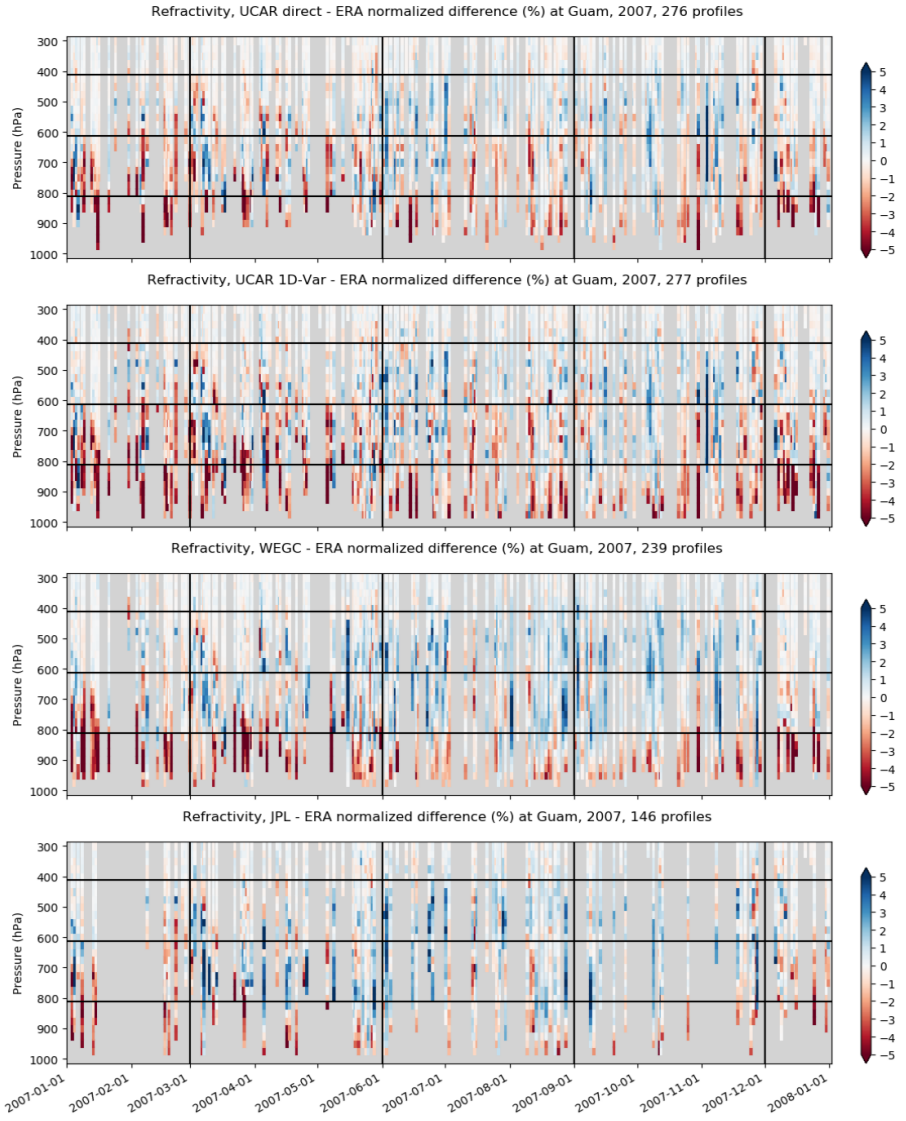

Figure S8. Normalized difference for refractivity for the RO retrievals UCAR direct, UCAR 1D-Var, WEGC 1D-Var, and JPl direct compared to ERA at Guam, 2007.

Atmos. Meas. Tech., 11, 4239–4260, 2018
https://doi.org/10.5194/amt-11-4239-2018

Atmospheric Measurement Techniques
Open Access
EGU

Estimating observation and model error variances using multiple data sets

Richard Anthes[1] **and Therese Rieckh**[1,2]

[1]COSMIC Program Office, University Corporation for Atmospheric Research, Boulder, Colorado, USA
[2]Wegener Center for Climate and Global Change, University of Graz, Graz, Austria

Correspondence: Richard Anthes (anthes@ucar.edu)

Received: 29 December 2017 – Discussion started: 18 January 2018
Revised: 21 June 2018 – Accepted: 22 June 2018 – Published: 19 July 2018

Abstract. In this paper we show how multiple data sets, including observations and models, can be combined using the "three-cornered hat" (3CH) method to estimate vertical profiles of the errors of each system. Using data from 2007, we estimate the error variances of radio occultation (RO), radiosondes, ERA-Interim, and Global Forecast System (GFS) model data sets at four radiosonde locations in the tropics and subtropics. A key assumption is the neglect of error covariances among the different data sets, and we examine the consequences of this assumption on the resulting error estimates. Our results show that different combinations of the four data sets yield similar relative and specific humidity, temperature, and refractivity error variance profiles at the four stations, and these estimates are consistent with previous estimates where available. These results thus indicate that the correlations of the errors among all data sets are small and the 3CH method yields realistic error variance profiles. The estimated error variances of the ERA-Interim data set are smallest, a reasonable result considering the excellent model and data assimilation system and assimilation of high-quality observations. For the four locations studied, RO has smaller error variances than radiosondes, in agreement with previous studies. Part of the larger error variance of the radiosondes is associated with representativeness differences because radiosondes are point measurements, while the other data sets represent horizontal averages over scales of ~ 100 km.

1 Introduction

Estimating the error characteristics of any observational system or model is important for many reasons. Not only are these errors of scientific interest; they are also important for data assimilation systems and numerical weather prediction. In many modern data assimilation schemes, observations of a given type are weighted proportionally to the inverse of their error variance (e.g., Desroziers and Ivanov, 2001).

Kuo et al. (2004) and Chen et al. (2011) used the difference between radio occultation (RO) observations and short-range model forecasts to estimate the error of the RO observations, using the concept of apparent or perceived errors, defined by

$$X_{\mathrm{AE}} = X_{\mathrm{RO}} - X_{\mathrm{fcst}}, \tag{1}$$

where X_{AE} is the apparent error of the RO observation and X_{RO} and X_{fcst} are the RO observations and model forecast values, respectively.

The error variance σ_{a}^2 of the apparent error is given by

$$\sigma_{\mathrm{a}}^2 = \frac{1}{n}\sum X_{\mathrm{AE}}^2, \tag{2}$$

where n is the number of samples of observed and modeled RO at the same location and time.

The relationship between the apparent error variance σ_{a}^2, the observational error variance σ_{o}^2, and the forecast error variance σ_{f}^2 is given by

$$\sigma_{\mathrm{a}}^2 = \sigma_{\mathrm{o}}^2 + \sigma_{\mathrm{f}}^2 - 2\mathrm{COV}_{\mathrm{err}}\left(X_{\mathrm{RO}}, \mathrm{X}_{\mathrm{fcst}}\right), \tag{3}$$

where the $\mathrm{COV}_{\mathrm{err}}$ term is the error covariance between the observations and the forecasts. If the error variance of the forecast σ_{f}^2 is estimated independently, the observational error variance can be estimated from the apparent error variance, under the assumption that the observational errors are uncorrelated with the forecast errors (in which case the

COV_{err} term in Eq. 3 is zero).

$$\sigma_a^2 = \sigma_o^2 + \sigma_f^2 \quad (4)$$

We note that the apparent errors are the same as the O − B (observation minus background) or innovations as used in data assimilation methods and studies (Chen et al., 2011).

As discussed by Kuo et al. (2004) and Chen et al. (2011), the forecast error variance can be estimated by two alternative methods, the National Meteorological Center (NMC) method (Parrish and Derber, 1992) or the Hollingsworth and Lönnberg (1986) method. Kuo et al. (2004) used both methods to estimate the observational errors of RO refractivity using the National Centers for Environmental Prediction (NCEP) Aviation Model (AVN). They found that the estimated radiosonde (RS) observations had larger errors than the RO observations, due in part to representativeness errors of the RS, which provide in situ point measurements, whereas the model data were larger-scale horizontal averages similar to those of the RO data. Chen et al. (2011) used the NMC method and Weather and Research Forecast Model (WRF) to estimate the forecast error variance and then the RO refractivity error variance.

In this paper, we estimate the error variances of multiple data sets using the "three-cornered hat" (3CH) method (Gray and Allan, 1974). Unlike the apparent-error method, this method does not require independent estimates of the error variance of a forecast; it uses the differences between combinations of three data sets. The 3CH method is described in Appendix A along with the closely related "triple-collocation method" (TC; Stoffelen, 1998). The data sets may be either different model or observational data, and estimates of the error variances of all the data sets are computed by the method. We compare three observational data sets (two versions of RO retrievals and radiosondes) and two model data sets at four locations in the tropics and subtropics to estimate the error variances of all five data sets. We find that the results are consistent with each other and with previous error estimates, where available.

2 Discussion of data sets

We use five data sets from an entire year (2007) in this study. Rieckh et al. (2018) extensively studied the properties of these data sets and their daily variability over 2007 in the tropical and subtropical western Pacific. They are described in more detail there but are summarized briefly here for convenience.

We chose 2007 for the year of our study because the number of COSMIC (Constellation Observing System for Meteorology, Ionosphere, and Climate) RO observations was near a maximum at this time. Because the primary interest in Rieckh et al. (2018) was the evaluation of water vapor observations and model analyses in challenging tropical and subtropical environments, we chose one RS station in the deep tropics and three Japanese stations in the subtropics. Because of our focus on water vapor, we carry out the analysis from 1000 to 200 hPa.

2.1 ERA-Interim

The ERA-Interim (hereafter ERA) reanalysis is a global model reanalysis produced by the European Centre for Medium-Range Weather Forecasts (ECMWF) (Dee et al., 2011). Information about the current status of ERA-Interim production, availability of data online, and near-real-time updates of various climate indicators derived from ERA-Interim data can be found at https://www.ecmwf.int/en/research/climate-reanalysis/reanalysis-datasets/era-interim.

We use the ERA analysis product, which assimilates both RS and RO data for the entire year of 2007; hence some correlation of model, RS, and RO errors is likely. However, there are many other observations going into the ERA reanalysis, and model correlations with any one observational data set are likely to be small.

2.2 NCEP Global Forecast System (GFS)

The Global Forecast System (GFS) is a forecast model produced by the National Centers for Environmental Prediction (NCEP). Data are available for download through the NOAA National Operational Model Archive and Distribution System (NOMADS). Forecast products and more information on GFS are available at https://www.ncdc.noaa.gov/data-access/model-data/model-datasets/global-forcast-system-gfs.

The GFS assimilated RS observations for the entire year 2007 but began assimilating RO data on 1 May 2007, along with many other changes to the model and analysis system (Cucurull and Derber, 2008; Kleist et al., 2009). Thus the GFS and RS and RO errors are also likely correlated to some degree. However, we computed vertical profiles of the correlation coefficients for RO and GFS refractivity, temperature, specific humidity, and relative humidity in the 2 months before and after 1 May 2007, when the GFS started assimilating RO data, and found little differences, so the error correlations between RO and GFS are likely small.

2.3 Radio occultation observations

The RO observations used in this study are re-processed data obtained from the UCAR COSMIC Data Analysis and Archive Center (CDAAC). Two methods for estimating the temperature and water vapor from the RO refractivity are used. In the direct method, the GFS temperature is used in the Smith and Weintraub (1953) equation

$$N = 77.6\frac{p}{T} + 3.73 \times 10^5 \frac{e}{T^2} \quad (5)$$

to compute water vapor pressure e from the observed refractivity N and GFS temperature T.

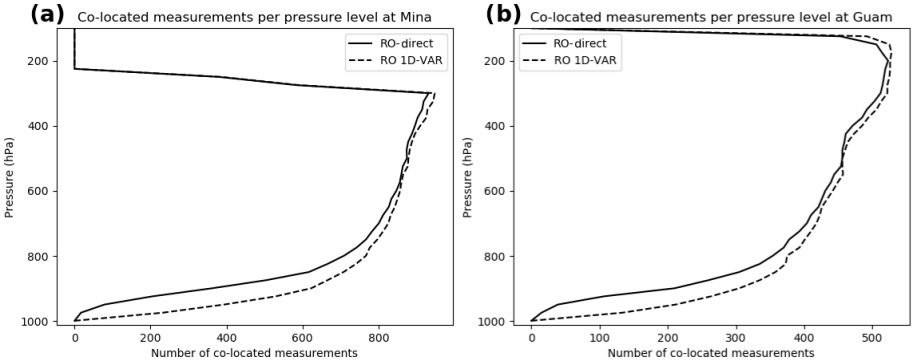

Figure 1. Number of co-located measurements for **(a)** Mina and **(b)** Guam. These are also the sample numbers in the calculations of the estimated error variances for the data sets. When using the RO 1D-VAR, the number of co-locations is slightly higher than for the RO-direct throughout the profile due to the way the 1D-VAR is computed.

A one-dimensional variational (1D-VAR) method is also used to estimate T and e from N. The 1D-VAR method uses an a priori state of the atmosphere (background profile) and an observed RO N profile to minimize a quadratic cost function. At CDAAC, an ERA-Interim profile is used as a background, which is interpolated to the time and location of the RO observation (accounting for tangent point drift during the occultation). The humidity retrieval allows an error for both T and e but only a very small error for bending angle/refractivity. Specific humidity q is then computed from the derived e.

2.4 Radiosonde observations

RS data from Guam and three Japanese stations are used in this comparison. The RS data are given on nine main pressure levels between 1000 and 200 hPa, plus additional levels if atmospheric conditions are variable. The four stations use the following sensors: Guam: VIZ/Sippican B2; Ishigakijima: Meisei; Minamidaitōjima: Vaisala RS92; and Naze: Meisei. They are launched twice daily in the hour before noon and midnight, UTC.

Guam is located in the deep tropics at 13.7° N, 144.8° E. Ishigakijima (hereafter called Ishi), Minamidaitōjima (hereafter called Mina), and Naze are located relatively close together in the western Pacific subtropics south of Japan and northeast of Taiwan:

- Naze (Kagoshima Prefecture): 28.4° N, 129.4° E
- Mina (Okinawa Prefecture): 25.6° N, 131.5° E
- Ishi (Okinawa Prefecture): 24.2° N, 124.5° E

2.5 Co-location of the data sets

The locations of the four radiosonde stations are chosen for the comparisons. We use RO observations that are located within 600 km and 3 h of the radiosonde launches. CDAAC provides GFS and ERA profiles that are already linearly interpolated in space and time to the RO location and time. These interpolated profiles, along with the RO observations, were corrected for their time and spatial differences from the radiosonde data using a model correction algorithm (described in Gilpin et al., 2018). Thus the effect of spatial and temporal differences among the data sets is expected to be minor.

The refractivity for the radiosonde and model data is computed from Eq. (5) using the pressure, temperature, and water vapor from these data. Normalized differences are computed for all combinations of the data sets (RO–ERA, RO–GFS, GFS–ERA, RS–ERA, RS–GFS, RS–RO), where RO is either the RO-direct or the RO 1D-VAR data. The ERA annual mean for 2007 at each RS station is used to normalize the differences in the data sets associated with that station. We consider the differences among all data sets for four variables: refractivity (N), temperature (T), specific humidity (q), and relative humidity (RH).

2.6 Number of samples

The number of samples is limited by the number of RO observations that are within the co-location criteria of 3 h and 600 km. Figure 1 shows the number of data samples per pressure level that meet these criteria during 2007 at Mina (the numbers at Ishi and Naze are similar) and Guam. The sharp cutoff on the top of the profiles is due to limited RS data availability at high altitudes. The smooth transition to lower numbers at the bottom results from a decrease in the number of RO observations with lower altitudes in the mid- and lower troposphere. The number of samples at the Japanese stations is a maximum of approximately 900 at 300 hPa. The number decreases to about 100 at 950 hPa. At Guam, the number ranges from a maximum of about 500 at 200 hPa to about 50 at 950 hPa. Thus the effect of the limited sample size will be greatest for the Japanese stations above 300 hPa and for

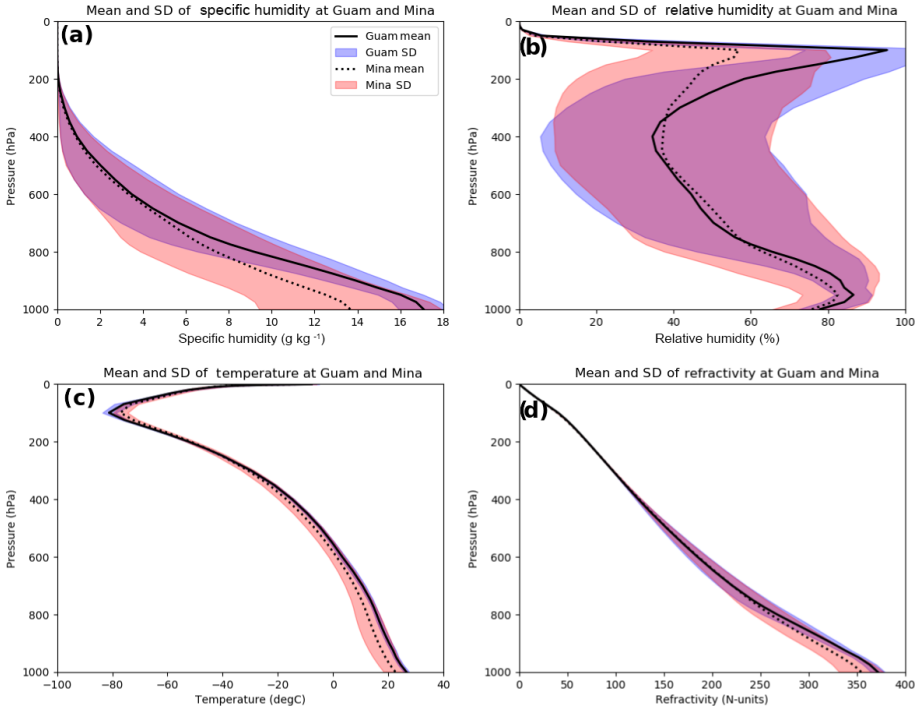

Figure 2. The mean ERA profiles over 2007 at Guam and Mina of specific humidity q **(a)**, relative humidity RH **(b)**, temperature T **(c)**, and refractivity N **(d)**. The standard deviations about the mean profiles are indicated by the shading.

all four stations below 900 hPa, where the sample size is less than 500.

2.7 Mean ERA profiles for 2007 and example of profiles and normalized-difference profiles

Before showing the statistical comparisons of the normalized differences between the data sets and their estimated errors, we present the mean ERA profiles of q, RH, T, and N at Mina and Guam for the year 2007 (Fig. 2). The standard deviations are shown by the shading around each mean profile. As shown by Fig. 2, the water vapor (especially relative humidity) shows the greatest variability over the year. The variability in specific humidity, temperature, and refractivity is greater at Mina, which is located in the subtropics, than Guam, which is located in the deep tropics.

We next present a single example of soundings from the five data sets, to illustrate how the profiles of the normalized differences of the variables (which we use in all the following calculations) compare to the actual profiles. Figure 3 illustrates the q, RH, T, and N profiles from 13 January 2007 at approximately 00:00 GMT, and Fig. 4 illustrates the corresponding profiles of the normalized differences of the variables from ERA, for example $(q - q_{\mathrm{ERA}})/\overline{q}$, where $\overline{q}$ is the 2007 mean ERA value of q.

A comparison of Figs. 3 and 4 shows that the normalized-difference profiles highlight the similarities and differences of the five data sets better than the actual profiles, especially in the upper troposphere. The magnitudes of the normalized differences are the same order of magnitude at all levels, whereas the differences in the actual profiles can vary by more than an order of magnitude from the lower to the upper troposphere. Figure 4 shows that typical percentage differences between data sets are $\sim 50\,\%$ for q and RH, $0.5\,\%$ for T, and $5\,\%$ for N.

2.8 Representativeness errors

As in the apparent-error method, the 3CH error estimates include representatives errors. Since four of the five data sets considered here are representative of horizontal averages with a length scale of ~ 100 km, while the RS data are point measurements, the differences between the RS and other data sets include a significant "representativeness" component (Kitchen, 1989). O'Carroll et al. (2008) discuss the importance of representativeness errors and how they relate to the concept of "truth" that is used in the 3CH method.

3 Derivation of error variances

In this section we summarize the derivation of the equations relating the error variances and covariances among the data sets. The complete derivation and a discussion of the limitations are given in Appendix A.

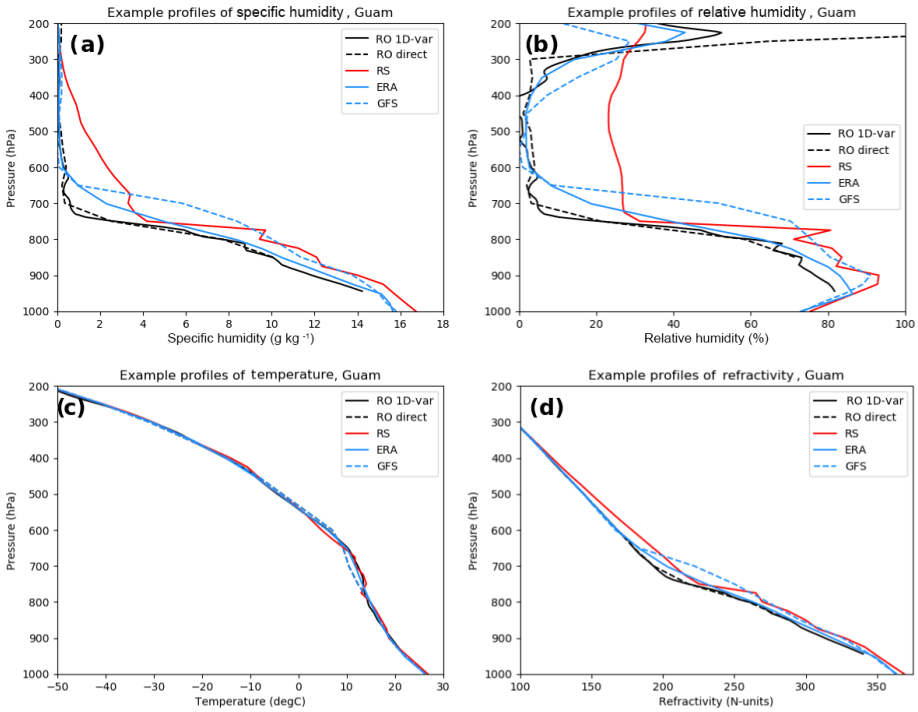

Figure 3. Profiles of specific humidity **(a)**, relative humidity **(b)**, temperature **(c)**, and refractivity **(d)** for the five data sets for 13 January 2007 at 00:23 UTC.

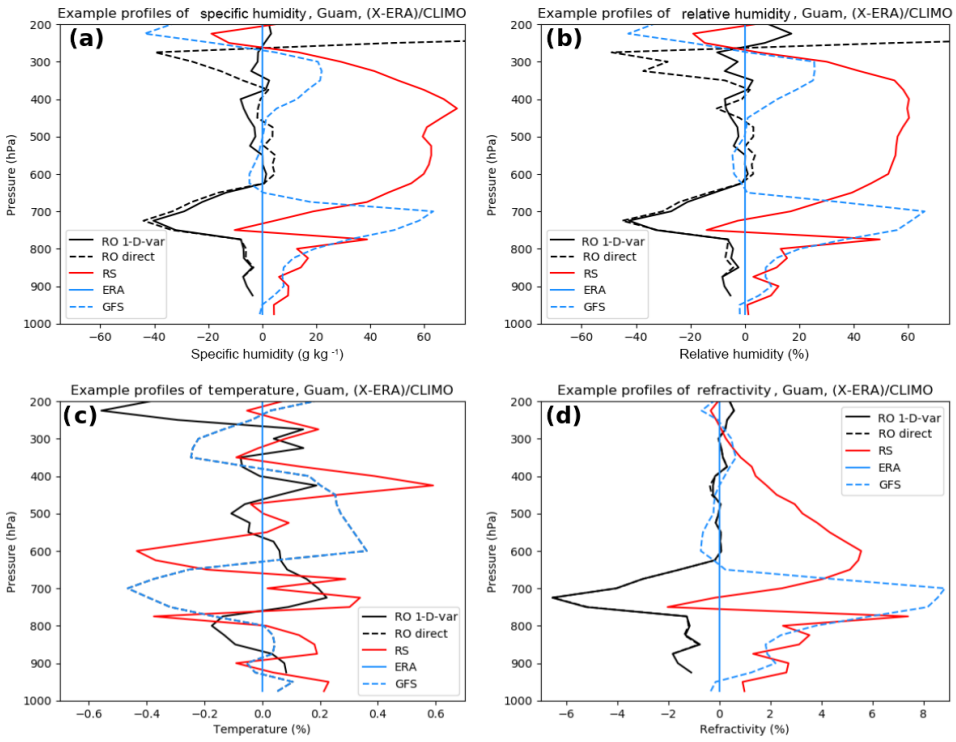

Figure 4. Same as Fig. 3 except for normalized differences from ERA.

The error variance of a variable X (e.g., q, RH, T, or N) is defined as

$$\mathrm{VAR_{err}}(X) = \frac{1}{n}\sum (X - \mathrm{true})^2 = \frac{1}{n}\sum X_{\mathrm{err}}^2, \quad (6)$$

where true is the true (but unknown) value of X and the summation is over n samples.

As shown in Appendix A, we can derive three different linearly independent equations for estimating the error variance of any data set, assuming that the error covariances among all the data sets are negligible compared to the differences in the observed mean square (MS) differences between the data sets. The three complete (and exact) linearly independent solutions for estimating the error variance of RO are

$$\begin{aligned}\mathrm{VAR_{err}\,(RO)} =& \frac{1}{2}\mathrm{MS\,(RO\text{–}ERA)} + \frac{1}{2}\mathrm{MS\,(RO\text{–}GFS)} \\ & -\frac{1}{2}\mathrm{MS\,(GFS\text{–}ERA)} + \mathrm{COV_{err}\,(RO, ERA)} \\ & +\mathrm{COV_{err}\,(RO, GFS)} - \mathrm{COV_{err}\,(GFS, ERA)}, \quad (7)\end{aligned}$$

$$\begin{aligned}\mathrm{VAR_{err}\,(RO)} =& \frac{1}{2}\mathrm{MS\,(RO\text{–}ERA)} + \frac{1}{2}\mathrm{MS\,(RO\text{–}RS)} \\ & -\frac{1}{2}\mathrm{MS\,(RS\text{–}ERA)} + \mathrm{COV_{err}\,(RO, ERA)} \\ & +\mathrm{COV_{err}\,(RO, RS)} - \mathrm{COV_{err}\,(RS, ERA)}, \quad (8)\end{aligned}$$

$$\begin{aligned}\mathrm{VAR_{err}\,(RO)} =& \frac{1}{2}\mathrm{MS\,(RO\text{–}GFS)} + \frac{1}{2}\mathrm{MS\,(RO\text{–}RS)} \\ & -\frac{1}{2}\mathrm{MS\,(RS\text{–}GFS)} + \mathrm{COV_{err}\,(RO, GFS)} \\ & +\mathrm{COV_{err}\,(RO, RS)} - \mathrm{COV_{err}\,(RS, GFS)}, \quad (9)\end{aligned}$$

where RO (or ERA, GFS, RS) corresponds to the value of X as estimated by RO (or ERA, GFS, RS) and MS denotes the mean square difference between the values from two data sets (e.g., RO–ERA).

We use Eqs. (7)–(9) to provide three independent estimates of $\mathrm{VAR_{err}}$(RO) by neglecting the $\mathrm{COV_{err}}$ terms in each equation. The assumption that the error covariances are small compared to the difference in variances between the data sets is similar to the assumption used in the apparent-error method that the errors of the observations and model forecasts are uncorrelated. In general the $\mathrm{COV_{err}}$ terms are not zero; thus we will examine the validity of this assumption by checking whether the various estimates of the error variances from the three equations are consistent with each other and reasonable compared to other independent studies that estimate error variances in other ways. In a related paper (Rieckh and Anthes, 2018) we examine the effect of various degrees of error correlations between two of the three data sets using simulated data sets with known errors.

The same procedure can be used to derive three equations for estimating the error variances for the other three data sets, RS, ERA, and GFS (equations not shown here).

So for each of the five data sets – RO-direct and RO 1D-VAR, RS, ERA, and GFS – there are three independent ways to estimate their respective error variances. This is the three-cornered hat method described in Appendix A. We note that it is possible that the estimated error variances from any of the three equations are negative because of the neglect of the $\mathrm{COV_{err}}$ terms and the small sample size, especially above 300 hPa for the Japanese stations and below 800 hPa for all four stations (Fig. 1).

4 Comparison with previous studies for RO refractivity

We first compute the estimated error variance for RO refractivity using GFS and ERA data for comparison with the Kuo et al. (2004) and Chen et al. (2011) estimates of RO error variance to illustrate the 3CH method. In an analogy to the apparent-error equation (Eq. 4), with RO being the observation and ERA being the forecast,

$$\mathrm{MS\,(RO\text{–}ERA)} = \mathrm{VAR_{err}\,(RO)} + \mathrm{VAR_{err}\,(ERA)}, \quad (10)$$

which is Eq. (A2) in Appendix A with neglect of the $\mathrm{COV_{err}}$ terms. We compute MS(RO–ERA) from the RO and ERA data sets (analogous to the apparent error variance σ_a^2 in Eq. 4) and plot its square root as the black line in Fig. 5. Then we estimate $\mathrm{VAR_{err}}$(RO) using Eq. (7) and the data sets (RO–GFS) and (GFS–ERA), neglecting the $\mathrm{COV_{err}}$ terms.

The square root of $\mathrm{VAR_{err}}$(RO) gives the standard deviation (SD) (Fig. 5, blue curve). Finally, the ERA error variance (analogous to the forecast error) is obtained by subtracting $\mathrm{VAR_{err}}$(RO) from MS(RO–ERA) using Eq. (10) above (pink line in Fig. 5). The gap in the computed ERA error SD in Fig. 5a occurs due to negative estimated error variance values, which can result from having a limited sample size, neglecting the error covariance terms, and having an error variance that is already close to zero (as is the case for ERA).

The results shown in Fig. 5 are quite similar to those from Kuo et al. (2004, Fig. 13) and Chen et al. (2011, Fig. 3d), who used different models and different data sets. The SD of normalized RO refractivity errors is a maximum of between 2.0 and 2.5 % near the surface, decreasing to about 0.5 % at 10 km. These similarities give credibility to both methods.

5 Calculation of the error variance terms using multiple data sets

This section shows the estimated error variances for N, q, T, and RH at one of the four stations (Mina) for the five data sets and summarizes the results for the other three stations (Naze, Ishi, and Guam).

5.1 Results for Mina

The following plots show the estimated error variances computed from Eqs. (7), (8), or (9). Two RO data sets (direct and 1D-VAR) are considered one at a time using the other three data sets. Thus we have two sets of error estimates for each

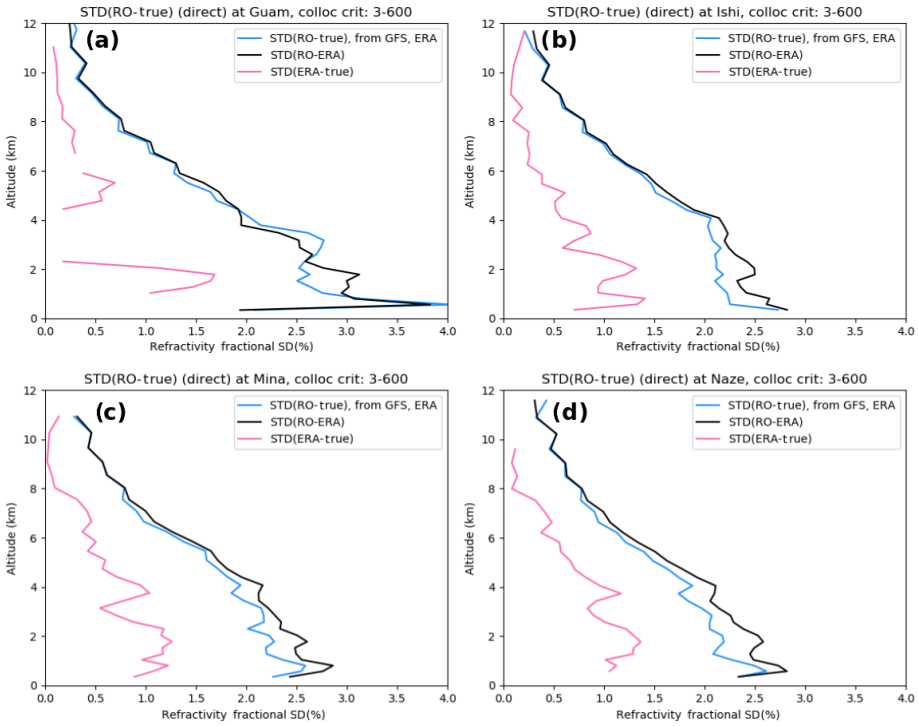

Figure 5. Standard deviations of the apparent-error SD(RO–ERA) (black line), estimated RO error SD(RO–true) computed from Eq. (7) (blue line) and ERA error SD(ERA–true) (pink line) for refractivity at **(a)** Guam, **(b)** Ishi, **(c)** Mina, and **(d)** Naze.

data set: one using the RO-direct with RS, ERA, and GFS, and one using the RO 1D-VAR with RS, ERA, and GFS. In the following plots, darker colors correspond to the three results using the RO 1D-VAR, and lighter colors correspond to the three results using the RO-direct.

Figure 6 shows the results for specific humidity. Error variances are shown rather than SDs because they are easier to interpret using the three equations used to derive them and because the SD are undefined for the occasional negative estimated error variance. Figure 6a shows the q error variance profiles for the two RO data sets (direct and 1D-VAR). The direct method (use of GFS temperature in Eq. 5) shows a steady increase of error variance with height, from about $100\,\%^2$ (SD $\sim 10\,\%$) at 950 hPa to $800\,\%^2$ (SD $\sim 28\,\%$) at 500 hPa and $2000\,\%^2$ (SD $\sim 45\,\%$) at 300 hPa. This is expected since the refractivity contains little information on water vapor above about 400 hPa and we are using an independent estimate of temperature, with no constraints on the water vapor retrieval. The q error variance profile for RO using the 1D-VAR method is similar to that of the direct method below 500 hPa but reaches a maximum at about 500 hPa of about $500\,\%^2$ (SD $\sim 22\,\%$) and then decreases toward zero at 200 hPa. The 1D-VAR method uses the ERA-Interim fields as a background and thus constrains the water vapor profile retrieval at high altitudes. It is notable that the three equations used to estimate the error variance profiles agree closely and the difference among the three estimates is much smaller than the differences in the mean profiles using the two RO retrieval methods.

The RS specific humidity error variance profiles at Mina (Fig. 6b) show a similar behavior to the RO-direct, with a steady increase with height, exceeding $2000\,\%^2$ (SD of $\sim 45\,\%$) at 400 hPa. The SDs of the RS are slightly larger than the two RO estimates below 600 hPa. The larger error variance of RS compared to RO is consistent with the results from Kuo et al. (2004) and is due in part to the RS representativeness differences. The error variance estimates using the RO-direct (orange) and RO 1D-VAR (red) are similar.

The error variance profiles from the two model sets (Fig. 6c, d) are quite different. The GFS error variance is less than the RO-direct and RS error variances at all levels, and also less than the RO 1D-VAR error variance except above 300 hPa. Although there is more scatter, especially in the upper troposphere, the ERA profiles are different from all the other data sets in that they show only a small increase of error variance with height, from near zero at the surface to up to a mean of about $100\,\%^2$ (SD $\sim 10\,\%$) at 200 hPa.

Figure 7 shows the estimated error variances of relative humidity. As with specific humidity, there is consistency among the estimates for the different data sets. The general behavior of the RH error variance profiles is similar to that for q, as might be expected because the percentage variability of water vapor is greater than that of temperature at this subtropical location. Again, the estimated error variances of the

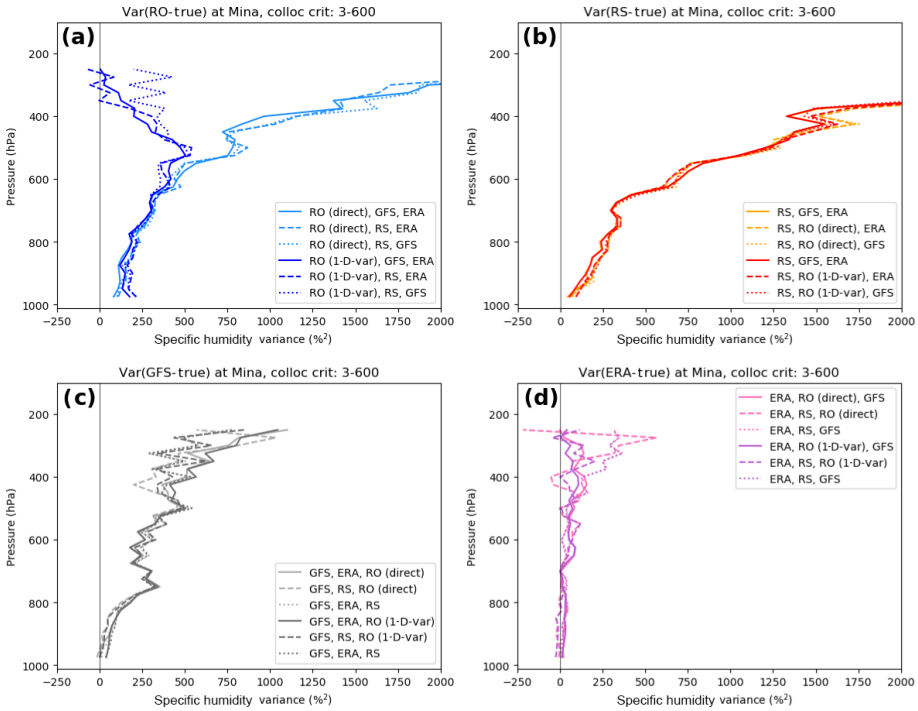

Figure 6. Estimated error variances (percent squared) of specific humidity at Mina: **(a)** RO, **(b)** RS, **(c)** GFS, and **(d)** ERA.

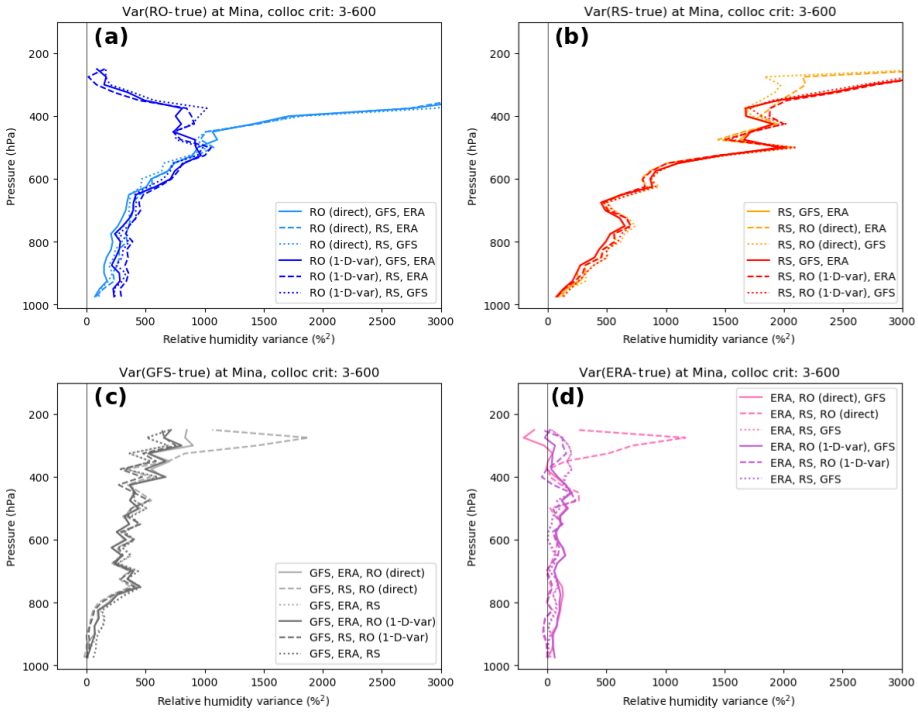

Figure 7. Estimated error variances (percent squared) of relative humidity at Mina: **(a)** RO, **(b)** RS, **(c)** GFS, and **(d)** ERA.

RO-derived RH are less than those of the RS in the lower troposphere. The GFS error variances are smaller than the RO and RS variances, except for the RO 1D-VAR profile above 300 hPa, which is constrained by the ERA observations in the upper troposphere. The ERA error variances are significantly smaller than the other data sets, averaging between 50 and 200 $\%^2$ (SD 7–14 %) throughout the troposphere.

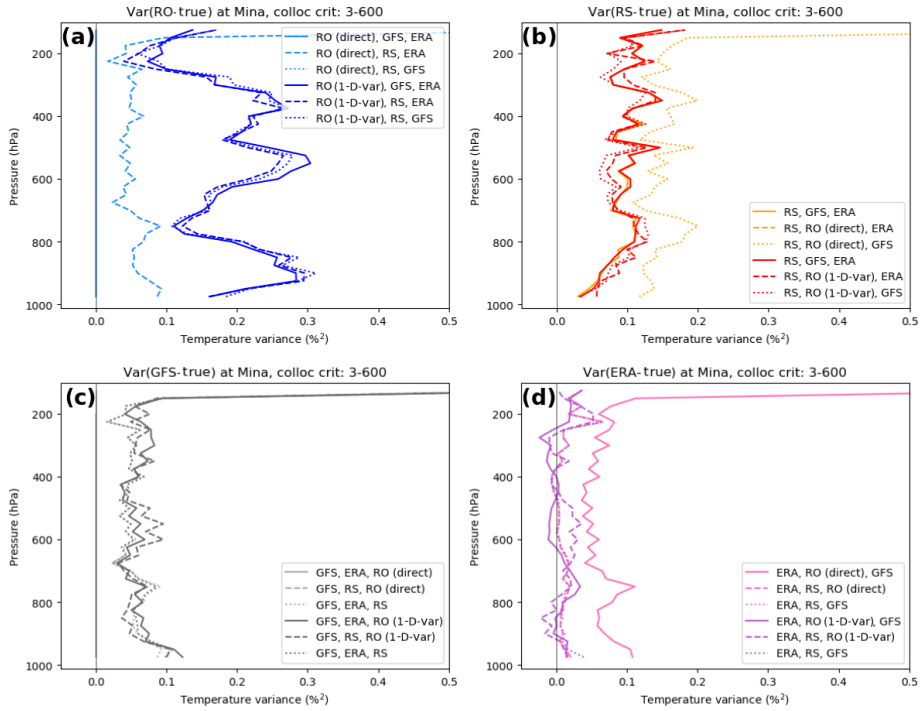

Figure 8. Estimated error variances (percent squared) of temperature at Mina: **(a)** RO, **(b)** RS, **(c)** GFS, and **(d)** ERA.

Figure 8 shows the estimated error variances of temperature. Because the RO-direct retrieval uses the exact GFS temperature, the results for the direct retrieval (light blue) using (RO, GFS, and ERA) and (RO, RS, and GFS) are not meaningful in Fig. 8a (they are identically zero). The result from Eq. (8) (RO, ERA, and RS), given by the dashed light blue line in Fig. 8a is valid, but in reality this is an estimate of the GFS T error variance, and it is in fact very similar to the profiles in Fig. 8c.

The RO 1D-VAR results for temperature from all three equations give somewhat larger results (Fig. 8, dark blue profiles). The estimated error variance profiles oscillate between 0.1 and 0.3 $\%^2$ (SD 0.3 to 0.55 %). For a temperature of 300 K, these correspond to 0.9 to 1.65 K.

The RS temperature error variances (Fig. 8b) vary between 0.05 and 0.15 $\%^2$ (SD 0.2 to 0.4 % or 0.6 to 1.2 K for $T = 300$ K). The GFS temperature error variances are a little lower, averaging around 0.05 to 0.10 $\%^2$ (SD 0.2 to 0.3 %), while the ERA-estimated temperature error variances average close to zero (Fig. 8d).

Figure 9 shows the estimates of the normalized refractivity errors for the five data sets. There is more spread in the refractivity estimates compared to those of the other variables, especially in the lower troposphere, where the estimates vary between about 4 and 9 $\%^2$ (SD 2 to 3 %) for the two RO variances. Recall that the RO-direct N are the observed RO N as provided by CDAAC, while the RO 1D-VAR N are modified based on the background (ERA) N. The average of the N error variances for the radiosondes (Fig. 9b) shows a maximum of $\sim 10\,\%^2$ (SD ~ 3.2 %) around 900 hPa. The GFS error variance profiles show a maximum around 750 hPa of $\sim 8\,\%^2$ (SD ~ 2.8 %). The ERA profiles show the smallest errors, with a maximum in the lower troposphere of an average of $\sim 2\,\%^2$ (SD ~ 1.4 %). All data sets show a decrease of error variance to less than 0.5 $\%^2$ (SD < 0.7 %) at 400 hPa. The reason for the large scatter in estimates of N below about 800 hPa may be related to errors in N caused by super-refraction in the lower troposphere, which occurs often in the tropics and subtropics. Super-refraction causes a negative N bias, which may lead to larger error covariances in this layer. The smaller number of RO samples below 800 hPa (Fig. 1) may also be a factor.

Figure 10 shows the mean of the three estimates of the error variances of the five data sets for q, RH, T, and N at Mina. The standard deviation[1] about these means is shown by the shaded areas. These figures show clearly the significant differences among the error variance estimates of the five data sets. In Fig. 10a, the error variance for specific humidity is greatest for the radiosonde (red and orange profiles) and least for the ERA profiles. As discussed earlier, the mean of the RO 1D-VAR retrieval reaches a maximum at about 550 hPa and then decreases back toward zero as it becomes constrained by the background profile at high levels. Figure 10b–d show the mean profiles of error variance for relative humidity, temperature, and refractivity. The rela-

[1] $\sigma = \left(\frac{1}{2}\sum_{n=1}^{n=3}(x_n - \overline{x})^2\right)^{1/2}$, where x_n denote the three error variance estimates.

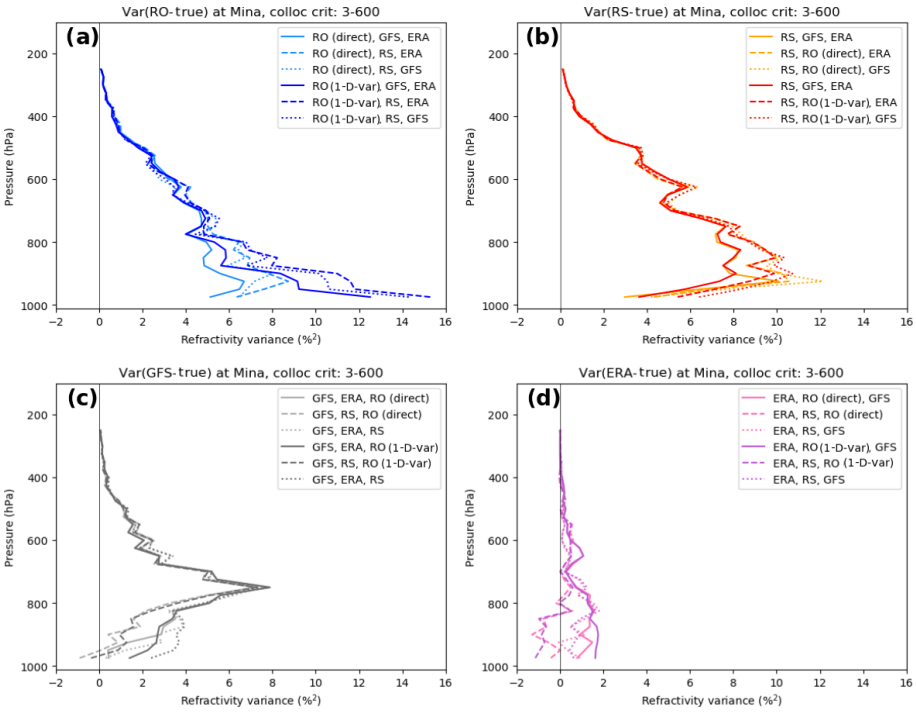

Figure 9. Estimated error variances (percent squared) of refractivity at Mina: **(a)** RO, **(b)** RS, **(c)** GFS, and **(d)** ERA.

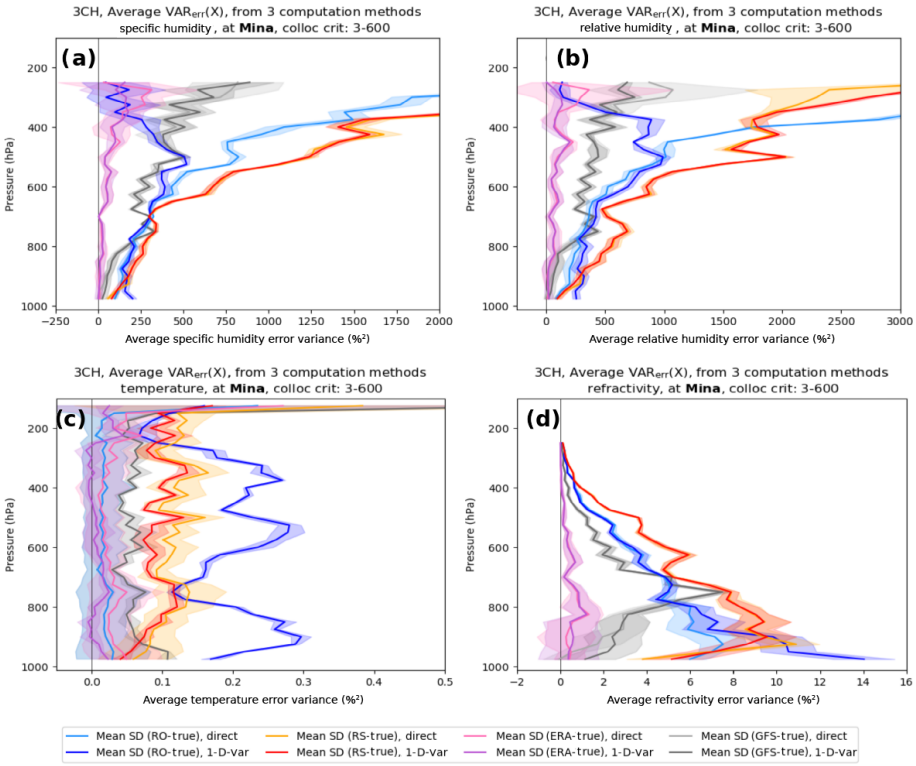

Figure 10. Mean of the three estimates of error variance plots for q, RH, T, and N using RO-direct and RO 1D-VAR for each data set at Mina. The standard deviation about the mean is indicated by shaded areas. **(a)** specific humidity, **(b)** relative humidity, **(c)** temperature, and **(d)** refractivity. RO (blue), radiosonde (red), GFS (gray), and ERA (purple).

tive humidity profiles are similar to the specific humidity profiles. The ERA errors are the smallest, followed by GFS, the RO, and finally the radiosondes. The temperature error variance profiles show that the ERA errors are very close to zero throughout the entire troposphere. The GFS profiles (gray) and the RS profiles (red and orange) show relatively constant values with height of approximately 0.05 and 0.1 $\%^2$, respectively (corresponding to temperature errors of 0.7 and 0.9 K at 300 K, respectively). The RO shows an oscillating error variance profile ranging between 0.1 and 0.3 $\%^2$ (0.9 and 1.6 K at 300 K). Finally, the refractivity profiles show the greatest variability, but the mean profiles are still quite distinct. ERA again shows the lowest errors, followed by GFS, RO, and RS.

It is difficult to find previous results for RS temperature and specific humidity error variances. However, previous studies comparing RO with RS and models indicate that our estimates are reasonable and consistent with these studies. Ho et al. (2017) found SD between RO and RS pairs for many RS types of about 1.5 K in the 200–20 hPa layer, where RO temperatures are most accurate (Table 2 in Ho et al., 2017). This value corresponds to the apparent error between RS and RO, which is larger than the RS error. The estimated RS temperature error variances from 200 to 100 hPa in Fig. 10c is about 0.15 $\%^2$, which corresponds to a SD of 0.39 % or 0.9 K for a mean temperature of 230 K. Ladstädter et al. (2015) compared high-quality GCOS (Global Climate Observing System) Reference Upper-Air Network (GRUAN) RS to RO globally and for a tropical station (Nauru) and subtropical station (Tateno, Japan) from 2002 to 2013. They found temperature SD of about 0.5 K for Nauru and 0.5 to 0.8 K at Tateno averaged over the layer 800 to 300 hPa. For specific humidity, they found SD between RO and RS of about 10 %, increasing to about 40 % in the upper troposphere. In our calculations for Guam and the three subtropical Japanese stations our estimates for SD of q are similar (Fig. 10a; Fig. B1 in Appendix B), ranging from about 10 % at 900 hPa to 45 % at 300 hPa.

Ho et al. (2010) compared COSMIC RO observations to ECMWF analyses and several types of radiosondes for the period August–November 2006. They found mean specific humidity SD of RO–ECMWF of $\sim 0.5\,\mathrm{g\,kg^{-1}}$ and RO–RS (Meisei) of $\sim 0.9\,\mathrm{g\,kg^{-1}}$. From their plots of the vertical profiles of the SD, these numbers are typical for the layer 800–500 hPa, which, given the normalization values from the four RS stations in our study (Fig. 3) of about $9\,\mathrm{g\,kg^{-1}}$ at 800 hPa and $2\,\mathrm{g\,kg^{-1}}$ at 500 hPa, correspond to SD (VAR) values of ~ 6 % (36 $\%^2$) at 800 hPa and 25 % (625 $\%^2$) at 500 hPa for ECMWF and ~ 10 % (100 $\%^2$) at 800 hPa and 45 % (2025 $\%^2$) at 500 hPa for Meisei RS. These values are similar to the estimates of the RS analysis for the Japanese stations shown in Fig. B1 of Appendix B.

Vergados et al. (2014) compared RO-derived observations of specific humidity with radiosondes and ERA-Interim under cloudy conditions in the tropics for August–October 2006. They used the direct method for computing specific humidity from the RO refractivity using the ERA-Interim temperatures. Their differences between zonal means of normalized RO and ERA-Interim observations of q are presented in Table 1 (we computed the normalized differences from their data in Table 3 for the tropics).

Table 1. Normalized differences of zonal mean RO and ERA specific humidity in the tropics for cloudy conditions (computed from data in Vergados et al., 2014).

Pressure (hPa)	VAR ($\%^2$)	SD (%)
925	320	17.8
850	460	21.4
700	1260	35.5
500	2760	53.5
400	4220	65.0
300	5625	75.0

The VAR values in Table 1 correspond to apparent errors, where RO and ERA correspond to the observation and forecast variables, respectively (Eq. 10). As expected, they are larger than the estimated error variances for RO-direct shown in Fig. 6a because the apparent errors are always larger than the observation errors as shown in Eq. (4). This comparison indicates that the estimates of true errors in Fig. 6a are reasonable.

5.2 Summary of results at Naze, Ishi, and Guam

The mean and SD error profiles for Naze, Ishi, and Guam corresponding to the above results for Mina are presented in Appendix B. Here we summarize the main similarities and differences between the error variance estimates for these stations compared to those for Mina. In general, we find similar magnitudes and shapes of the profiles of the estimated error variances of the five data sets for all four variables (q, RH, T, and N).

The estimated error profiles are especially similar for the three Japanese stations. This close similarity may be due primarily to the fact that the three locations are relatively close together and two of the three use the same type of radiosonde (Meisei).

The results from Guam are also similar in general magnitudes and shapes of the profiles to those from the three Japanese stations, but there are somewhat greater differences in some of the profiles (e.g., GFS q, RH, and N; and RS N). These differences are likely due to the different location and the use of a different radiosonde type at Guam (VIZ/Sippican B2). The neglected error covariance terms are also likely different between the three Japanese stations, which are located in a data-rich region, and Guam, which is located in a data-sparse region. Thus the model errors are less likely to be highly correlated with a single observational sys-

tem in the former than in the latter, where single observations may affect the models more significantly.

6 Summary and discussion

We used the three-cornered hat (3CH) method to estimate vertical profiles of error variances of different observation and model data sets by computing the differences among the data sets. We computed estimated error variances of four variables (specific humidity q, relative humidity RH, temperature T, and refractivity N) for five data sets (ERA, GFS, radiosondes (RS), and radio occultation (RO) 1D-VAR and RO-direct) at four different locations in the tropics and subtropics for the year 2007. The stations are Guam, Ishigakijima, Minamidaitōjima, and Naze. The latter three stations are on Japanese islands and are located quite close together (a few hundred kilometers apart). We computed vertical profiles of estimated error variances for normalized differences from the 2007 ERA mean values of q, RH, T, and N at the four stations using three linearly independent equations (Eqs. 7–9) neglecting all error covariance terms. Ideally, with a very large sample of data pairs and zero correlation of errors among the different data sets, all three equations would produce identical results. However, a finite data set and nonzero error correlations among the data sets lead to three different estimates, as shown by Rieckh and Anthes (2018). The differences among the three estimates is a measure of these effects.

Although the neglect of the covariance terms affects the results to a noticeable degree in some of the estimated profiles, there is strong evidence that there is valid information in the estimated error profiles that rises above the noise caused by the neglect of the covariance terms and the limited data sample. This evidence is summarized as follows:

1. There is generally good agreement in the three estimated error profiles of the four variables for each of the five data sets at all four locations. It is unlikely that this agreement would occur by chance if the neglected error covariance terms were large enough to invalidate the results, because they would have to somehow combine or cancel in each of the three equations to give the observed similar results.

2. There are large differences in the overall structure (shape and magnitude) of the average vertical profiles of estimated error variances for the five data sets (Fig. 10). These differences are significantly larger than the standard deviation from the three independent equations used to compute the error variances.

3. The variability, or spread among the error estimates, is similar at most height levels for specific humidity, relative humidity, and temperature. If the error covariance terms were significant, they would almost certainly vary with height, giving different agreement in estimated error profiles with height. For example, we know that RO temperature and refractivity are most accurate in the upper troposphere and least accurate in the lower troposphere and that the weight given to RO in the models' data assimilation varies significantly with height, being largest in the upper troposphere and smallest in the lower troposphere. Thus one would expect the RO–ERA and RO–GFS error covariance terms to vary significantly with height. Also, the RS errors as well as the ERA and GFS model errors vary with height. It is therefore unlikely that all of the neglected error covariance terms are the same at all heights.

4. The general structure and magnitudes of the estimated error variance profiles are similar at the four locations. However, there are some small differences among the profiles at the four locations. In general, the differences among the three estimates (indicated by the SD about the mean), which are a measure of the effect of the neglected covariance terms as well as limited sample size, are smallest for Ishi, Naze, and Mina and largest for Guam. Since the three Japanese stations are close together, this suggests that there is a difference in the error variance of the Japanese RS observations compared to the Guam RS observations. There may also be small differences in the model errors over the Japanese stations, which are located in a data-rich area compared to Guam, which is located in a data-sparse region. The largest variability and largest error estimates occur at Guam, which uses a radiosonde that is thought to have large water vapor biases due to sensor malfunctions (Holger Vömel, personal communication, 2017).

5. The magnitudes of the estimated RO refractivity error variances are supported by previously published studies, including Kuo et al. (2004) and Chen et al. (2011).

6. The estimated errors are smallest for the ERA-Interim model data set, which is a reasonable result since ERA uses an excellent model and data assimilation system that assimilates many independent, quality-checked observations. In fact, Vergados et al. (2015) state that "ERA-Interim is one of the most advanced global atmospheric models simulating the state of the atmosphere with accuracy similar to what is theoretically possible (Simmons and Hollingsworth, 2002) using a 4D-VAR method (Simmons et al., 2005)".

7. Our results show, in general, that the RO observations have smaller errors than the radiosonde errors, in agreement with previous studies. This difference is in part due to representativeness errors associated with the RS, which are point measurements while the other data sets are representative of horizontal averages with a length scale of ~ 100 km.

Code availability. Code will be made available by the author upon request.

Data availability. Data can be made available from authors upon request.

Appendix A: Derivation of estimates of error variances using four data sets and the three-cornered hat method

A1 Description of three-cornered hat method

In this appendix we summarize the 3CH method (Gray and Allan, 1974) for estimating error variances from three data sets. Gray and Allan (1974) developed the method to estimate the absolute frequency stability of an ensemble of N clocks by forming all $(N-1)(N-2)/2$ triads under the assumption that the clock errors are uncorrelated. Each of the triads are three-cornered hat (3CH) estimates. Riley (2003) provides a summary of the 3CH method.

Variations and enhancements of the 3CH method have been applied to many diverse geophysical data sets. The 3CH method has been used to estimate the stability of GNSS clocks using the measured frequencies from multiple clocks (Ekstrom and Koppang, 2006; Griggs et al., 2014, 2015; Luna et al., 2017). Valty et al. (2013) used the 3CH method to estimate the geophysical load deformation computed from GRACE satellites, GPS vertical displacement measurements, and global general circulation models. O'Carroll et al. (2008) compared three types of systems to measure sea surface temperatures: two different radiometers and in situ observations from buoys. They discuss the assumption of the neglect of error correlations among the three data sets; the effect of representativeness errors; and the interpretation of "truth", the true value of the variable being measured.

Closely related to the 3CH method is the triple-collocation (TC) method, which was introduced by Stoffelen (1998) and has been widely used since in oceanography and hydrometeorology (e.g., Su et al., 2014; Gruber et al., 2016). It has been used to estimate the error variances of triplets of observation types to measure a diverse set of geophysical properties, including wave heights, sea surface temperatures, precipitation, surface winds over the ocean, leaf area index (LAI) products, and soil moisture. Stoffelen (1998) estimated the error variances of in situ measurements, ERS scatterometer winds, and NCEP forecast model wind speeds. Later, Vogelzang et al. (2011) compared four sets of scatterometer winds from ASCAT and SeaWinds with buoy measurements and ECMWF model forecasts of surface winds over the oceans to estimate the error variances and standard deviations of the different data sets and their combinations. Stoffelen (1998) and Vogelzang et al. (2011) calibrate their data sets using an error model and show how the error estimates may account for a partial correlation of representativeness errors between two data sets if independent information about this correlation is known. Fang et al. (2012) estimated the uncertainties in three different estimates of LAI products. McColl et al. (2014) extended the method by deriving a performance metric of the measurement system to the unknown truth and applied the extended method to wind estimates from numerical weather prediction, scatterometer, and buoy wind estimates. Roebeling et al. (2012) used the triple-collocation method to estimate the errors associated with three ways of estimating precipitation: the Spinning Enhanced Visible and Infrared Imager (SEVERI), weather radars, and ground-based precipitation rain gauges. They concluded that the method provides useful error estimates of these systems.

The major assumption in the 3CH and TC methods is that the unknown errors of the three systems are uncorrelated. Correlations between any or all of the three measurement systems will reduce the accuracy of the error estimates. Other factors that can reduce the accuracy of the error estimates include widely different errors associated with the three systems or a small sample size. These factors can lead to negative estimates of error variances, especially when the estimates are close to zero (Gray and Allan, 1974; Riley, 2003). All three of these factors potentially affect the 3CH estimates in this paper, but the general agreement of the three linearly independent equations for estimating the error variances of each variable suggests that the estimates are still reasonably valid and contain useful information.

A2 Derivation of 3CH equations

In this section we summarize the derivation of the 3CH method as applied to four meteorological data sets, RO, RS, GFS, and ERA. The error variance of a variable X (e.g., temperature, specific humidity, relative humidity, refractivity) is defined as

$$\mathrm{VAR_{err}}(X) = \frac{1}{n}\sum (X - \mathrm{true})^2 = \frac{1}{n}\sum X_{\mathrm{err}}^2, \tag{A1}$$

where true is the true but unknown value of X and the summation is over n samples. This definition of error variance includes bias as well as random errors in X. Let RO correspond to the value of X as estimated by RO, ERA correspond to the value of X as estimated by ERA, and similarly for GFS and RS. We then have

$$\mathrm{MS\,(RO–ERA)} = \mathrm{VAR_{err}\,(RO)} + \mathrm{VAR_{err}\,(ERA)} - 2\mathrm{COV_{err}\,(RO, ERA)}\,, \tag{A2}$$

where MS(RO–ERA) is the mean square difference between RO and ERA and the last term is the error covariance between RO and ERA.

In the estimation of the error variances for the four data sets, we assume that the RO errors and ERA errors are uncorrelated, so the error covariance term in Eq. (A2) is zero or, in practice, negligibly small compared to the other terms. However, to show the complete (and exact) equations, we retain them here in the six equations (Eqs. A2–A7) involving the different pairs of data sets.

$$\begin{aligned}\mathrm{MS\,(GFS–ERA)} =& \mathrm{VAR_{err}\,(GFS)} + \mathrm{VAR_{err}\,(ERA)} \\ & - 2\mathrm{COV_{err}\,(GFS, ERA)}\,, \end{aligned} \tag{A3}$$

$$\begin{aligned}\mathrm{MS\,(RS–ERA)} =& \mathrm{VAR_{err}\,(RS)} + \mathrm{VAR_{err}\,(ERA)} \\ & - 2\mathrm{COV_{err}\,(RS, ERA)}\,, \end{aligned} \tag{A4}$$

$$\begin{aligned}\mathrm{MS\,(RO–GFS)} =& \mathrm{VAR_{err}\,(RO)} + \mathrm{VAR_{err}\,(GFS)} \\ & - 2\mathrm{COV_{err}\,(RO, GFS)}\,, \end{aligned} \tag{A5}$$

$$\begin{aligned}\mathrm{MS\,(RS–GFS)} =& \mathrm{VAR_{err}\,(RS)} + \mathrm{VAR_{err}\,(GFS)} \\ & - 2\mathrm{COV_{err}\,(RS, GFS)}\,, \end{aligned} \tag{A6}$$

$$\begin{aligned}\mathrm{MS\,(RO–RS)} =& \mathrm{VAR_{err}\,(RO)} + \mathrm{VAR_{err}\,(RS)} \\ & - 2\mathrm{COV_{err}\,(RO, RS)}\,. \end{aligned} \tag{A7}$$

It is possible to use these six equations to get three different, linearly independent estimates of the four unknowns error variances for RO, RS, ERA, and GFS. For RO, these three equations are

$$\begin{aligned}\mathrm{VAR_{err}(RO)} =& \frac{1}{2}\mathrm{MS(RO-ERA)} + \frac{1}{2}\mathrm{MS(RO-GFS)} \\ & - \frac{1}{2}\mathrm{MS(GFS-ERA)} + \mathrm{COV_{err}(RO, ERA)} \\ & + \mathrm{COV_{err}(RO, GFS)} - \mathrm{COV_{err}(GFS, ERA)} \end{aligned} \tag{A8}$$

$$\begin{aligned}\mathrm{VAR_{err}(RO)} =& \frac{1}{2}\mathrm{MS(RO-ERA)} + \frac{1}{2}\mathrm{MS(RO-RS)} \\ & - \frac{1}{2}\mathrm{MS(RS-ERA)} + \mathrm{COV_{err}(RO, ERA)} \\ & + \mathrm{COV_{err}(RO, RS)} - \mathrm{COV_{err}(RS, ERA)} \end{aligned} \tag{A9}$$

$$\begin{aligned}\mathrm{VAR_{err}(RO)} =& \frac{1}{2}\mathrm{MS(RO-GFS)} + \frac{1}{2}\mathrm{MS(RO-RS)} \\ & - \frac{1}{2}\mathrm{MS(RS-GFS)} + \mathrm{COV_{err}(RO, GFS)} \\ & + \mathrm{COV_{err}(RO, RS)} - \mathrm{COV_{err}(RS, GFS)}. \end{aligned} \tag{A10}$$

O'Carroll et al. (2008) present these equations for a system of three observation types (their Eq. 1). However, they remove the mean biases from each data set in their definition of error variance, whereas we do not in our definition (Eq. A1). Our expressions for estimated error variances are identical to those of O'Carroll et al. (2008) with the removal of the effect of these biases; e.g., replace $\mathrm{MS}(X-Y)$ in Eqs. (A8)–(A10) with $\mathrm{MS}(X-Y) - [M(X-Y)]^2$, where X and Y are any of the data sets. Removing these biases will generally result in smaller estimated error variances than the results presented in this paper.

As noted by an anonymous reviewer, it is possible to derive infinitely many linearly dependent equations by combining Eqs. (A8)–(A10) in different ways by forming combinations of the form $M_1 \times$ Eq. (A8) $+ M_2 \times$ Eq. (A9) $+ M_3 \times$ Eq. (A10), where M_1, M_2, and M_3 are any numbers except those for which $M_1 + M_2 + M_3 = 0$. We did not pursue this possibility in this paper but instead used the three linearly independent equations only in our estimates of error variances.

If all the neglected $\mathrm{COV_{err}}$ terms were in fact identically zero and the sample size was very large (much larger than our sample size), all three estimates of the error variances would be the same. The fact that they give different solutions is because the neglected $\mathrm{COV_{err}}$ terms are in reality not zero, and hence their neglect affects the three approximate equations in different ways to give three different solutions. The relatively small sample size n also contributes to the differences in the three solutions, which are a measure of these effects.

We also note that the error estimates contain any representativeness errors caused by the different data sets representing different scales of atmospheric structure (O'Carroll et al., 2008). Representativeness errors can occur because of different horizontal or vertical resolutions or footprints of the data sets.

A3 Brief comparison of 3CH method and TC method

While it is not the intent of this paper to do a thorough comparison of the 3CH and TC methods, which are introduced above, in response to a reviewer's comment we compared the two methods on a subset of our data sets. A difference between the 3CH and TC method is that the TC method corrects for additive and multiplicative biases among the three data sets, as discussed by Stoffelen (1998), Vogelzang et al. (2011), and others. The TC method calibrates two of the data sets against the third, eliminating biases among the three data sets. This calibration uses an error model of the form $X_i = a \cdot \mathrm{true} + b + e_i$, where a and b stand for the "trend" and "bias" calibration coefficients and e_i are random errors (Vogelzang et al., 2011). As shown below, calibrating our data sets according to this model gave results very similar to results using our uncalibrated data sets.

In our application of the TC method we use the following combinations of data sets: (ERA, RO, RS), (ERA, RO, GFS), and (ERA, GFS, RS). For the RO we use two RO retrievals, the direct and 1D-VAR (see Sect. 2.3). The RO, RS, and GFS data sets are all calibrated using ERA as the calibration reference, using the following calibration factors. For example, the calibrated RO and RS (designated by $\mathrm{RO_{cal}}$ and $\mathrm{RS_{cal}}$, respectively) using ERA as the reference are (following Stoffelen, 1998; Vogelzang et al., 2011; and Roebeling et al., 2012)

$$\mathrm{RO_{cal}} = \frac{\mathrm{RO} - b_{\mathrm{RO}}}{a_{\mathrm{RO}}},$$

$$\mathrm{RS_{cal}} = \frac{\mathrm{RS} - b_{\mathrm{RS}}}{a_{\mathrm{RS}}},$$

where the additive bias terms are

$$b_{\mathrm{RO}} = M\,(\mathrm{RO–ERA})\,,$$

$$b_{\mathrm{RS}} = M\,(\mathrm{RS–ERA})\,,$$

the multiplicative bias terms are

$$a_{\mathrm{RO}} = \frac{M\,(\mathrm{RO \cdot RS})}{M\,(\mathrm{RS \cdot ERA})},$$

$$a_{\mathrm{RS}} = \frac{M\,(\mathrm{RO}\cdot\mathrm{RS})}{M\,(\mathrm{RO}\cdot\mathrm{ERA})},$$

and M denotes the mean value over the data sets.

The results of the specific humidity error variance estimates for $\mathrm{RO_{cal}}$ and $\mathrm{RS_{cal}}$ compared to RO and RS are shown in Fig. A1, and the estimates for $\mathrm{ERA_{cal}}$ and $\mathrm{GFS_{cal}}$ compared to ERA and GFS are shown in Fig. A2. The left panels show the results from the TC method (calibrated data), and the right panels show the results using the 3CH method (uncalibrated data). The close similarity of the results indicates that the biases do not significantly affect the 3CH estimates, in agreement with the results from the error model study in Rieckh and Anthes (2018).

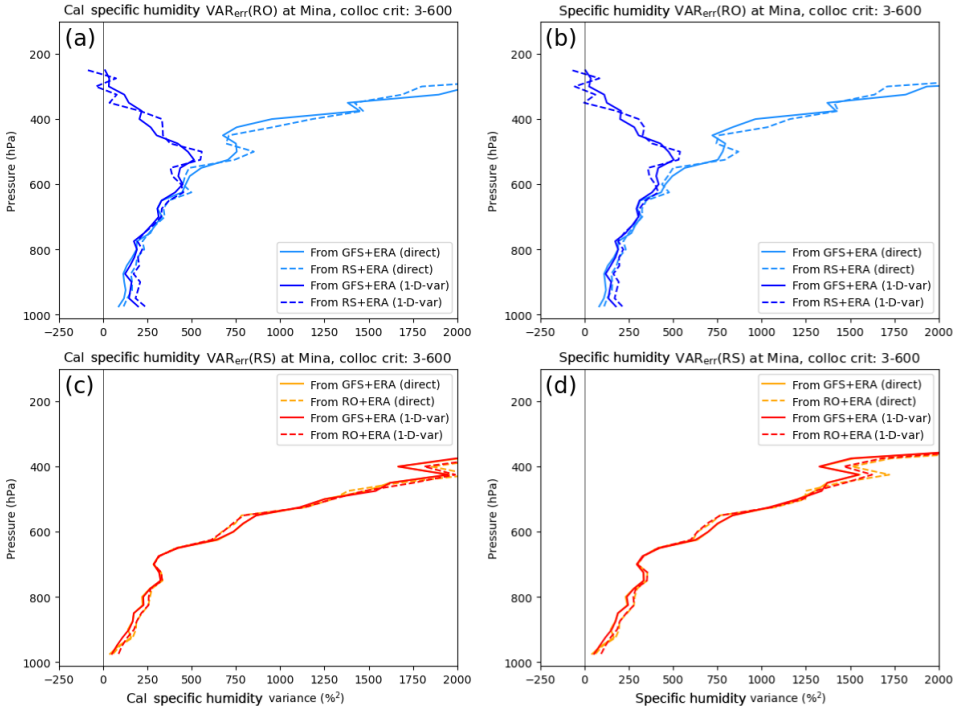

Figure A1. Estimated RO and RS error variances for specific humidity at Minamidaitōjima (Japan) using calibrated data as in the TC method **(a, c)** and the uncalibrated data as in the 3CH method **(b, d)**. For the TC method, the RO, RS, and GFS data sets are calibrated with respect to ERA as the reference data set. The following combinations of the four data sets are used: (ERA, RO, RS), (ERA, RO, GFS), and (ERA, GFS, RS).

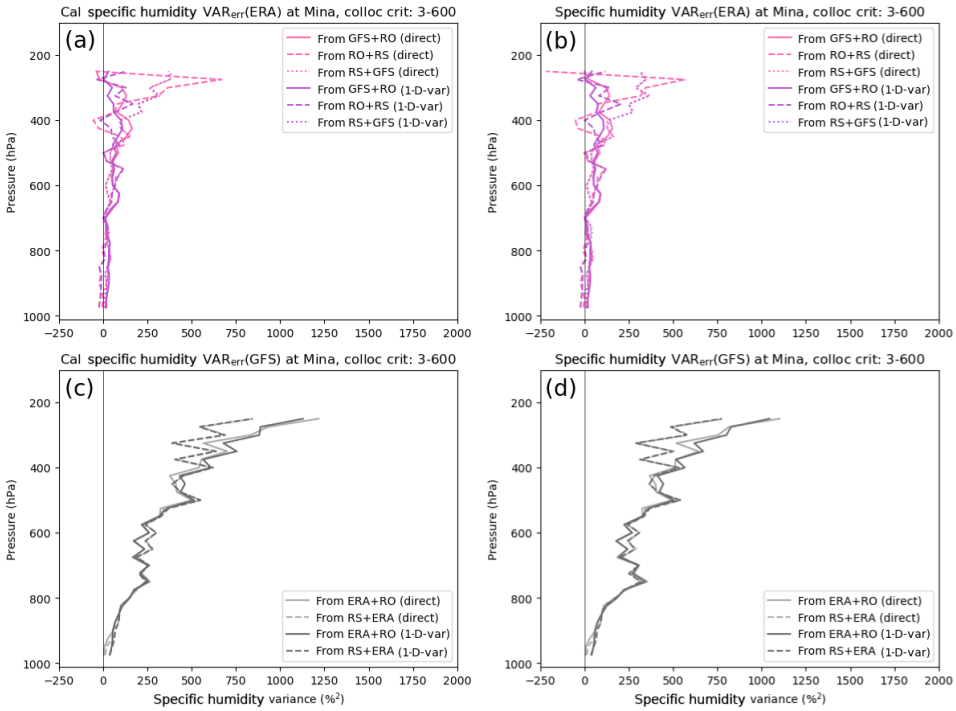

Figure A2. Estimated ERA and GFS specific error variances for ERA at Minamidaitōjima (Japan) using calibrated data as in the TC method **(a, c)** and the uncalibrated data as in 3CH method **(b, d)**. For the TC method, the RO, RS, and GFS data sets are calibrated with respect to ERA. The following combinations of the four data sets are used: (ERA, RO, RS), (ERA, RO, GFS), and (ERA, GFS, RS).

Appendix B: Mean and standard deviations of three independent error estimates of q, RH, T, and N using RO-direct and RO 1D-VAR at Guam, Ishi, Mina and Naze

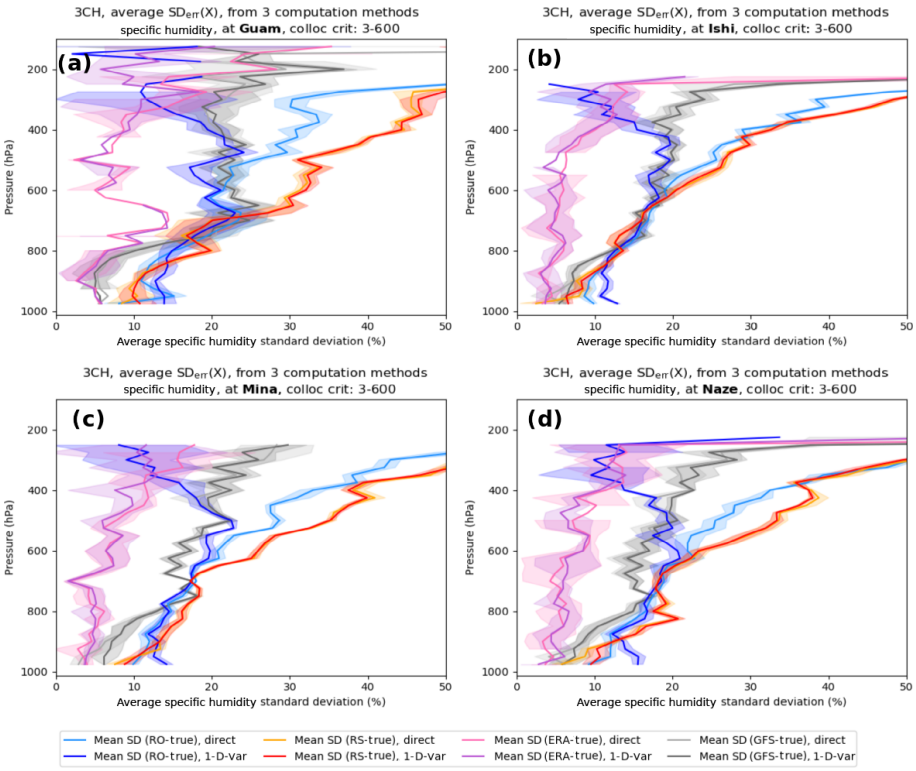

Figure B1. Mean and standard deviations (shading) of the three estimates of normalized specific humidity using RO-direct and RO 1D-VAR at **(a)** Guam, **(b)** Ishi, **(c)** Mina, and **(d)** Naze.

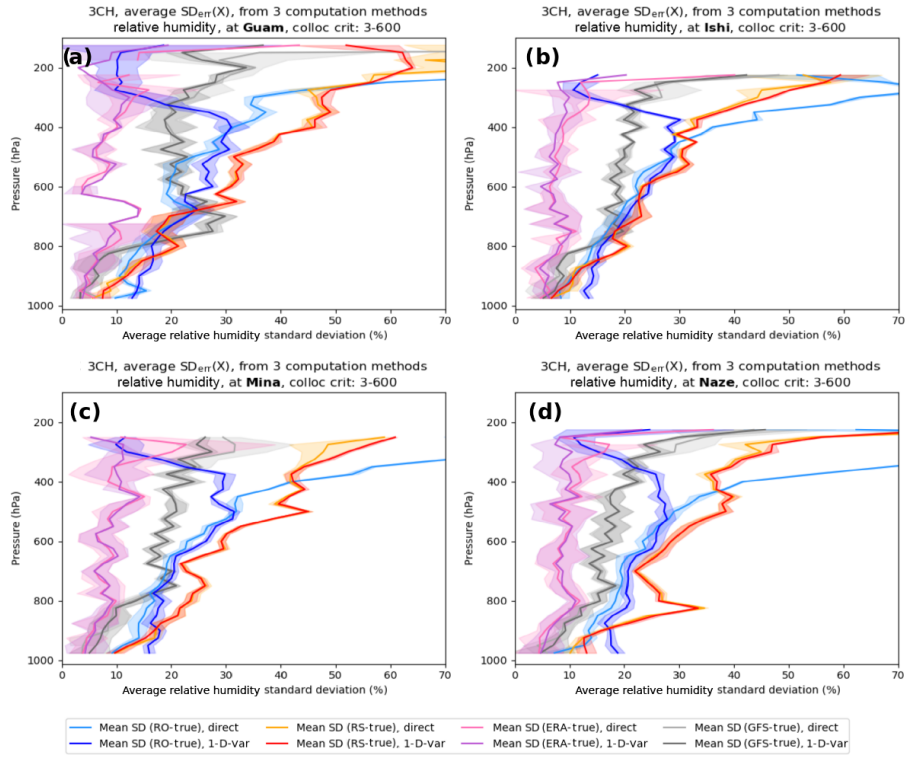

Figure B2. Mean and standard deviations (shading) of the three estimates of normalized relative humidity using RO-direct and RO 1D-VAR at **(a)** Guam, **(b)** Ishi, **(c)** Mina, and **(d)** Naze.

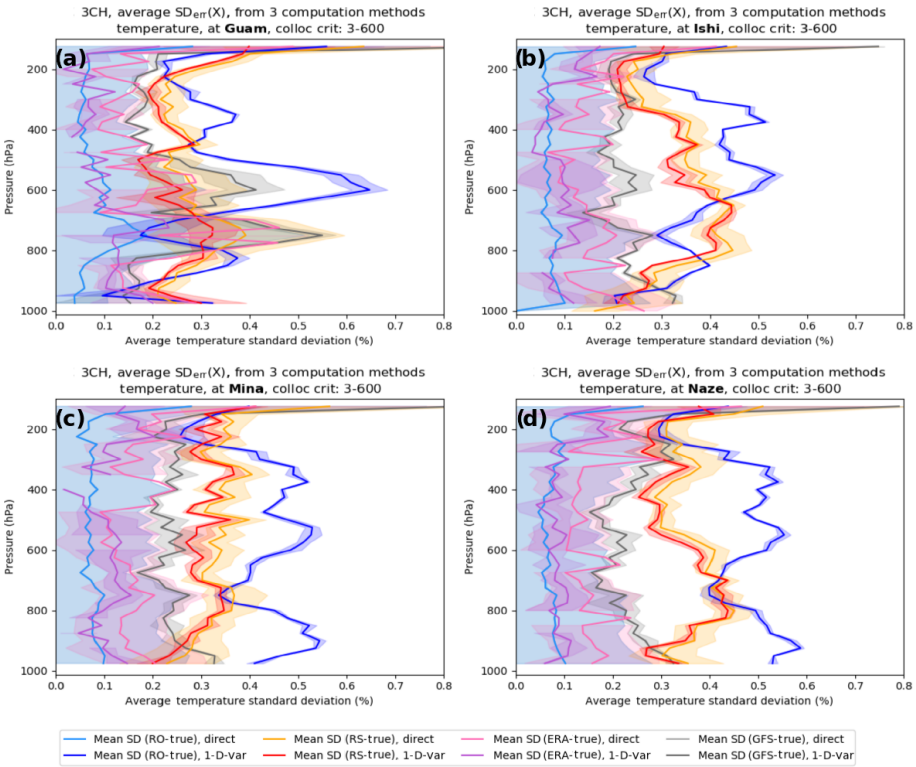

Figure B3. Mean and standard deviations (shading) of the three estimates of normalized temperature using RO-direct and RO 1D-VAR at **(a)** Guam, **(b)** Ishi, **(c)** Mina, and **(d)** Naze.

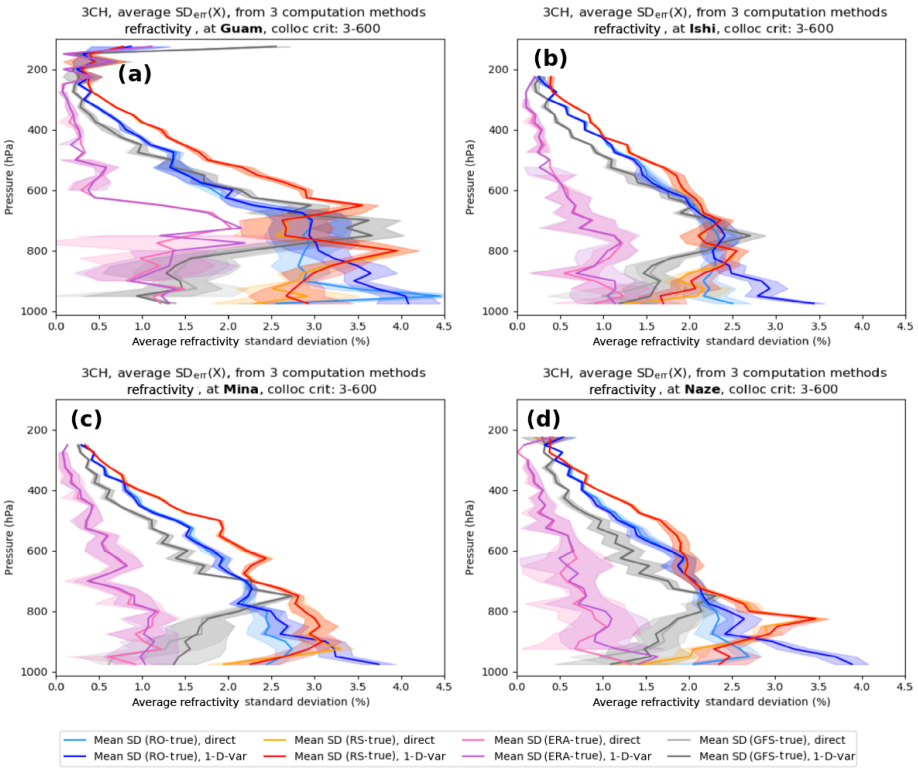

Figure B4. Mean and standard deviations (shading) of the three estimates of normalized refractivity using RO-direct and RO 1D-VAR at **(a)** Guam, **(b)** Ishi, **(c)** Mina, and **(d)** Naze.

Author contributions. RA formulated the overall idea of this work, and TR performed all the calculations and contributed significantly to the discussion of the results.

Competing interests. The authors declare that they have no conflict of interest.

Acknowledgements. We acknowledge with thanks the insightful comments and advice on this study from Ian Culverwell and John Eyre (Met Office), Shay Gilpin (UCAR COSMIC), Sean Healy (ECMWF), Adrian Simmons (ECMWF), and Sergey Sokolovskiy (UCAR COSMIC). We thank the three anonymous reviewers for their constructive comments. Anthes and Rieckh were supported by NSF-NASA grant AGS-1522830. We thank Eric DeWeaver (NSF) and Jack Kaye (NASA) for their long-term support of COSMIC.

Edited by: Ad Stoffelen
Reviewed by: three anonymous referees

References

Chen, S.-Y., Huang, C.-Y., Kuo, Y.-H., and Sokolovskiy, S.: Observational Error Estimation of FORMOSAT-3/COSMIC GPS Radio Occultation Data, Mon. Weather Rev., 139, 853–865, https://doi.org/10.1175/2010MWR3260.1, 2011.

Cucurull, L. and Derber, J. C.: Operational Implementation of COSMIC Observations into NCEP's Global Data Assimilation System, Weather Forecast., 23, 702–711, https://doi.org/10.1175/2008WAF2007070.1, 2008.

Dee, D. P., Uppala, S. M., Simmons, A. J., Berrisford, P., Poli, P., Kobayashi, S., Andrae, U., Balmaseda, M. A., Balsamo, G., Bauer, P., Bechtold, P., Beljaars, A. C. M., van de Berg, L., Bidlot, J., Bormann, N., Delsol, C., Dragani, R., Fuentes, M., Geer, A. J., Haimberger, L., Healy, S. B., Hersbach, H., Hólm, E. V., Isaksen, L., Kållberg, P., Köhler, M., Matricardi, M., McNally, A. P., Monge-Sanz, B. M., Morcrette, J.-J., Park, B.-K., Peubey, C., de Rosnay, P., Tavolato, C., Thépaut, J.-N., and Vitart, F.: The ERA-Interim reanalysis: configuration and performance of the data assimilation system, Q. J. Roy. Meteor. Soc., 137, 553–597, https://doi.org/10.1002/qj.828, 2011.

Desroziers, G. and Ivanov, S.: Diagnosing and adaptive tuning of observation-error parameters in a variational assimilation, Q. J. Roy. Meteor. Soc., 127, 1433–1452, https://doi.org/10.1002/qj.49712757417, 2001.

Ekstrom, C. R. and Koppang, P. A.: Error Bars for Three-Cornered Hats, IEEE T. Ultrason. Ferr., 53, 876–879, https://doi.org/10.1109/TUFFC.2006.1632679, 2006.

ERA-Interim, available at: https://www.ecmwf.int/en/research/climate-reanalysis/reanalysis-datasets/era-interim, last access: 1 July 2018.

Fang, H., Wei, S., Jiang, C., and Scipal, K.: Theoretical uncertainty analysis of global MODIS, CYCLOPES, and GLOBCARBON LAI products using a triple collocation method, Remote Sens. Environ., 124, 610–621, https://doi.org/10.1016/j.rse.2012.06.013, 2012.

Gilpin, S., Rieckh, T., and Anthes, R.: Reducing representativeness and sampling errors in radio occultation–radiosonde comparisons, Atmos. Meas. Tech., 11, 2567–2582, https://doi.org/10.5194/amt-11-2567-2018, 2018.

Gray, J. E. and Allan, D. W.: A method for estimating the frequency stability of an individual oscillator, in: 28th Annual Symposium on Frequency Control, Atlantic City, New Jersey, 29–31 May 1974, IEEE, 243–246, https://doi.org/10.1109/FREQ.1974.200027, 1974.

Griggs, E., Kursinski, E., and Akos, D.: An investigation of GNSS atomic clock behaviour at short time intervals, GPS Solut., 18, 443–452, https://doi.org/10.1007/s10291-013-0343-7, 2014.

Griggs, E., Kursinski, E., and Akos, D.: Short-term GNSS satellite clock stability, Radio Sci., 50, 813–826, https://doi.org/10.1002/2015RS005667, 2015.

Gruber, A., Su, C.-H., Zwieback, S., Crow, W., Dorigo, W., and Wagner, W.: Recent advances in (soil moisture) triple collocation analysis, Int. J. Appl. Earth Obs., 45, 200–211, https://doi.org/10.1016/j.jag.2015.09.002, 2016.

Ho, S.-P., Zhou, X., Kuo, Y.-H., Hunt, D., and Wang, J.-H.: Global evaluation of radiosonde water vapor systematic biases using GPS radio occultation from COSMIC and ECMWF analysis, Remote Sens., 2, 1320–1330, https://doi.org/10.3390/RS2051320, 2010.

Ho, S.-P., Peng, L., and Vömel, H.: Characterization of the long-term radiosonde temperature biases in the upper troposphere and lower stratosphere using COSMIC and Metop-A/GRAS data from 2006 to 2014, Atmos. Chem. Phys., 17, 4493-4511, https://doi.org/10.5194/acp-17-4493-2017, 2017.

Hollingsworth, A. and Lönnberg, P.: The statistical structure of short-range forecast errors as determined from radiosonde data. Part I: The wind field, Tellus A, 38, 111–136, https://doi.org/10.3402/tellusa.v38i2.11707, 1986.

Kitchen, M.: Representativeness errors for radiosonde observations, Q. J. Roy. Meteor. Soc., 115, 673–700, https://doi.org/10.1002/qj.49711548713, 1989.

Kleist, D. T., Parrish, D. F., Derber, J. C., Treadon, R., Wu, W.-S., and Lord, S.: Introduction of the GSI into the NCEP Global Data Assimilation System, Weather Forecast., 24, 1691–1705, https://doi.org/10.1175/2009WAF2222201.1, 2009.

Kuo, Y.-H., Wee, T.-K., Sokolovskiy, S., Rocken, C., Schreiner, W., Hunt, D., and Anthes, R. A.: Inversion and error estimation of GPS radio occultation data, J. Meteorol. Soc. Jpn., 82, 507–531, 2004.

Ladstädter, F., Steiner, A. K., Schwärz, M., and Kirchengast, G.: Climate intercomparison of GPS radio occultation, RS90/92 radiosondes and GRUAN from 2002 to 2013, Atmos. Meas. Tech., 8, 1819–1834, https://doi.org/10.5194/amt-8-1819-2015, 2015.

Luna, D., Pérez, D., Cifuentes, A., and Gómez, D.: Three-Cornered Hat Method via GPS Common-View Comparisons, IEEE T. Instrum. Meas., 66, 2143–2147, https://doi.org/10.1109/TIM.2017.2684918, 2017.

McColl, K., Vogelzang, J., Konings, A., Entekhabi, D., Piles, M., and Stoffelen, A.: Extended triple collocation: Estimating errors and correlation coefficients with respect to an unknown target, Geophys. Res. Lett., 41, 6229–6236, https://doi.org/10.1002/2014GL061322, 2014.

O'Carroll, A. G., Eyre, J. R., and Saunders, R. S.: Three-way error analysis between AATSR, AMSR-E, and in situ sea surface tem-

perature observations, J. Atmos. Ocean. Tech., 25, 1197–1207, https://doi.org/10.1175/2007JTECHO542.1, 2008.

Parrish, D. F. and Derber, J. C.: The National Meteorological Center's Spectral Statistical-Interpolation analysis system, Mon. Weather Rev., 120, 1747–1763, https://doi.org/10.1175/1520-0493(1992)120<1747:TNMCSS>2.0.CO;2, 1992.

Rieckh, T. and Anthes, R.: Evaluating two methods of estimating error variances using simulated data sets with known errors, Atmos. Meas. Tech. Discuss., https://doi.org/10.5194/amt-2018-75, in review, 2018.

Rieckh, T., Anthes, R., Randel, W., Ho, S.-P., and Foelsche, U.: Evaluating tropospheric humidity from GPS radio occultation, radiosonde, and AIRS from high-resolution time series, Atmos. Meas. Tech., 11, 3091–3109, https://doi.org/10.5194/amt-11-3091-2018, 2018.

Riley, W. J.: Application of the 3-cornered hat method to the analysis of frequency stability, Hamilton Technical Services, available at: http://www.wriley.com/3-CornHat.htm (last access: 1 July 2018), 2003.

Roebeling, R. A., Wolters, E. L. A., Meirink, J. F., and Leijnse, H.: Triple collocation of summer precipitation retrievals from SEVIRI over Europe with gridded rain gauge and weather radar data, J. Hydrometeorol., 13, 1552–1566, https://doi.org/10.1175/JHM-D-11-089.1, 2012.

Simmons, A. J. and Hollingsworth, A.: Some aspects of the improvement in skill of numerical prediction, Q. J. Roy. Meteor. Soc., 128, 647–677, https://doi.org/10.1256/003590002321042135, 2002.

Simmons, A. J., Hortal, M., Kelly, G., McNally, A., Untch, A., and Uppala, S.: ECMWF Analyses and Forecasts of Stratospheric Winter Polar Vortex Breakup: September 2002 in the Southern Hemisphere and Related Events, J. Atmos. Sci., 62, 668–689, https://doi.org/10.1175/JAS-3322.1, 2005.

Smith, E. and Weintraub, S.: The constants in the equation for atmospheric refractive index at radio frequencies, Proc. IRE, 41, 1035–1037, 1953.

Stoffelen, A.: Toward the true near-surface wind speed: Error modeling and calibration using triple collocation, J. Geophys. Res., 103, 7755–7766, https://doi.org/10.1029/97JC03180, 1998.

Su, C.-H., Ryu, D., Crow, W. T., and Western, A. W.: Beyond triple collocation: Applications to soil moisture monitoring, J. Geophys. Res., 119, 6419–6439, https://doi.org/10.1002/2013JD021043, 2014.

Valty, P., de Viron, O., Panet, I., Camp, M. V., and Legrand, J.: Assessing the precision in loading estimates by geodetic techniques in Southern Europe, Geophys. J. Int., 194, 1441–1454, https://doi.org/10.1093/gji/ggt173, 2013.

Vergados, P., Mannucci, A. J., and Ao, C. O.: Assessing the performance of GPS radio occultation measurements in retrieving tropospheric humidity in cloudiness: A comparison study with radiosondes, ERA-Interim, and AIRS data sets, J. Geophys. Res.-Atmos., 119, 7718–7731, https://doi.org/10.1002/2013JD021398, 2014.

Vergados, P., Mannucci, A. J., Ao, C. O., Jiang, J. H., and Su, H.: On the comparisons of tropical relative humidity in the lower and middle troposphere among COSMIC radio occultations and MERRA and ECMWF data sets, Atmos. Meas. Tech., 8, 1789–1797, https://doi.org/10.5194/amt-8-1789-2015, 2015.

Vogelzang, J., Stoffelen, A., Verhoef, A., and Figa-Saldaña, J.: On the quality of high-resolution scatterometer winds, J. Geophys. Res., 116, C10033, https://doi.org/10.1029/2010JC006640, 2011.

Part III.

Acronyms

1D-Var One-Dimensional Variational

3CH Three-Cornered Hat

AIRS Atmospheric Infrared Sounder

CONTRAST CONvective TRansport of Active Species in the Tropics

DMI Danish Institute for Meteorology

ERA-Interim ECMWF Reanalysis Interim

GCOS Global Climate Observing System

GFS Global Forecast System

GPS Global Positioning System

GRUAN Reference Upper-Air Network

IGRA Integrated Global Radiosonde Archive

ITCZ Intertropical Convergence Zone

JPL Jet Propulsion Laboratory

LEO Low-Earth Orbit

MSL Mean Sea Level

NCAR National Center for Atmospheric Research

ND Normalized Difference

NSF National Science Foundation

NWP Numerical Weather Prediction

PBL Planetary Boundary Layer

RH Relative Humidity

RHS Right Hand Side

RMS Root Mean Square

RO Radio Occultation

RO Radiookkultationsmethode

SI International System of Units

SR Super Refraction

STD Standard Deviation

UCAR University Corporation for Atmospheric Research

UTLS Upper Troposphere – Lower Stratosphere

WEGC Wegener Center for Climate and Global Change

List of Figures

Synopsis

2.1. Water molecule absorption lines in the near- and thermal infrared ... 11
2.2. Schematic of the overturning circulation ... 12

3.1. A radiosonde from 1929 compared to a modern-day radiosonde ... 17
3.2. Number of daily processed RO profiles at the WEGC over time ... 19
3.3. Schematic of the occultation geometry for a setting event ... 21
3.4. RO specific humidity retrieval errors resulting from temperature uncertainty ... 24
3.5. 1D-Var toy model ... 26

Paper I: Tropospheric dry layers in the Tropical Western Pacific: Comparisons of GPS radio occultation with multiple data sets

5.1. Locations of the CONTRAST profiles ... 36
5.2. RH, T, N, and q profiles for CONTRAST, RO, ERA, and GFS ... 37
5.3. RH profiles for CONTRAST, RO, ERA, and GFS ... 38
5.4. Two snapshots of the troposphere during a dry air intrusion ... 39
5.5. MTSAT-2 satellite images of brightness temperatures ... 40
5.6. Scatter plots for N, T, q, and RH ... 41
5.7. Scatter plots for RH for ERA, CONTRAST, and GFS ... 42
5.8. Frequency for RH$< 10\,\%$ at the potential temperature level 320 K ... 43
5.9. T, RH, q, and e profiles for ERA, RO 1D-Var, and RO simple ... 46
5.10. RO 1D-Var and simple retrieval q versus radiosonde data ... 46
5.11. RO 1D-Var versus simple retrieval q ... 47
5.12. RH, T, q, and e ERA and resulting RO profiles for a modified first guess ... 48

Paper II: Evaluating tropospheric humidity from GPS radio occultation, radiosonde, and AIRS from high-resolution time series

6.1. ERA annual average profiles for N, q, RH, and T 57
6.2. Scatter plots of q for 7 data sets versus ERA 58
6.3. Time series at Guam: ERA RH and q ND of PERSIST and GFS 59
6.4. Time series of the q ND of RS and AIRS at Guam 60
6.5. Time series of the q ND for four RO retrievals at Guam 61
6.6. Mean and RMS of the q ND for all data sets at Guam 62
6.7. Mean and RMS of the q ND for all data sets at Mina 63
6.8. Mean ND for dry versus wet conditions at Guam and Mina 63
6.9. The q difference from $\mathrm{CLIMO}_{\mathrm{JulOct}}$ during typhoon passages 64
6.10. Deviations for four RO retrievals from the intercenter mean 65
6.11. Map showing the studied locations 72
6.12. Sketch of the co-location of RO, RS, and AIRS 72
6.13. ERA 2007 time series at Guam for N, T, q, and RH 74
6.14. ERA 2007 time series at Ishi for N, T, q, and RH 75
6.15. 2007 time series of RH at Mina and q ND for PERSIST, GFS, RS, and AIRS 76
6.16. q ND for four RO retrievals at Mina 77
6.17. N ND for PERSIST, GFS, RS, and AIRS at Guam 78
6.18. N ND for four RO retrievals at Guam 79

Paper III: Estimating observation and model error variances using multiple data sets

7.1. Number of co-located measurements for Mina and Guam 83
7.2. The mean ERA profiles at Guam and Mina of q, RH, T, and N 84
7.3. Profiles of q, RH, T, and N for five data sets 85
7.4. Same as Fig. 7.3 except for normalized differences from ERA 85
7.5. STD of the apparent error and estimated RO and ERA error 87
7.6. Estimated error variances of q for RO, RS, GFS, and ERA 88
7.7. Estimated error variances of RH for RO, RS, GFS, and ERA 88
7.8. Estimated error variances of T for RO, RS, GFS, and ERA 89
7.9. Estimated error variances of N for RO, RS, GFS, and ERA 90
7.10. Mean of the three error variance estimates for q, RH, T and N 90

7.11. Estimated RO and RS error variances for calibrated and uncalibrated data 97
7.12. Estimated ERA and GFS error variances for calibrated and uncalibrated data 97
7.13. Mean of the three error variance estimates for q 98
7.14. Mean of the three error variance estimates for RH 99
7.15. Mean of the three error variance estimates for T 99
7.16. Mean of the three error variance estimates for N 100

List of Tables

Paper I: Tropospheric dry layers in the Tropical Western Pacific: Comparisons of GPS radio occultation with multiple data sets

5.1. Distances and time differences between co-located profiles 39
5.2. Mean, RMS, and Pearson R coefficients for RH 40

Paper II: Evaluating tropospheric humidity from GPS radio occultation, radiosonde, and AIRS from high-resolution time series

6.3. Mean annual values for N, q, RH, and T for ERA in 2007 73

Paper III: Estimating observation and model error variances using multiple data sets

7.4. ND of zonal mean RO and ERA q 91

Bibliography

Barbara Angerer, Florian Ladstädter, Barbara Scherllin-Pirscher, Marc Schwärz, Andrea Karin Steiner, Ulrich Foelsche, and Gottfried Kirchengast. Quality aspects of the Wegener Center multi-satellite GPS radio occultation record OPSv5.6. *Atmos. Meas. Tech.*, 10:4845–4863, 2017. doi: 10.5194/amt-10-4845-2017.

R. A. Anthes, D. Ector, D. C. Hunt, Y.-H. Kuo, C. Rocken, W. S. Schreiner, S. V. Sokolovskiy, S. Syndergaard, T-K. Wee, Z. Zeng, P. A. Bernhardt, K. F. Dymond, Y. Chen, H. Liu, K. Manning, W. J. Randel, K. E. Trenberth, L. Cucurull, S. B. Healy, S.-P. Ho, C. McCormick, T. K. Meehan, D. C. Thompson, and N. L. Yen. The COSMIC/FORMOSAT-3 mission: Early results. *Bull. Amer. Meteor. Soc.*, 89:313–333, 2008. doi: 10.1175/BAMS-89-3-313.

Richard Anthes and Therese Rieckh. Estimating observation and model error variances using multiple data sets. *Atmos. Meas. Tech. Discuss.*, 2018. doi: 10.5194/amt-2017-487. in review.

Richard A. Anthes. Exploring Earth's atmosphere with radio occultation: contributions to weather, climate, and space weather. *Atmos. Meas. Tech.*, 4:1077–1103, 2011. doi: 10.5194/amt-4-1077-2011.

Chi O. Ao, Duane E. Waliser, Steven K. Chan, Jui-Lin Li, Baijun Tian, Feiquin Xie, and Anthony J. Manucci. Planetary boundary layer heights from GPS radio occultation refractivity and humidity profiles. *J. Geophys. Res.*, 117:D16117, 2012. doi: 10.1029/2012JD017598.

P. Berrisford, P.W. Kållberg, S. Kobayashi, D.P. Dee, S. Uppala, A. Simmons, P. Poli, and H. Sato. Atmospheric conservation properties in ERA-Interim. *Quart. J. Roy. Meteor. Soc.*, 137:1381–1399, 2011. doi: 10.1002/qj.864.

Georg Beyerle, Klemens Hocke, Jens Wickert, Torsten Schmidt, Christian Marquardt, and Christoph Reigber. Gps radio occultations with CHAMP: A radio holographic analysis of GPS signal propagation in the troposphere and surface reflections. *J. Geophys. Res.*, 107:D24, 2002. doi: 1029/2001JD001402.

G. E. Bodeker, S. Bojinski, D. Cimini, R. J. Dirksen, M. Haeffelin, J. W. Hannigan, D. F. Hurst, T. Leblanc, F. Madonna, M. Maturilli, A. C. Mikalsen, R. Philipona, T. Reale, D. J. Seidel, D. G. H. Tan, P. W. Thorne, H. Vömel, , and J. Wang. Reference upper-air observations for climate: From concept to reality. *Bull. Amer. Meteor. Soc.*, 97:123–135, 2016. doi: 10.1175/BAMS-D-14-00072.1.

Randy G. Brown and Chidong Zhang. Variability of midtropospheric moisture and its effect on cloud-top height distribution during TOGA COARE. *J. Atmos. Sci.*, 54:2760–2774, 1997. doi: 10.1175/1520-0469(1997)054<2760:VOMMAI>2.0.CO;2.

Sean P. F. Casey, Andrew E. Dessler, and Courtney Schumacher. Five-year climatology of midtroposphere dry air layers in warm tropical ocean regions as viewed by AIRS/Aqua. *J. Appl. Meteor. Climatol.*, 48:1831–1842, 2009. doi: 10.1175/2009JAMC2099.1.

Piero Cau, John Methven, and Brian Hoskins. Representation of dry tropical layers and their origins in ERA-40 data. *J. Geophys. Res.*, 110:D06110, 2005. doi: 10.1029/2004JD004928.

Piero Cau, John Methven, and Brian Hoskins. Origins of dry air in the tropics and subtropics. *J. Climate*, 20:2745–2759, 2007. doi: 10.1175/JCLI4176.1.

Shu-Ya Chen, Ching-Yuang Huang, Ying-Hwa Kuo, and Sergey Sokolovskiy. Observational error estimation of FORMOSAT-3/COSMIC GPS radio occultation data. *Mon. Wea. Rev.*, 139(3):853–865, 2011. doi: 10.1175/2010MWR3260.1.

Ming-Dah Chou, Chun-Hsiung Weng, and Po-Hsiung Lin. Analyses of FORMOSAT-3/COSMIC humidity retrievals and comparisons with AIRS retrievals and NCEP/NCAR reanalyses. *J. Geophys. Res.*, 114:D00G03, 2009. doi: 10.1029/2008JD010227.

COSMIC Project Office. Variational Atmospheric Retrieval Scheme (VARS) for GPS radio occultation data. COSMIC technical report, version 1.1, University Corporation for Atmospheric Research, 2005.

Lidia Cucurull and John C. Derber. Operational implementation of COSMIC observations into NCEP's global data assimilation system. *Wea. Forecasting*, 23 (4):702–711, 2008. doi: 10.1175/2008WAF2007070.1.

Aiguo Dai, Junhong Wang, Peter W. Thorne, David E. Parker, Leopold Haimberger, and Xiaolan L. Wang. A new approach to homogenize daily radiosonde humidity data. *J. Climate*, 24(4):965–991, 2011. doi: 10.1175/2010JCLI3816.1.

D. P. Dee, S. M. Uppala, A. J. Simmons, P. Berrisford, P. Poli, S. Kobayashi, U. Andrae, M. A. Balmaseda, G. Balsamo, P. Bauer, P. Bechtold, A. C. M. Beljaars, L. van de Berg, J. Bidlot, N. Bormann, C. Delsol, R. Dragani, M. Fuentes, A. J. Geer, L. Haimberger, S. B. Healy, H. Hersbach, E. V. Hólm, L. Isaksen, P. Kållberg, M. Köhler, M. Matricardi, A. P. McNally, B. M. Monge-Sanz, J.-J. Morcrette, B.-K. Park, C. Peubey, P. de Rosnay, C. Tavolato, J.-N. Thépaut, and F. Vitart. The ERA-Interim reanalysis: configuration and performance of the data assimilation system. *Quart. J. Roy. Meteor. Soc.*, 137(656):553–597, 2011. doi: 10.1002/qj.828.

Gerald Desroziers and Serguei Ivanov. Diagnosing and adaptive tuning of observation-error parameters in a variational assimilation. *Quart. J. Roy. Meteor. Soc.*, 127(574):1433–1452, 2001. doi: 10.1002/qj.49712757417.

Jason P. Dunion and Christopher S. Marron. A reexamination of the Jordan mean tropical sounding based on awareness of the Saharan air layer: Results from 2002. *J. Climate*, 21:5242–5253, 2008. doi: 10.1175/2008JCLI1868.1.

Christopher R. Ekstrom and Paul A. Koppang. Error bars for three-cornered hats. *IEEE Trans. Ultrason. Ferroelect. Freq. Contr.*, 53(5):876–879, 2006. doi: 10.1109/TUFFC.2006.1632679.

Kerry A. Emanuel. The theory of hurricanes. *Annu. Rev. Fluid Mech.*, 23:179–196, 1991. doi: 10.1146/annurev.fl.23.010191.001143.

European Centre for Medium-Range Weather Forecasts. ERA-Interim Project, 2009. URL `http://dx.doi.org/10.5065/D6CR5RD9`.

Hongliang Fang, Shanshan Wei, Chongya Jiang, and Klaus Scipal. Theoretical uncertainty analysis of global MODIS, CYCLOPES, and GLOBCARBON LAI products using a triple collocation method. *Remote Sensing of Environment*, 124:610–621, 2012. doi: 10.1016/j.rse.2012.06.013.

Ulrich Foelsche. *Tropospheric water vapor imaging by combination of ground-based and spaceborne GNSS sounding data*. Doctoral dissertation, University of Graz, Austria, 1999.

Ulrich Foelsche, Michael Borsche, Andrea Karin Steiner, Andreas Gobiet, Barbara Pirscher, Gottfried Kirchengast, Jens Wickert, and Torsten Schmidt. Observing upper troposphere-lower stratosphere climate with radio occultation data from the CHAMP satellite. *Climate Dyn.*, 31:49–65, 2008. doi: 10.1007/s00382-007-0337-7.

Ulrich Foelsche, Barbara Pirscher, Michael Borsche, Gottfried Kirchengast, and Jens Wickert. Assessing the climate monitoring utility of radio occultation data: From CHAMP to FORMOSAT-3/COSMIC. *Terr. Atmos. Ocean. Sci.*, 20(1): 155–170, 2009. doi: 10.3319/TAO.2008.01.14.01(F3C).

J.R. Garratt. *The Atmospheric Boundary Layer*. Cambridge Univ. Press, 1992. ISBN 0521467454.

Shay Gilpin, Therese Rieckh, and Richard Anthes. Reducing representativeness and sampling errors in radio occultation–radiosonde comparisons. *Atmos. Meas. Tech.*, 11:2567–2582, 2018. doi: 10.5194/amt-11-2567-2018.

M. E. Gorbunov, H.-H. Benzon, A. S. Jensen, M. S. Lohmann, and A. S. Nielsen. Comparative analysis of radio occultation processing approaches based on Fourier integral operators. *Radio Sci.*, 39:RS6004, 2004. doi: 10.1029/2003RS002916.

Mikhail. E. Gorbunov. Radioholographic analysis of radio occultation data in multipath zones. *Radio Sci.*, 37, 2002. doi: 10.1029/2000RS002577.

J. E. Gray and D. W. Allan. A method for estimating the frequency stability of an individual oscillator, 1974. Atlantic City, New Jersey, May 29–31.

E. Griggs, E.R. Kursinski, and D. Akos. An investigation of gnss atomic clock behaviour at short time intervals. *GPS Solut.*, 18:443–452, 2014. doi: 10.1007/s10291-013-0343-7.

E. Griggs, E.R. Kursinski, and D. Akos. Short-term gnss satellite clock stability. *Radio Sci.*, 50(8):813–826, 2015. doi: 10.1002/2015RS005667.

A. Gruber, C.-H. Su, S. Zwieback, W. Crow, W. Dorigo, and W. Wagner. Recent advances in (soil moisture) triple collocation analysis. *Int. J. Appl. Earth Obs. and Geoinf.*, 45:200–211, 2016. doi: 10.1016/j.jag.2015.09.002.

George A. Hajj, Emil Robert Kursinski, Larry J. Romans, Willy I. Bertiger, and Stephen S. Leroy. A technical description of atmospheric sounding by GPS occultation. *J. Atmos. Solar-Terr. Phys.*, 64(4):451–469, 2002. doi: 10.1016/S1364-6826(01)00114-6.

Shu-Peng Ho, Gottfried Kirchengast, Stephen Leroy, Jens Wickert, Anthony J. Mannucci, Andrea K. Steiner, Doug Hunt, William Schreiner, Sergey Sokolovskiy, Chi Ao, Michael Borsche, Axel von Engeln, Ulrich Foelsche, Stefan Heise, Byron Iijima, Ying-Hwa Kuo, Emil R. Kursinski, Barbara Pirscher, Mark Ringer, Chris Rocken, and Torsten Schmidt. Estimating the uncertainty of using GPS radio

occultation data for climate monitoring: Intercomparison of CHAMP refractivity climate records from 2002 to 2006 from different data centers. *J. Geophys. Res.*, 114:D23107, 2009. doi: 10.1029/2009JD011969.

Shu-Peng Ho, Xinjia Zhou, Ying-Hwa Kuo, Douglas Hunt, and Jun-Hong Wang. Global evaluation of radiosonde water vapor systematic biases using GPS radio occultation from COSMIC and ECMWF analysis. *Remote Sensing*, 2:1320–1330, 2010. doi: 10.3390/RS2051320.

Shu-Peng Ho, Doug Hunt, Andrea K. Steiner, Anthony J. Mannucci, Gottfried Kirchengast, Hans Gleisner, Stefan Heise, Axel von Engeln, Christian Marquardt, Sergey Sokolovskiy, William Schreiner, Barbara Scherllin-Pirscher, Chi Ao, Jens Wickert, Stig Syndergaard, Kent B. Lauritsen, Stephen Leroy, Emil R. Kursinski, Ying-Hwa Kuo, Ulrich Foelsche, Torsten Schmidt, and Michael Gorbunov. Reproducibility of GPS radio occultation data for climate monitoring: Profile-to-profile inter-comparison of CHAMP climate records 2002 to 2008 from six data centers. *J. Geophys. Res.*, 117:D18111, 2012. doi: 10.1029/2012JD017665.

Shu-Peng Ho, Liang Peng, Richard A. Anthes, Ying-Hwa Kuo, and Hsiao-Chun Lin. Marine boundary layer heights and their longitudinal, diurnal, and interseasonal variability in the southeastern Pacific using COSMIC, CALIOP, and radiosonde data. *JClimate*, 28:2856–2872, 2015. doi: 10.1175/JCLI-D-14-00238.1.

Shu-Peng Ho, Liang Peng, Carl Mears, and Richard A. Anthes. Comparison of global observations and trends of total precipitable water derived from microwave radiometers and COSMIC radio occultation from 2006 to 2013. *ACPD*, 2017. doi: 10.5194/acp-2017-525. in review.

Shu-Peng Ho, Liang Peng, Carl Mears, and Richard A. Anthes. Comparison of global observations and trends of total precipitable water derived from microwave radiometers and COSMIC radio occultation from 2006 to 2013. *ACP*, 18:259–274, 2018. doi: 10.5194/acp-18-259-2018.

A. Hollingsworth and P. Lönnberg. The statistical structure of short-range forecast errors as determined from radiosonde data. part i: The wind field. *Tellus A*, 38A(2), 1986. doi: 10.1111/j.1600-0870.1986.tb00460.x.

Catherine E. Housecroft and Alan G. Sharpe. *Inorganic chemistry*. Pearson Education Limited, 3 edition, 2008.

IPCC. *"Historical Overview of Climate Change." In: Climate Change 2007: The Physical Science Basis. Contribution of Working Group I to the Fourth*

Assessment Report of the Intergovernmental Panel on Climate Change. Ed. by: Le Treut, H., R. Somerville, U. Cubasch, Y. Ding, C. Mauritzen, A. Mokssit, T. Peterson and M. Prather. Cambridge University Press, 2007.

Eric J. Jensen, Leonhard Pister, David E. Jordan, David W Fahey, Paul A. Newman, Troy Thornberry, Andrew Rollins, Glenn S. Diskin, T. Paul Bui, Matthew McGill, Dennis Hlavka, R. Paul Lawson, Ru-Shan Gao, Peter Pilewskie, James Elkins, Eric Hintsa, Fred Moore, Michael J. Mahoney, Elliot Atlas, Jochen Stutz, Klaus Pfeilsticker, Steven C. Wofsy, Stephanie Evan, and Karen H. Rosenlof. The NASA Airborne Tropical TRopopause EXperiment (ATTREX). *SPARC Newsletter*, 4: 15–24, 2013.

Richard H. Johnson, Paul E. Ciesielski, and Kenneth E. Hart. Tropical inversions near the 0°c level. *J. Atmos. Sci.*, 53:1838–1855, 1996.

B. H. Kahn, F. W. Irion, V. T. Dang, E. M. Manning, S. L. Nasiri, C. M. Naud, J. M. Blaisdell, M. M. Schreier, Q. Yue, K. W. Bowman, E. J. Fetzer, G. C. Hulley, K. N. Liou, D. Lubin, S. C. Ou, J. Susskind, Y. Takano, B. Tian, and J. R. Worden. The Atmospheric Infrared Sounder version 6 cloud products. *Atmos. Chem. Phys.*, 14:399–426, 2014. doi: 10.5194/acp-14-399-2014.

Niklaus Kämpfer. *Monitoring Atmospheric Water Vapor: Graound-Based Remote Sensing and In-situ Methods.* Springer, 2013. ISBN 978-1-4614-3908-0. doi: 10.1007/978-1-4614-3909-7.

N. Khélifa, M. Lecollinet, and M. Himbert. Molar mass of dry air in mass metrology. *Measurement*, 40(7–8):779–784, 2007. doi: 10.1016/j.measurement.2006.05.009.

J. T. Kiehl and Kevin E. Trenberth. Earth's annual global mean energy budget. *Bull. Amer. Meteor. Soc.*, 78(2):197–208, 1997. doi: 10.1175/1520-0477(1997)078<0197:EAGMEB>2.0.CO;2.

P. Kishore, M. Venkat Ratnam, S.P. Namboothiri, Isabella Velicogna, Ghouse Basha, J.H. Jiang, K. Igarashi, S.V.B. Rao, and V. Sivakumar. Global (50°S–50°N) distribution of water vapor observed by COSMIC GPS RO: Comparison with GPS radiosonde, NCEP, ERA-Interim, and JRA-25 reanalysis data sets. *J. Atmos. Solar-Terr. Phys.*, 73:1849–1860, 2011. doi: 10.1016/j.jastp.2011.04.017.

Daryl T. Kleist, David F. Parrish, John C. Derber, Russ Treadon, Wan-Shu Wu, and Stephen Lord. Introduction of the gsi into the ncep global data assimilation system. *Wea. Forecasting*, 24(6):1691–1705, 2009. doi: 10.1175/2009WAF2222201.1.

Kenneth R. Knapp. Scientific data stewardship of International Satellite Cloud Climatology Project B1 global geostationary observations. *J. Appl. Remote Sens.*, 2(1)(023548), 2008. doi: 10.1117/1.3043461.

Ying-Hwa Kuo, Tae-Kwon Wee, Sergey Sokolovskiy, Christian Rocken, William Schreiner, Douglas Hunt, and Richard A. Anthes. Inversion and error estimation of GPS radio occultation data. *J. Meteor. Soc. Japan*, 82(1B):507–531, 2004.

Emil Robert Kursinski and George A. Hajj. A comparison of water vapor derived from GPS occultations and global weather analyses. *J. Geophys. Res.*, 106(D1): 1113–1138, 2001. doi: 10.1029/2000JD900421.

Emil Robert Kursinski, George A. Hajj, Kenneth R. Hardy, L. J. Romans, and J. Tim Schofield. Observing tropospheric water vapor by radio occultation using the Global Positioning System. *Geophys. Res. Lett.*, 22(17):2365–2368, 1995. doi: 10.1029/95GL02127.

Emil Robert Kursinski, George A. Hajj, J. Tim Schofield, Roger P. Linfield, and Kenneth R. Hardy. Observing Earth's atmosphere with radio occultation measurements using the Global Positioning System. *J. Geophys. Res.*, 102(D19): 23429–23465, 1997. doi: 10.1029/97JD01569.

Florian Ladstädter, Andrea Karin Steiner, Marc Schwärz, and Gottfried Kirchengast. Climate intercomparison of GPS radio occultation, RS90/92 radiosondes and GRUAN from 2002 to 2013. *Atmos. Meas. Tech.*, 8:1819–1834, 2015. doi: 10.5194/amt-8-1819-2015.

Kent Lauritsen, Hans Gleisner, Johannes K. Nielsen, and Stig Syndergaard. Using a toy model to analyze relationships between radio occultation moist air retrieval algorithms, 2017. Joint COSMIC Tenth Data Users' Workshop and IROWG-6 Meeting. Estes Park, Colorado. September 21–27, 2017.

John R. Lazante, Stephen A. Klein, and Dian J. Seidel. Temporal homogenization of monthly radiosonde temperature data. part i: Methodology. *J. Climate*, 16: 224–240, 2002.

Stephen S. Leroy, J. A. Dykema, and J. G. Anderson. Climate benchmarking using GNSS occultation. In Ulrich Foelsche, Gottfried Kirchengast, and Andrea Karin Steiner, editors, *Atmosphere and Climate: Studies by Occultation Methods*, pages 287–302. Springer, 2006.

Diego Luna, Daniel Pérez, Alejandro Cifuentes, and Demián Gómez. Three-cornered hat method via GPS common-view comparisons. *IEEE Trans. Instrument. Measure.*, 66(8):2143–2147, 2017. doi: 10.1109/TIM.2017.2684918.

Brian E. Mapes and Paquita Zuidema. Radiative-dynamical consequences of dry tongues in the tropical troposphere. *J. Atmos. Sci.*, 53(4):620–638, 1996.

K.A. McColl, Jur Vogelzang, A.G. Konings, D. Entekhabi, M. Piles, and Ad Stoffelen. Extended triple collocation: Estimating errors and correlation coefficients with respect to an unknown target. *Geophys. Res. Lett.*, 41:6229–6236, 2014. doi: 10.1002/2014GL061322.

William G. Melbourne, Edgar S. Davis, C. B. Duncan, George A. Hajj, Kenneth R. Hardy, Emil Robert Kursinski, Thomas K. Meehan, L. E. Young, and Thomas P. Yunck. The application of spaceborne GPS to atmospheric limb sounding and global change monitoring. *JPL Publication*, 94–18:147, 1994.

Larry M. Miloshevich, Holger Vömel, David N. Whiteman, Barry M. Lesht, F. J. Schmidlin, and Felicita Russo. Absolute accuracy of water vapor measurements from six operational radiosonde types launched during AWEX-G and implications for AIRS validation. *J. Geophys. Res.*, 111:D09S10, 2006. doi: 10.1029/2005JD006083.

Susan Bucci Mockler. Water vapor in the climate system, 1995. URL `https://www.eso.org/gen-fac/pubs/astclim/espas/pwv/mockler.html`.

Peter J. Mohr, Barry N. Taylor, and David B. Newell. CODATA recommended values of the fundamental physical constants: 2006. *Rev. Mod. Phys.*, 80:633–730, 2008. doi: 10.1103//RevModPhys.80.633.

D. M. Murphy and T. Koop. Review of the vapour pressures of ice and supercooled water for atmospheric applications. *Quart. J. Roy. Meteor. Soc.*, 131:1539–1565, 2005. doi: 10.1256/qj.04.94.

Johannes N. Nielsen. ROM SAF CDOP-2 algorithm theoretical baseline document: Level 2B and 2C 1D-Var products. Algorithm theoretical baseline document, version 2.7, Danish Meteorological Institute (DMI), European Centre for Medium-Range Weather Forecasts (ECMWF), Institut d'Estudis Espacials de Catalunya (IEEC), Met Office (METO), 2016.

A. G. O'Carroll, J. R. Eyre, and R. S. Saunders. Three-way error analysis between AATSR, AMSR-E, and in situ sea surface temperature observations. *J. Atmos. Oceanic Tech.*, 25:1197–1207, 2008. doi: 10.1175/2007JTECHO542.1.

Laura Pan, E. Atlas, R. Salawitch, S. Honomichl, J. Bresch, W. Randel, E. Apel, R. Hornbrook, A. Weinheimer, D. Anderson, S. Andrews, S. Baidar, S. Beaton, T. Campos, L. Carpenter, D. Chen, B. Dix, V. Donets, S. Hall, T. Hanisco, C. Homeyer, L. Huey, J. Jensen, L. Kaser, D. Kinnison, T. Koenig, J. Lamarque, C. Liu, J. Luo, Z. Luo, D. Montzka, J. Nicely, R. Pierce, D. Riemer, T. Robinson, P. Romashkin, A. Saiz-Lopez, S. Schauffler, O. Shieh, M. Stell, K. Ullmann, G. Vaughan, R. Volkamer, , and G. Wolfe. The Convective Transport of Active Species in the Tropics (CONTRAST) experiment. *Bull. Amer. Meteor. Soc.*, 98: 106–128, 2017. doi: 10.1175/BAMS-D-14-00272.1.

David F. Parrish and John C. Derber. The National Meteorological Center's spectral statistical-interpolation analysis system. *Mon. Wea. Rev.*, 120:1747–1763, 1992. doi: 10.1175/1520-0493(1992)120<1747:TNMCSS>2.0.CO;2.

David B. Parsons, Jean-Luc Redelsperger, and Kunio Yoneyama. The evolution of the tropical western Pacific atmosphere–ocean system following the arrival of a dry intrusion. *Quart. J. Roy. Meteor. Soc.*, 126:517–548, 2000. doi: 10.1002/qj.49712656307.

Raymond T. Pierrehumbert. Thermostats, radiator fins, and the local runaway greenhouse. *J. Atmos. Sci.*, 52:1784–1806, 1995.

Barbara Pirscher. *Multi-satellite climatologies of fundamental atmospheric variables from radio occultation and their validation (Ph.D. thesis)*. Wegener Center Verlag Graz, 2010. ISBN 978-3-9502940-3-3. Sci. Rep. 33-2010.

P. Poli, J. Joiner, and E.R. Kursinski. 1DVAR analysis of temperature and humidity using GPS radio occultation refractivity data. *J. Geophys. Res.*, 107(D20):4448, 2002. doi: 10.1029/2001JD000935.

Paul Poli, Sean B. Healy, and Dick P. Dee. Assimilation of Global Positioning System radio occultation data in the ECMWF ERA-Interim reanalysis. *Quart. J. Roy. Meteor. Soc.*, 136:1972–1990, 2010. doi: 10.1002/qj.722.

William J. Randel, Louis Rivoire, Laura Pan, and Shawn Honomichl. Dry layers in the tropical troposphere observed during CONTRAST and global behavior from GFS analyses. *J. Geophys. Res.*, 121(23):14142–14158, 2016. doi: 10.1002/2016JD025841.

Therese Rieckh and Richard Anthes. Evaluating two methods of estimating error variance from multiple data sets using an error model. *Atmos. Meas. Tech. Discuss.*, 2018. doi: 10.5194/amt-2018-75. in review.

Therese Rieckh, Richard Anthes, William Randel, Shu-Peng Ho, and Ulrich Foelsche. Tropospheric dry layers in the tropical western Pacific: comparisons of GPS radio occultation with multiple data sets. *Atmos. Meas. Tech.*, 10: 1093–1110, 2017. doi: 10.5194/amt-10-1093-2017.

Therese Rieckh, Richard Anthes, William Randel, Shu-Peng Ho, and Ulrich Foelsche. Evaluating tropospheric humidity from GPS radio occultation, radiosonde, and AIRS from high-resolution time series. *Atmos. Meas. Tech. Discuss.*, 2018. doi: 10.5194/amt-2017-486. accepted.

W. J. Riley, 2003. URL `http://www.wriley.com/3-CornHat.htm`.

R. A. Roebeling, E. L. A. Wolters, J. F. Meirink, and H. Leijnse. Triple collocation of summer precipitation retrievals from SEVIRI over Europe with gridded rain gauge and weather radar data. *Journal of Hydrometeorology*, 13:1552–1566, 2012. doi: 10.1175/JHM-D-11-089.1.

Marc Schwärz, Gottfried Kirchengast, Barbara Scherllin-Pirscher, Jakob Schwarz, Florian Ladstädter, and Barbara Angerer. Multi-mission validation by satellite radio occultation – extension project. Wegener center/uni graz technical report for esa/esrin no01/2016, issue 1.1, Wegener Center for Climate and Global Change, University of Graz, 2016.

Steven C. Sherwood, R. Roca, T. M. Weckwerth, and N. G. Andronova. Tropospheric water vapor, convection, and climate. *Rev. Geophys.*, 48:RG2001, 2010. doi: 10.1029/2009RG000301.

Adrian J. Simmons and A. Hollingsworth. Some aspects of the improvement in skill of numerical prediction. *Quart. J. Roy. Meteor. Soc.*, 128(580):647–677, 2002. doi: 10.1256/003590002321042135.

Adrian J. Simmons, Mariano Hortal, Graeme Kelly, Anthony McNally, Agathe Untch, and Sakari Uppala. ECMWF analyses and forecasts of stratospheric winter polar vortex breakup: September 2002 in the southern hemisphere and related events. *J. Atmos. Sci.*, 62(3):668–689, 2005. doi: 10.1175/JAS-3322.1.

E. Smith and S. Weintraub. The constants in the equation for atmospheric refractive index at radio frequencies. *Proc. IRE*, 41:1035–1037, 1953.

Sergey Sokolovskiy. Modeling and inverting radio occultation signals in the moist troposphere. *Radio Sci.*, 36(3):441–458, 2001.

Sergey Sokolovskiy. Effect of superrefraction on inversions of radio occultation signals in the lower troposphere. *Radio Sci.*, 38(3), 2003. doi: 10.1029/2002RS002728.

Sergey Sokolovskiy, Christian Rocken, Douglas Hunt, William Schreiner, J. Johnson, D. Masters, and S. Esterhuizen. GPS profiling of the lower troposphere from space: Inversion and demodulation of the open-loop radio occultation signals. *Geophys. Res. Lett.*, 33(14):L14816, 2006. doi: 10.1029/2006GL026112.

Andrea K. Steiner, Doug Hunt, Shu-Peng Ho, Gottfried Kirchengast, A. J. Mannucci, Barbara Scherllin-Pirscher, H. Gleisner, Axel von Engeln, Torsten Schmidt, Chi Ao, Steven S. Leroy, E. R. Kursinski, Ulrich Foelsche, Michael Gorbunov, S. Heise, Ying-Hwa Kuo, Kent B. Lauritsen, C. Marquardt, C. Rocken, William Schreiner, Sergey Sokolovskiy, Stig Syndergaard, and Jens Wickert. Quantification of structural uncertainty in climate data records from GPS radio occultation. *Atmos. Chem. Phys.*, 13:1469–1484, 2013. doi: 10.5194/acp-13-1469-2013.

Bjorn Stevens and Sandrine Bony. Water in the atmosphere. *Physics Today*, 66: 29–34, 2013. doi: 10.1063/PT.3.2009.

A. Stoffelen. Toward the true near-surface wind speed: Error modeling and calibration using triple collocation. *J. Geophys. Res.*, 103:7755–7766, 1998. doi: 10.1029/97JC03180.

C.-H. Su, D. Ryu, W. T. Crow, and A. W. Western. Beyond triple collocation: Applications to soil moisture monitoring. *J. Geophys. Res.*, 119:6419–6439, 2014. doi: 10.1002/2013JD021043.

Joel Susskind, Chris D. Barnet, and John Blaisdell. Retrieval of atmospheric and surface parameters from AIRS/AMSU/HSB data in the presence of clouds. *IEEE Trans. Geoscience abd Remote Sens.*, 41(2):390–409, 2003. doi: 10.1109/TGRS.2002.808236.

Joel Susskind, John M. Blaisdell, and Lena Iredell. Improved methodology for surface and atmospheric soundings, error estimates, and quality control procedures: the atmospheric infrared sounder science team version-6 retrieval algorithm. *J. Appl. Remote Sens.*, 8, 2014. doi: 10.1117/1.JRS.8.084994.

Pierre Valty, Olivier de Viron, Isabelle Panet, Michel Van Camp, and Juliette Legrand. Assessing the precision in loading estimates by geodetic techniques in Southern Europe. *Geophys. J. Int.*, 194:1441–1454, 2013. doi: 10.1093/gji/ggt173.

Panagiotis Vergados, Anthony J. Mannucci, and Chi O. Ao. Assessing the performance of GPS radio occultation measurements in retrieving tropospheric humidity in cloudiness: A comparison study with radiosondes, ERA-interim, and AIRS data sets. *J. Geophys. Res.*, 119:7718–7731, 2014. doi: 10.1002/2013JD021398.

Panagiotis Vergados, Anthony J. Mannucci, Chi O. Ao, J.H. Jiang, and H. Su. On the comparisons of tropical relative humidity in the lower and middle troposphere among COSMIC radio occultations and MERRA and ECMWF data sets. *Atmos. Meas. Tech.*, 8:1789–1797, 2015. doi: 10.5194/amt-8-1789-2015.

Panagiotis Vergados, Anthony J. Mannucci, Chi O. Ao, Olga Verkhoglyadova, and Byron Iijima. Comparisons of the tropospheric specific humidity from GPS radio occultations with ERA-Interim, NASA MERRA, and AIRS data. *Atmos. Meas. Tech.*, 2018. doi: 10.5194/amt-11-1193-2018.

Jur Vogelzang, Ad Stoffelen, Anton Verhoef, and Julia Figa-Saldaña. On the quality of high-resolution scatterometer winds. *J. Geophys. Res.*, 116(C10033), 2011. doi: 10.1029/2010JC006640.

Holger Vömel, Henry B. Selkirk, Larry Miloshevich, J. Valverde-Canossa, Juan Valdés, E. Kyrö, R. Kivi, W. Stolz, G. Peng, and J. A. Diaz. Radiation dry bias of the Vaisala RS92 humidity sensor. *J. Atmos. Oceanic Tech.*, 24:953–963, 2007. doi: 10.1175/JTECH2019.1.

B.-R. Wang, X.-Y. Liu, and J.-K. Wang. Assessment of COSMIC radio occultation retrieval product using global radiosonde data. *Atmos. Meas. Tech.*, 6:1073–1083, 2013. doi: 10.5194/amt-6-1073-2013.

Junhong Wang and Liangying Zhang. Systematic errors in global radiosonde precipitable water data from comparisons with ground-based GPS measurements. *J. Climate*, 21:2218–2238, 2008. doi: 10.1175/2007JCLI1944.1.

R. Ware, M. Exner, M. Gorbunov, K. Hardy, B. Herman, Y. Kuo, T. Meehan, W. Melbourne, C. Rocken, W. Schreiner, Sergey Sokolovskiy, F. Solheim, X. Zou, R. Anthes, S. Businger, and K. Trenberth. GPS Sounding of the Atmosphere from Low Earth Orbit: Preliminary Results. *Bull. Amer. Meteor. Soc.*, 77(1), 1996.

Peter J. Webster and Roger Lukas. TOGA-COARE: The Coupled Ocean–Atmosphere Response Experiment. *Bull. Amer. Meteor. Soc.*, 73:1377–1416, 1992.

S. Wong, Eric J. Fetzer, M. Schreier, G. Manipon, E. F. Fishbein, B. H. Kahn, Q. Yue, and F. W. Irion. Cloud-induced uncertainties in AIRS and ECMWF temperature and specific humidity. *J. Geophys. Res.*, 120:1880–1901, 2015. doi: 10.1002/2014JD022440.

F. Xie, D.L. Wu, C.O. Ao, E.R. Kursinski, A.J. Manucci, and S. Syndergaard. Super-refraction effects on GPS radio occultation refractivity in marine boundary layers. *Geophys. Res. Lett.*, 37:L11805, 2010. doi: 10.1029/2010GL043299.

F. Xie, D.L. Wu, C.O. Ao, A.J. Manucci, and E.R. Kursinski. Advances and limitations of atmospheric boundary layer observations with gps occultation over southeast pacific ocean. *Atmos. Chem. Phys.*, 12(2):903–918, 2012. doi: 10.5194/acp-12-903-2012.

Mark A. Zondlo, Mark E. Paige, Steven M. Massick, and Joel A. Silver. Vertical cavity laser hygrometer for the National Science Foundation Gulfstream-V aircraft. *J. Geophys. Res.*, 115(D20), 2010. doi: 10.1029/2010JD014445.

Abstract:
This report investigates the quality of Radio Occultation (RO)-derived humidity using other remote sensing techniques, in-situ observing techniques, and model analyses and reanalyses. Since water vapor plays a key role in many atmospheric processes, a correct understanding of the distribution, transport, and vertical structure of tropospheric humidity are crucial to accurately model weather and climate. But to the present day, no single observing system can provide global accurate tropospheric humidity data with a resolution that captures their variability on all important vertical, horizontal, and time scales.
Using multiple observational data sets and models, we assess the quality of RO-derived tropospheric humidity. The structural uncertainty of RO-derived humidity is determined from comparisons of multiple different RO humidity retrievals. Even in challenging humidity conditions, such as high variability and extreme dryness, the accuracy of RO-derived humidity data is similar to the one of other state-of-the-art humidity measurements. Additionally, the RO technique features global coverage, all-weather capability, and same data quality for day and night time measurements. This shows the usefulness of RO for tropospheric humidity studies, as well as its potential to contribute tropospheric data to numerical weather prediction models via data assimilation.

Zum Inhalt:
Das Ziel dieser Arbeit ist es, die Qualität von Radiookkultation-Feuchtedaten mithilfe von anderen Fernerkundungsmethoden und in-situ Messungen sowie Modell-Analysen und Reanalysen abzuschätzen. Wasserdampf spielt eine große Rolle in vielen atmosphärischen Prozessen und genaues Wissen über die Verteilung und Vertikalstruktur troposphärischer Feuchte ist daher sehr wichtig um Wetter und Klima korrekt modellieren zu können. Allerdings gibt es keine einzige Messmethode, welche Wasserdampf global mit einer Auflösung messen kann, die dessen starke Variabilität auf zeitlicher, horizontaler und vertikaler Ebene widerspiegelt.
Die GPS Radiookkultationsmethode (RO) liefert die Möglichkeit, vertikal hoch aufgelöste Information über die Feuchteverteilung in der Troposphäre zu gewinnen. Die Qualität dieser RO Feuchtedaten wird mithilfe von Daten mehrerer Messmethoden sowie Modellen abgeschätzt. Ihre strukturelle Unsicherheit wird über Unterschiede zwischen verschiedenen RO Feuchte-Retrievals bestimmt. Sogar in Regionen mit starken Feuchteschwankungen ist die Genauigkeit von RO Feuchte vergleichbar mit der von anderen Messmethoden. Zusätzlich kann RO kurzzeitige und kleinräumige Variabilität auflösen und liefert globale Messungen unter allen Wetterbedingungen bei Tag wie bei Nacht. RO zeigt daher durchaus Potential troposphärische Daten im Datenassimilationsprozess der Wettervorhersage beitragen zu können.

Wegener Zentrum für Klima und Globalen Wandel
Karl-Franzens-Universität Graz
Brandhofgasse 5
8010 Graz, Austria
www.wegcenter.at
ISBN 978-3-9504501-8-7